

Microstructural Quantification, Property Prediction, and
Stochastic Reconstruction of Heterogeneous Materials

Using Limited X-Ray Tomography Data

by

Hechao Li

A Dissertation Presented in Partial Fulfillment
of the Requirements for the Degree
Doctor of Philosophy

Approved December 2016 by the
Graduate Supervisory Committee:

Yang Jiao, Chair
Yongming Liu
Yi Ren
Bin Mu
Nikhilesh Chawla

ARIZONA STATE UNIVERSITY

May 2017

ABSTRACT

An accurate knowledge of the complex microstructure of a heterogeneous material is crucial for quantitative structure-property relations establishment and its performance prediction and optimization. X-ray tomography has provided a non-destructive means for microstructure characterization in both 3D and 4D (i.e., structural evolution over time). Traditional reconstruction algorithms like filtered-back-projection (FBP) method or algebraic reconstruction techniques (ART) require huge number of tomographic projections and segmentation process before conducting microstructural quantification. This can be quite time consuming and computationally intensive.

In this thesis, a novel procedure is first presented that allows one to directly extract key structural information in forms of spatial correlation functions from limited x-ray tomography data. The key component of the procedure is the computation of a “probability map”, which provides the probability of an arbitrary point in the material system belonging to specific phase. The correlation functions of interest are then readily computed from the probability map. Using effective medium theory, accurate predictions of physical properties (e.g., elastic moduli) can be obtained.

Secondly, a stochastic optimization procedure that enables one to accurately reconstruct material microstructure from a small number of x-ray tomographic projections (e.g., 20 - 40) is presented. Moreover, a stochastic procedure for multi-modal data fusion is proposed, where both X-ray projections and correlation functions computed from limited 2D optical images are fused to accurately reconstruct complex heterogeneous materials in 3D. This multi-modal reconstruction algorithm is proved to be able to integrate the complementary data to perform an excellent optimization procedure,

which indicates its high efficiency in using limited structural information.

Finally, the accuracy of the stochastic reconstruction procedure using limited X-ray projection data is ascertained by analyzing the microstructural degeneracy and the roughness of energy landscape associated with different number of projections. Ground-state degeneracy of a microstructure is found to decrease with increasing number of projections, which indicates a higher probability that the reconstructed configuration matches the actual microstructure. The roughness of energy landscape can also provide information about the complexity and convergence behavior of the reconstruction for given microstructures and projection number.

ACKNOWLEDGMENTS

I am sincerely grateful to my advisor Dr. Yang Jiao, for his continued intellectual guidance and care throughout the years, without whom I could not possibly finish these work. I am also very grateful to Dr. Nikhilesh Chawla for his numerous help and professional advice on this project. I also want to express my gratitude to my committee members, Dr. Yongming Liu, Dr. Yi Ren, and Dr. Bin Mu, for their time and supporting on my research.

I would like to acknowledge Dr. James Mertens, C. Shashank Kaira, and Somya Singh, for doing the X-ray tomography experiment at lab-scale tomography facility at Arizona State University and Advanced Photon Source, Argonne National Laboratory, and providing me the projection data. I'm also grateful to Dr. Jason Williams for developing the code of FBP reconstruction algorithm to provide us referential reconstruction results.

I also appreciate all the support and encouragement from my close friends, and all my lab mates, Yaopengxiao Xu, Shaohua Chen, Long Liang and Deepark Karunakaran throughout the years of my staying at Arizona State University.

Most of all, I want to thank my parents, Yulai Li, Binghong, Zhao, for their endless love through my entire life. It is their unconditional support and encouragement that make me a better person.

I want to thank National Science Foundation (DMR-1305119) for the funding and financial support.

TABLE OF CONTENTS

	Page
LIST OF TABLES	vii
LIST OF FIGURES	viii
CHAPTER	
1 INTRODUCTION	1
1.1 Heterogeneous Materials	1
1.2 Quantification of the Microstructure	2
1.3 Property Prediction of Heterogeneous Materials	4
1.4 X-Ray Tomography and Reconstruction	4
1.5 Microstructural Degeneracy and Energy Landscape	7
2 STRUCTURE QUANTIFICATION OF THE HETEROGENEOUS MATERIALS USING LIMITED X-RAY TOMOGRAPHY DATA	9
2.1 Definition of Correlation Functions	9
2.1.1 Standard N-Point Correlation Function	9
2.1.2 Two-Point Cluster Function	12
2.1.3 Surface Correlation Functions	13
2.2 Computing Probability Map from Limited X-Ray Tomography Data	14
2.3 Extracting Correlation Functions from Probability Map	18
2.3.1 N-Point Correlation Functions	18
2.3.2 Non-Standard Lower Order Correlation Functions	21

CHAPTER	Page
2.4 Quantification of Tin-Clay Composite Microstructure From Synchrotron and Lab-Scale X-Ray Tomographic Data.....	24
2.5 Summary.....	26
 3 PROPERTY PREDICTION USING THE MORPHOLOGICAL INFORMATION EXTRACTED FROM LIMITED X-RAY TOMOGRAPHY DATA	
3.1 Strong-Contrast Expansion Formulism.....	27
3.2 Statistical Sampling Method.....	28
3.3 Predicting Mechanical Properties of Polymer Matric Composites.....	35
3.4 Predicting Mechanical Properties of SiC/Al Composites.....	45
3.5 Summary.....	48
 4 STOCHASTIC RECONSTRUCTION USING LIMITED X-RAY TOMOGRAPHY DATA	
4.1 Stochastic Reconstruction Procedure via Simulated Annealing.....	49
4.1.1 Simulated Annealing Reconstruction Procedure	49
4.1.2 Algorithmic Details for Parallel-Beam Geometry	53
4.1.3 Algorithmic Details for Cone-Beam Geometry.....	56
4.2 Stochastic Reconstruction Using Simulated X-Ray Tomographic Projections.....	59
4.3 Reconstructions from Limited-Angle X-ray Tomographic Data.....	64
4.4 Stochastic Reconstruction with Multi-Modal Data Fusion.....	68
4.5 Summary.....	78

CHAPTER	Page
5 MICROSTRUCTURAL DEGENERACY AND ENERGY LANDSCAPE ASSOCIATED WITH X-RAY TOMOGRAPHIC PROJECTION	80
5.1 Microstructural Degeneracy and Density of States	80
5.2 Energy Landscape and Roughness Metric	87
5.3 Summary	101
6 FUTURE WORK	103
REFERENCES	105

LIST OF TABLES

Table	Page
3.1 Mechanical Properties of Each Component of Polymer Matrix Composites	36
3.2 3pt Parameters of Polymer Matrix Composites Structures with Different Volume Fractions of Glass Spheres (Single 2D slice).....	36
3.3 Effective Young's Modulus of Polymer Matrix Composites from Experimental Test, Theoretical Calculation from Single 2D Slice, and Normalized Difference for Different Volume Fractions of Glass Spheres.....	42
3.4 3pt Parameters of Polymer Matrix Composites Structures with Different Volume Fractions of Glass Spheres (6 Slices).....	44
3.5 Effective Young's Modulus of Polymer Matrix Composites from Experimental Test, Theoretical Calculation from 6 Independent 2D Slices, and Normalized Difference for Different Volume Fractions of Glass Spheres	45
3.6 Tensile Properties of Reinforced and Unreinforced 2080 Al [60]	47
3.7 Mechanical Properties of Each Component, 3pt Parameters and Estimated Young's Modulus of SiC Reinforced Aluminum Composite Material	47
4.1 Volume Fraction of the Target Phase and Normalized Error Between Target Structure and Reconstruction Results with Different Data Input.	75
5.1 System Size, Number of Target Pixels, Ground-State Degeneracy Associated with One Projection, and Theoretically the Number of All Possible Configurations...	84
5.2 Roughness Metric for Different Configurations with Same System Size and Number of Target Pixels	101

LIST OF FIGURES

Figure	Page
1.1 Schematic of a Two-Phase Heterogeneous Material with General Phase Properties K_1 and K_2 and Phase Volume Fraction Φ_1 and Φ_2	1
1.2 Schematic of Key Components of X-Ray Tomography and an Illustration of a 2D Projection of a 3D Hard Sphere Packing Structure. Different Colors in the 2D Projection Represent Different Attenuated Intensities.....	6
2.1 Schematic Illustration of the Probability Interpretation of the Correlation Functions. The Line Segments (Two-Point Configurations) and Triangles (Three-Point Configurations) Illustrate the Events That Contribute to the Corresponding Correlation Functions.....	9
2.2 Simple Illustration of One-Point and Two-Point Probability Functions As the Probability of Finding One Random Point and Two End Points of a Line Segment with Specific Length and Orientation to Be in the Phase of Interest, i.e., the Red Phase.	12
2.3 Schematic Illustration of Generating Probability Map. The Probability Is Calculated for the Highlighted Pixel as an Example. Only Two Projections from 0 and 90 Degrees Are Being Used.	17

Figure	Page
2.4 (a) The Test Configure Is a 2D Stripe-Like Structure with White Stripes Being the Phase of Interest and Black Phase as the Matrix. (b) The Probability Map Generated Using Only 30 Projections Evenly Distributed from 0 to 180 Degrees. The Value in Each Pixel Is the Probability of the Pixel Being in the Target Phase, i.e., Stripe-Like Particle. The Brighter the Color, the Higher the Probability of the Pixel Belongs to the White Phase.	18
2.5 Vector Based Two-Point Probability Functions Computed from Both the Target Structure (a), and the Probability Map (b). The Distance and Angle Between Each Pixel and the Center in the Image Is the Same as the Distance and Angle for Two Pixels in the Structure. The Value in Each Pixel Indicates the Probability of the Two Pixels Both Being in the Phase of Interest. The Brighter the Color, the Higher the Value.	20
2.6 Vector Based Two-Point Correlation Functions for Target Structure (a) (c) and Segmented Probability Map (b) (d). (a) and (b) Are Two-Point Cluster Function C2. (c) and (d) Are Surface Correlation Function Fss. The Distance and Angle Between Each Pixel and the Center in the Image Is the Same as the Distance and Angle for Two Pixels in the Structure. For C2, the Value in Each Pixel Indicates the Probability of the Two Pixels Both Being in the Phase of Interest and in the Same Cluster. For Fss, the Value in Each Pixel Indicates the Probability of the Two Pixels Both Being the Boundary Pixel in the Phase of Interest. The Brighter the Color, the Higher the Value.	23

Figure	Page
2.7 Vector Based Two-Point Correlation Functions for Tin-Clay Composite Microstructure. (A)(B)(C) Are the Two-Point Probability Function, Two-Point Cluster Function, and Surface Correlation Function Computed from Target Structure. (D)(E)(F) Are Corresponding Correlation Functions Computed from Probability Map Generated Using Synchrotron Data (Parallel-Beam Geometry). (G)(H)(I) Are Corresponding Correlation Functions Computed from Probability Map Generated Using Lab-Scale Data (Cone-Beam Geometry).....	25
3.1 Schematics of Statistical Sampling Method in 2D. (A) Shows the Primary Points Randomly and Uniformly Distributed in the Sample Domain. (B) Shows the Discrete Line Segment of Length ρ_k with the End Point Being the Primary Point and One Secondary Point (Originating from the Primary Point) in a Sampling Template. (C) Shows the Triangle Defined by Two-Line Segment of Length ρ_k, ρ_l , and the Angle between Them, θ_m , in a Sampling Template.....	29
3.2 Schematics of Sampling Template in 3D by Randomly Choosing the Euler Angle....	31
3.3 S_2 with R Smaller than 1 Compared to the Volume Fraction of a 3D Hard Sphere Packing Structure.....	33
3.4 Long Range Behavior of S_2 with R Goes to the Maximum Value Compared to the Theoretically Asymptotic Value of a 3D Hard Sphere Packing Structure.....	34
3.5 S_3 with Fixed R and S for Both Short Range and Long Range Values.....	35
3.6 2D Slice of Polymer Matrix Composite Materials with (A) 5%, (B) 10%, (C) 20%, and (D) 30% Volume Fractions of Glass Spheres.....	37

Figure	Page
3.7 Left Panel: A Segmented Virtual Slice of the Polymer Matrix Composite with 5% Borosilicate Spheres Obtained via Filtered-Backprojection Reconstruction. Middle Panel: The Probability Map Associated with the Virtual Slice Computed from 30 Simulated Synchrotron X-Ray Tomography Projections Evenly Distributed between 0 and 180 Degrees. Right Panel: The Two-Point Correlation Function S_2 Computed from the Probability Map.	39
3.8 Left Panel Shows the Effective Bulk Modulus with Different Percentage of Borosilicate Spheres Compared to the Hashin-Shtrikman Bounds. Right Panel Shows the Effective Shear Modulus with Different Percentage of Borosilicate Spheres Compared to the Hashin-Shtrikman Bounds.....	40
3.9 Comparison of the Young's Modulus Estimated from Limited X-Ray Tomography Data and That Obtained from Tensile Test for Composites with Different Particle Volume Fractions.	42
3.10 6 Independent 2D Slice of the 5% Polymer Matrix Composites.....	44
4.1 A Schematic Illustration of Parallel-Beam Projection Geometry in 2D.	51
4.2 Schematic Illustration of the Stochastic Reconstruction Procedure Using the Simulated Annealing Method: Energy-Increasing Trial Microstructures Can Be Accepted Initially in Order to Increase the Probability for the System to Converge to the Global or Very Deep Local Energy Minima.	53

Figure	Page
4.4 Schematic Illustration of Detector-Bin-Based Projection Method for Cone-Beam Geometry. For Each Detector Bin, a Path Connecting the Point X-Ray Source to the Bin Is Created. The Number of Voxels in the Discrete Sample Domain in the Target Phase Along That Path Is Then Counted. The Total Intensity Drop (i.e., Attenuation) Along That Path Is Computed and Record for That Bin.....	58
4.5 Reconstructions of the Sandstone Microstructure (A) from 5 (B), 10 (C), 20 (D) and 30 (E) Simulated Projections Generated in Parallel-Beam Geometry.	59
4.6 Reconstructions of the Sandstone Microstructure (A) from 5 (B), 10 (C), 20 (D) and 30 (E) Simulated Projections Generated in Cone-Beam Geometry.....	60
4.7 Reconstructions of a Dense Packing of Hard Ellipsoids (A) from 5 (B), 10 (C), 20 (D) and 30 (E) Simulated Projections Generated in Parallel-Beam Geometry.	61
4.8 Reconstructions of a Dense Packing of Hard Ellipsoids (A) from 5 (B), 10 (C), 20 (D) and 30 (E) Simulated Projections Generated in Cone-Beam Geometry.	61
4.9 The Accuracy Metric M_a as a Function of N_θ for the Reconstructions of the Sandstone Microstructure (A) and the Hard-Ellipsoid Packing (B). In Both Systems, M_a Initially Decays Rapidly as N_θ Increases and Virtually Decays to 0 Beyond $N_\theta = 20$	63
4.10 Reconstruction of the Helical Arrangement of Sn-Spheres in Clay from Cone-Beam Data. (A) A Projection (i.e., the Total Attenuation Intensity) Associated with the Projection Angle of 0° . (B) Reconstructed Microstructure from 30 Projections Evenly Distributed in the Interval Between 0 and 180 Degrees.	66

Figure	Page
4.11 Reconstruction of the Helical Arrangement of Sn-Spheres in Clay from Parallel-Beam Data. (A) A Projection (i.e., the Total Attenuation Intensity) Associated with the Projection Angle of 0°. (B) Reconstructed Microstructure from 30 Projections Evenly Distributed in the Interval Between 0 and 180 Degrees.	67
4.12 Reconstruction of a Random Distribution of Sn-Spheres in Clay from Parallel-Beam Data. (A) A Projection (i.e., the Total Attenuation Intensity) Associated with the Projection Angle 0°. (B) Reconstructed Microstructure from 30 Projections Evenly Distributed in the Interval Between 0 and 180 Degrees.	68
4.13 Left Panel: The Correlation Functions S_2 , C_2 and F_{ss} of a Concrete Microstructure (See Inset) as Computed from a 2D Optical Image. Right Panel: S_2 Associated with the Grains in a Polycrystalline Sn-Rich Solder Joint as Computed from a 2D EBSD Color Map (See Inset).....	71
4.14 Target Structure of a Fountainbleau Sample (A) and the Reconstruction Result Using Only S_2 (B), Only 4 Projections (C), and Both S_2 and 4 Projections (D).	74
4.15 Upper Panels: Parallel-Beam X-Ray Tomography Projection Intensity Maps for the Pb-Sn System at Different Aging Stages. Middle Panels: Optical Images of the Coarsening System at Different Stages Corresponding to the Tomography Data. Lower Panels: 3D Reconstruction of the Coarsening System via Stochastic Optimization Using Both Tomography Data and Optical Images. Linear Size of the System Shown in the Panels Is 180 μm	76
4.16 Target Structure of SiC/Al Composite (A) and the Reconstruction Result Using Only S_2 (B), Only 5 Projections (C), and Both S_2 and 5 Projections (D).	78

Figure	Page
5.1 Cumulative DOS Associated with Energy for (A) Single Disk, (B) Small Hard Disks, and (C) Poisson Point Process. The System Size Is 8 by 8, and the Number of Red Pixels Is 13 for All Three Configurations.	85
5.2 Cumulative DOS Associated with Energy for Configuration with Multiple Spheres. The System Size Is 32 by 32 and the Number of Red Pixels Is 196.....	87
5.3 Average Energy Associated with Hamming Distance for Single Sphere Structure Under the Condition of Different Number of Projections. The System Size Is 32 by 32 and the Number of Red Pixel Is 196.....	90
5.4 Average Energy Associated with Hamming Distance for a Structure of Poisson Point Process Under the Condition of Different Number of Projections. The System Size Is 32 by 32 and the Number of Red Pixel Is 196.....	91
5.5 Comparison of Average Energy $\langle E \rangle$ Associated with Hamming Distance for Three Different Structures with Same System Size, and Number of Red Pixels Under the Condition of 5 Projections.	93
6.1 Reconstruction of the Growth of a Fatigue Crack. The Growth Process Consists of 6 Images Showing Successive Growth Stages of the Crack. (A) Target Process. (B) Reconstructed Process.	104

CHAPTER 1

INTRODUCTION

1.1 Heterogeneous Materials

A heterogeneous material is the one that composed of domains of different materials or phases, such as a composite, or the same material in different states, such as a polycrystalline. Heterogeneous materials are normally studied in microscopic length scale, which is much larger than the molecular dimension, but much smaller than the size of characteristic length of a macroscopic sample. In such circumstances, a heterogeneous material can be viewed as a continuum on the microscopic scale, subject to classical analysis, and possess macroscopic properties at the same time, as shown in Figure 1.1. Typical examples can be easily found in synthetic materials, i.e., fiber and particulate composites, and natural environment, i.e., bones, tissue, sandstone, etc.

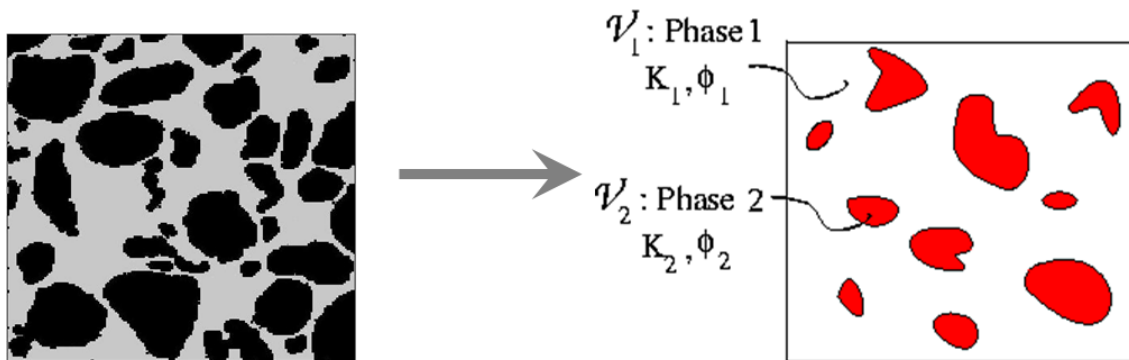


Figure 1.1 Schematic of a two-phase heterogeneous material with general phase properties K_1 and K_2 and phase volume fraction Φ_1 and Φ_2 .

The physical properties and performance of heterogeneous materials are determined by their complex microstructures and how such microstructures evolve under

various external stimuli [1, 2]. Traditionally, the study of material microstructure has been limited by two dimensional (2D) imaging techniques. This approach is often inaccurate or inadequate for solving many cutting-edge problems. It is also often laborious and time-consuming. Advances in experimental methods, analytical techniques, and computational approaches, have now enabled the development of three dimensional (3D) analyses [3]. The study of 3D microstructures under an external stimulus (e.g., stress, temperature, and environment) as a function of time (i.e., 4D materials science) is also particularly exciting. Examples include an understanding of time-dependent deformation structures, phase transformations, compositional evolution, magnetic domains, to name just a few.

1.2 Quantification of the Microstructure

The behavior and performance of an engineering material strongly depends on its complex microstructures on multiple length scales [1]. The recent developments in advanced imaging techniques such as x-ray tomography microscopy allow one to reveal detailed morphological features with sub-micrometer resolution and to investigate microstructural evolution *in situ* under different external stimuli [4-8]. Accurately quantifying the microstructure of a heterogeneous material from available image data is crucial to establishing quantitative structure-property relations for material optimization and design. To this end, several classes of structure quantification schemes have been developed.

A widely used class of quantification schemes employs feature-specific statistics. In these schemes, the morphological features of interest are prescribed, which may include the shape and size of grains or precipitates, degree of connectivity of filamentary

structures, to name but a few. Accordingly, feature-specific statistics are employed to quantify the prescribed structural characteristics. For example, distribution of aspect ratios, effective radius and geometrical moments are usually utilized to quantify the grain morphology of a polycrystalline material; while the coefficients of variation of local near statistics (e.g., nearest neighbor distance) are widely used to quantify the degree of clustering in particle reinforced composites. The statistics devised for a specific structural feature possess clear physical interpretations, but are not applicable to characterize other features. Another commonly used class of schemes borrows the techniques developed in computational pattern recognition. Specifically, a given microstructure image is decomposed (typically in Fourier space) and then is approximately represented by weighted combination of a set of “basis”. These pattern-recognition based methods are generic and can be easily applied to any microstructure on any length scales. However, the “basis” images usually contain random patterns without clear physical interpretations.

Recently, a new structure quantification scheme based on spatial correlation functions has been developed and successfully applied to model complex material microstructures on different length scales [9-13]. The spatial correlation functions are morphological descriptors that statistically characterize different geometrical and topological features of the materials of interest [1]. For example, the standard n-point correlation function $S_n(x_1, \dots, x_n)$ gives the probability of finding a specific n-point configuration with all points x_1, \dots, x_n fall into the phase of interests. There are a number of advantages of correlation function-based quantification scheme: (i) The correlation functions such as S_n are generic but still possess clear physical interpretations. Certain feature-specific statistics such as average particle sizes can be directly extracted from the

correlation functions. (ii) These statistically descriptors naturally arise in rigorous structure-property relations and be directly used to predict material properties for a given microstructure. (iii) Virtual 3D microstructures can be easily reconstructed for given correlation functions.

1.3 Property Prediction of Heterogeneous Materials

There are four different classes of steady-state effective media problems that have been widely studied, thermal/electric conductivity, elastic moduli, mean survival time, and fluid permeability [1]. Thermal/electrical conductivity is the macroscopic parameter to characterize the thermal/electrical properties of a heterogeneous material. For analyzing elastic moduli, effective stiffness tensor is one of the most important mechanical properties. In Physical and biological sciences, physical problems involving simultaneous diffusion and reaction in heterogeneous media are well concerned. For porous media, the key macroscopic property of describing slow viscous flow through porous media is the fluid permeability tensor.

In the past decade, a lot of works have been done on conductivity estimation and material design with desired physical properties [14-17]. All these works were proposed using spatial correlation functions and strong contrast expansion formulism to analyze thermal or electrical conductivities. None of them were working on elastic modulus. On the other hands, in their model, they computed spatial correlation functions from known structures, which is not available in our case, since we only have x-ray tomographic projection data.

1.4 X-ray Tomography and Reconstruction

An accurate knowledge of the complex microstructure of a heterogeneous

material and its evolution under external stimuli is crucial for the development of novel material systems to address the grand challenges raised by the world-wise growing demands in energy, security and health. Advanced imaging techniques such as scanning electron microscopy (SEM) [18], electron backscatter diffraction (EBSD) imaging [19-21], backscatter electron microscopy (BSE) [22], and X-ray tomographic microscopy [23, 24], to name but a few, allow one to obtain detailed microstructural information on different length scales or complementary morphological information on the same length scale. X-ray tomography microscopy, when properly combined with *in situ* experiments, is an extremely attractive, non-destructive technique for characterizing microstructure in 3D and 4D [25-27]. The use of high brilliance and partially coherent synchrotron light allows one to image multi-component materials from the sub-micrometer to nanometer range. X-ray tomography can be conducted in imaging modes based on absorption or phase contrast. The technique can also be used using lab-scale systems (See Figure 1.2). In x-ray tomography, 2D projections are usually obtained at small angular increments. Given a sufficiently large number of such 2D projections, tomographic reconstruction techniques such as the filtered-back-projection algorithm [28], algebraic reconstruction techniques [29], as well as trajectory-based direct iterative reconstruction method [30] can be employed to generate a grayscale image of the microstructure. Further segmentation and thresholding analysis are used to resolve details of individual material phases and produce accurate digital representations of the 3D microstructure. Such data sets can be used to quantify the microstructure, and/or can be used as an input for microstructure-based modeling. Thus, x-ray tomography is an excellent technique that eliminates destructive cross-sectioning, and allows for superior resolution and image

quality with minimal sample preparation [4-8, 31, 32].

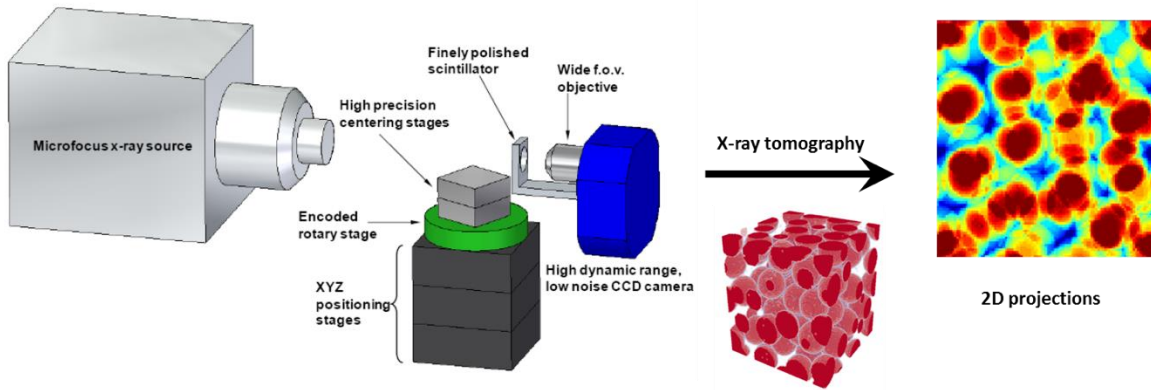


Figure 1.2 Schematic of key components of X-ray tomography and an illustration of a 2D projection of a 3D hard sphere packing structure. Different colors in the 2D projection represent different attenuated intensities.

The large number of 2D projections required for traditional reconstruction algorithms strongly limits the application of this technique in 4D materials science. An extremely large volume of data is usually needed as the input for the reconstruction algorithms even for a single “snapshot” of the microstructure at a given time-step. Characterizing an entire microstructural evolution process, at multiple time steps, may lead to hundreds of TB of data. Efficiently storing, retrieving, and maintaining such large data streams are a significant challenge to the materials community. Therefore, it is highly desirable to devise alternative reconstruction procedures that can render accurate virtual microstructures from only a handful of 2D projections. This will not only significantly reduce the volume of tomography data required to characterize a 4D process but also improve the temporal resolution since the time interval between successive

snapshots can be much shorter due to the smaller number of projections acquired.

If the material of interest only contains a small number of distinct phases and the phase properties (i.e., the attenuation coefficients) are known a priori, the reconstruction problem amounts to distributing different phases in a predefined discrete regular grid (e.g., simple cubic lattice), which is the focus of discrete tomography [33, 34]. Discrete tomography is closely related to several other mathematical fields, including number theory [35, 36], discrete geometry [37, 38] and combinatorics [39, 40]. It typically deals with reconstructions from a small number of projections and can directly yield a segmented 3D image, and thus, requires a complete different set of algorithms than the aforementioned “continuous” tomography (leading to grayscale images of material microstructure). A number of algorithms have been devised for discrete tomography reconstruction, including the discrete algebraic reconstruction technique [41, 42], the generic iterative subset algorithm [43], and the stochastic method for reconstruction of 3D grain maps from x-ray diffraction [44, 45]. In general, the iterative-based methods generate a reconstruction through successively improving an initial guess by incorporating more and more projection data [43]. The DART uses a grayscale reconstruction obtained from algebraic method for continuous tomography as a starting point, which is then segmented and the interface regions are iteratively improved [41, 42]. The stochastic methods devised in Refs. [44] and [45] reconstruct a microstructure by optimizing an initial structure to reproduce a predefined distribution of local pixel configurations.

1.5 Microstructural Degeneracy and Energy Landscape

The term degeneracy here refers to different structures perform same function or

same output. It is a widely studied term in material science field [46-52]. For example, Yang studied the pair distance associated with point configurations for characterizing the geometrical ambiguity of correlation functions [49, 50]. To be specific, he studied the point distance that can be applied to different configurations, i.e., structure degeneracy, and the condition where different configurations can possess same correlation functions, in other words, they form a degenerate pair. Gommes [51, 52] systematically studied for the first time the microstructural degeneracy associated with two-point correlation functions and its information content. He computed the degeneracy in the frame work of reconstructions, which can be used to determine the ground-state degeneracies. And he also measured the roughness of the energy landscape to approximate the ground-state degeneracy, which combined with density of states, can be used to define the information content that in return determine the complexity of reconstructing specific configuration.

Energy landscape can be considered as a map of all possible configurations associated with their energy levels. Every configuration can be grouped based on their difference with the given ground state configuration, which is represented by the hamming distance. As a result, an energy landscape will be strongly affected by ground-state degeneracy. Based on Gommes's work, the condition that one should have in order to get an accurate reconstruction is to have comparable information content, to the number of pixels (voxels in 3D) in the structure domain.

CHAPTER 2

STRUCTURE QUANTIFICATION OF THE HETEROGENEOUS MATERIALS USING LIMITED X-RAY TOMOGRAPHY DATA

2.1 Definition of Correlation Functions

2.1.1 Standard N-Point Correlation Function

In general, the microstructure of a heterogeneous material can be determined uniquely by specifying the indicator functions associated with all of the individual phases of the material [1]. Without loss of generality, we focus on two-phase materials (binary medium) in this work. The generalization of the subsequent discussion to a multiple-phase system is straightforward.

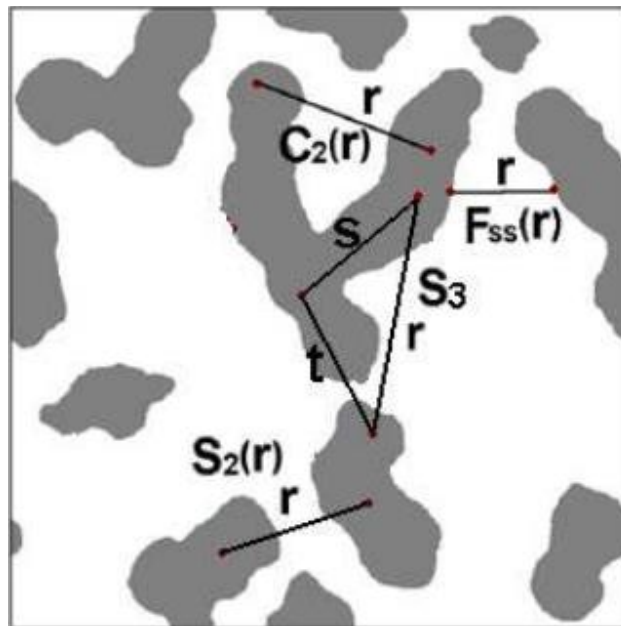


Figure 2.1 Schematic illustration of the probability interpretation of the correlation functions. The line segments (two-point configurations) and triangles (three point configurations) illustrate the events that contribute to the corresponding correlation functions.

Consider a heterogeneous material occupying some subset V of d -dimensional Euclidean space R^d ($d = 2, 3$), e.g. $V \in R^d$, which is partitioned into two disjoint random phases: phase 1, a region V_1 of volume fraction ϕ_1 , and phase 2, regions V_2 of volume fraction ϕ_2 (See Figure 1.1). Static indicate that the state of each point in the material is constant and independent of time. It is obvious that $V_1 \cup V_2 = V$ and $V_1 \cap V_2 = 0$. As we denote that phase 1 is our phase of interest, the indicator function $I^{(1)}(x)$ of phase 1 is then given by

$$I^{(1)}(x) = \begin{cases} 1, & x \in V_1 \\ 0, & x \in V_2 \end{cases} \quad (2.1)$$

One can follow the same procedure to get $I^{(2)}(x)$ and it is clearly to see that

$$I^{(1)}(x) + I^{(2)}(x) = 1 \quad (2.2)$$

The n -point correlation function (or n -point probability function) $S_n^{(1)}$ for phase 1 is then defined as follows (Figure 2.1):

$$S_n^{(1)}(\mathbf{x}_1, \mathbf{x}_2, \dots, \mathbf{x}_n) = \langle I^{(1)}(\mathbf{x}_1) I^{(1)}(\mathbf{x}_2) \dots I^{(1)}(\mathbf{x}_n) \rangle \quad (2.3)$$

where the angular brackets “ $\langle \dots \rangle$ ” denote ensemble averaging over independent realizations of the medium. Two simple illustrations will be one-point and two-point probability functions (see Figure 2.2). The one-point probability function $S_1^{(1)}$, which is the probability of finding one point to be in the phase 1, is equal to the volume fraction of the phase 1, i.e.,

$$S_1^{(1)}(\mathbf{x}_1) = \langle I^{(1)}(\mathbf{x}_1) \rangle = \phi_1 \quad (2.4)$$

The two-point probability function $S_2^{(1)}$ for phase 1 can then be derived from Eq. (2.3) as

$$S_2^{(1)}(\mathbf{x}_1, \mathbf{x}_2) = \langle I^{(1)}(\mathbf{x}_1) I^{(1)}(\mathbf{x}_2) \rangle \quad (2.5)$$

The system is statistically homogeneous if the joint probability distributions describing the stochastic process are translationally invariant, i.e., invariant under a translation (shift) of the space origin. For a statistically homogeneous medium, $S_2^{(1)}$ is a function of the relative displacements of point pairs,

$$S_2^{(1)}(\mathbf{x}_1, \mathbf{x}_2) = S_2^{(1)}(\mathbf{x}_1 - \mathbf{x}_2) = S_2^{(1)}(\mathbf{r}) \quad (2.6)$$

where $\mathbf{r} = \mathbf{x}_2 - \mathbf{x}_1$.

The material system is statistically isotropic if the joint probability distributions describing the stochastic process are rotationally invariant, i.e., invariant over rigid-body rotation of the spatial coordinates. If the medium is statistically isotropic, then $S_2^{(1)}$ is only a radial function, depending on the separation distances of point pairs,

$$S_2^{(1)}(\mathbf{x}_1, \mathbf{x}_2) = S_2^{(1)}(|\mathbf{r}|) = S_2^{(1)}(r) \quad (2.7)$$

Henceforth, we will drop the superscript in $S_2^{(1)}$ for simplicity. Without further elaboration, S_2 is always the two-point correlation function of the phase of interest. With the understanding of the nature of two-point probability functions, one can easily obtain the limit of the value of S_2 ,

$$\lim_{r \rightarrow 0} S_2(r) = \varphi_1 \quad \text{and} \quad \lim_{r \rightarrow \infty} S_2(r) = \varphi_1^2 \quad (2.8)$$

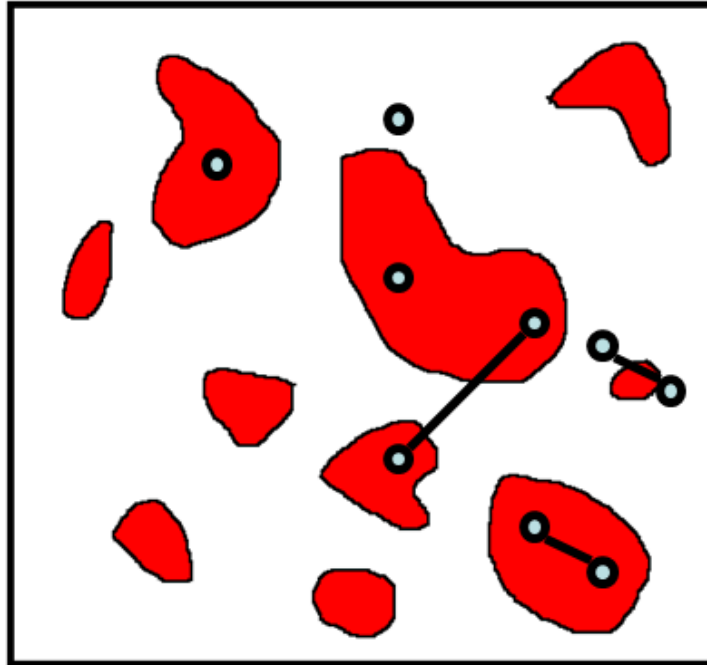


Figure 2.2 Simple illustration of one-point and two-point probability functions as the probability of finding one random point and two end points of a line segment with specific length and orientation to be in the phase of interest, i.e., the red phase.

2.1.2 Two-point Cluster Function

In a heterogeneous material, a cluster of phase i is defined as the part of phase i that can be reached from a point in phase i without passing through phase $j \neq i$. As a microstructural descriptor, two-point cluster function $C_2(x_1, x_2)$ is defined to be the probability of finding two randomly selected points x_1 and x_2 fall into the same cluster of the phase of interest (see Figure 2.1). For statistically homogeneous and isotropic materials, C_2 depends only on the relative distance r between the two points, like S_2 . It contains complete clustering information of the phases, which has been shown to have dramatic effects on the material's physical properties. And it will reach a critical point,

known as percolation threshold, when a sample-spanning cluster first appears. However, unlike S_2 , the cluster function generally cannot be obtained from lower-dimensional cuts (e.g., 2D slices) of a 3D microstructure, which may not contain correct connectedness information of the actual 3D system.

It has been shown that C_2 is related to S_2 via the following equation

$$S_2(r) = C_2(r) + D_2(r) \quad (2.9)$$

where $D_2(r)$ measures the probability that two points separated by r fall into different clusters of the phase of interest. In other words, C_2 is the connectedness contribution to the standard two-point correlation function S_2 . For microstructures with well-defined inclusion, $C_2(r)$ of the inclusions is a short-ranged function that rapidly decays to zero as r approaches the largest linear size of the inclusions. We note that although C_2 is a “two-point” quantity, it has been shown to encode higher-order structural information which makes it a highly sensitive statistical descriptor over and above S_2 .

2.1.3 Surface Correlation Functions

The surface correlation functions contain information about the random interface in a heterogeneous system (see Figure 2.1). Since such statistics arise in and are of basic importance in the trapping and flow problems, it is conventional in that context to let phase 1 denote the fluid or “void” phase and phase 2 denote the “solid” phase. The simplest surface correlation function is the specific surface $s(x)$ at point x , which gives the interface per unit volume, as a one point correlation function for statistically inhomogeneous media,

$$s(x) = \langle M(x) \rangle \quad (2.10)$$

where $M(x)$ is the interface indicator function defined as the absolute gradient of the

phase indicator function,

$$M(\mathbf{x}) = |\nabla I(\mathbf{x})| \quad (2.11)$$

We note that for statistically homogeneous material, the specific surface is a constant everywhere and thus, is simply denoted by s .

The two-point surface correlation functions for a general heterogeneous material are defined by

$$F_{SS}(\mathbf{x}_1, \mathbf{x}_2) = \langle M(\mathbf{x}_1)M(\mathbf{x}_2) \rangle \quad (2.12)$$

and

$$F_{Sv}(\mathbf{x}_1, \mathbf{x}_2) = \langle M(\mathbf{x}_1)I(\mathbf{x}_2) \rangle \quad (2.13)$$

which are respectively called the surface-surface and surface-void correlation functions.

For statistically homogeneous and isotropic materials, the functions F_{SS} and F_{Sv} only depend on the scalar distance $r = |\mathbf{x}_2 - \mathbf{x}_1|$. The functions can be obtained from any plane cut through a medium that is isotropic. When the two points are far from one another in systems without long range order $F_{SS}(\mathbf{x}_1, \mathbf{x}_2) \rightarrow s(\mathbf{x}_1)s(\mathbf{x}_2)$ and $F_{Sv}(\mathbf{x}_1, \mathbf{x}_2) \rightarrow s(\mathbf{x}_1)S_1(\mathbf{x}_2)$. In the case of homogeneous media, these asymptotic results for $|\mathbf{r}| \rightarrow \infty$ reduce to

$$\lim_{r \rightarrow \infty} F_{SS}(r) = \langle M \rangle \langle M \rangle = s^2, \quad \lim_{r \rightarrow \infty} F_{Sv}(r) = \langle M \rangle \langle I \rangle = s\phi \quad (2.14)$$

We note that unlike S_n , the surface correlation functions do not have a direct probability interpretation, since the probability of finding a point exactly falling on the interface is always zero. Instead, they can be associated with the probability of finding points in the dilated interface region with thickness δ in the limit $\delta \rightarrow 0$.

2.2 Computing Probability Map from Limited X-ray Tomography Data

In this section, we discuss in detail our procedure for computing the probability

map $P(x)$ from limited x-ray tomography data [53]. We first provide a brief description of how x-ray tomography projections are obtained, which is crucial to subsequent computation of the probability map. In x-ray tomography microscopy, a set of x-ray beams will be generated from an x-ray source, either as parallel beams (in synchrotron tomography at APS) or as cone beams (in lab-scale tomography at ASU). We refer to the former set-up as parallel beam geometry, and the latter one as cone-beam geometry. In both set-ups, the x-ray beams will pass through the material sample, and the attenuated intensity will be captured by the detector bin behind the sample. Because different phases in the material have different attenuation coefficients, attenuated intensity in the case of absorption contrast x-ray tomography can be written as the path-integral of the local attenuation coefficients. Specifically, the total attenuation $\pi = \ln(J/J_0)$ is given by

$$\pi = \ln(J/J_0) = -\int \mu(y)dy \quad (2.15)$$

where J and J_0 are respectively the attenuated and incident intensity of the x-ray, $\mu(y)$ is the attenuation coefficient along the path y that x-ray travels, and the integration is along the path. For a two-phase heterogeneous material, Eq. (2.15) can be further written as

$$\pi = -(\mu_1 L_1 + \mu_2 L_2) \quad (2.16)$$

where μ_1 and μ_2 are respectively the attenuation coefficient of the two phases, and L_1 and L_2 are respectively the length of the phases that x-ray travels along the path with total length $L = L_1 + L_2$.

Eq. (2.15) and (2.16) allow us to convert the total attenuation π to the relative volume fraction ϕ of the particle phase along the path of the x-ray hitting the bin by rescaling the total attenuation values with normalized attenuation coefficient of the particle phase. Specifically, the “volume fraction” ϕ_1 of phase 1 along the path is given

by

$$\varphi_1 = \frac{L_1}{L} = - \frac{\pi + \mu_2 L}{(\mu_1 - \mu_2)L} \quad (2.17)$$

where φ_1 can also be interpreted as the probability that a randomly selected point along the x-ray path belongs to phase 1.

This probability interpretation of rescaled total attenuation allows us to compute the probability map $P(x)$. As schematically illustrated in Figure 2.3, the probability of a point at position x belonging to the solid phase can be obtained by superposing the scaled attenuation intensity φ of the x-rays passing x from different angles, which are recorded in the projection data. Since the scaled attenuation intensity of a single x-ray passing x provides the probability of finding phase 1 (i.e., the volume fraction φ_1) along that path of the x-ray, superposing the probabilities associated with different x-ray paths leads to an estimate of the global probability $P^{(1)}(x)$ that point x belongs to phase 1. Once the probability map $P^{(1)}(x)$ for phase 1 is obtained, the probability map for phase 2 is simply given by $P^{(2)}(x) = 1 - P^{(1)}(x)$.

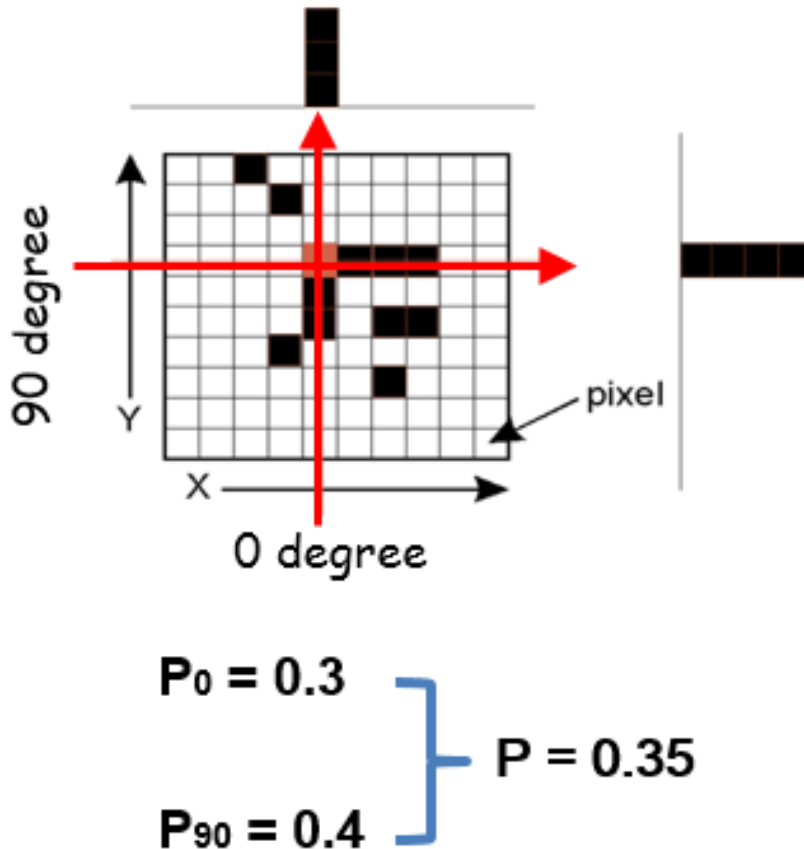


Figure 2.3 Schematic illustration of generating probability map. The probability is calculated for the highlighted pixel as an example. Only two projections from 0 and 90 degrees are being used.

Figure 2.4 illustrates the computation of the probability map for a model 2D binary microstructure (Figure 2.4a) with stripe-like inclusions. The probability map $P(x)$ for the inclusion phase (Figure 2.4b) is generated using only 30 simulated parallel beam projections evenly distributed in the interval between 0 and 180 degrees. (The projections are generated using an algorithm that simulates the process of an x-ray tomography scan during the experiment and results in a set of 1D projection of the 2D structure.) The value

of each pixel of $P(x)$ is the probability of the pixel being the inclusion phase. Brighter color indicates higher the probability values. We would like to emphasize that although the probability map appears to be very similar with the original microstructure, it is not a reconstruction of material microstructure and is obtained via distinctly different method instead of FBP or ART.

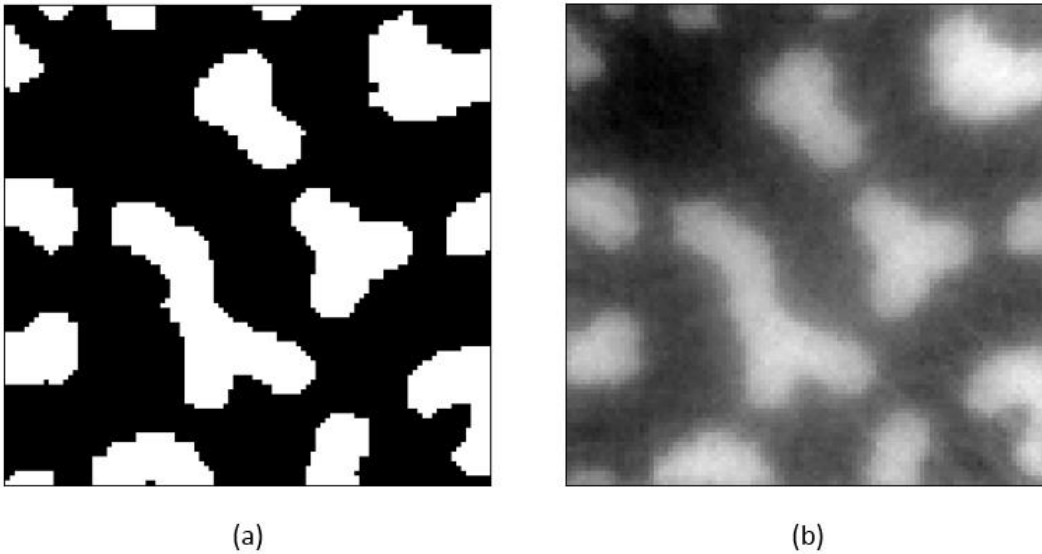


Figure 2.4 (a) The test figure is a 2D stripe-like structure with white stripes being the phase of interest and black phase as the matrix. (b) The probability map generated using only 30 projections evenly distributed from 0 to 180 degrees. The value in each pixel is the probability of the pixel being in the target phase, i.e., stripe-like particle. The brighter the color, the higher the probability of the pixel belongs to the white phase.

2.3 Extracting Correlation Functions from Probability Map

2.3.1 N-point Correlation Functions

Once the probability map is obtained, based on its probability interpretation, one

can easily compute the n -point correlation function as follows:

$$S_n^{(i)}(\mathbf{x}_1, \mathbf{x}_2, \dots, \mathbf{x}_n) = \frac{1}{V} \int P^{(i)}(\mathbf{x}_1 + \mathbf{r}) \cdot P^{(i)}(\mathbf{x}_2 + \mathbf{r}) \dots P^{(i)}(\mathbf{x}_n + \mathbf{r}) d\mathbf{r} \quad (2.18)$$

where $P^{(i)}(x)$ is the probability of finding phase i at position x , and the integration is carried out over the entire material with volume V , and statistical homogeneity is assumed in deriving Eq. (2.18).

In this subsequent discussion, we will focus on the two-point correlation function $S_2^{(i)}(\mathbf{r})$, which gives the probability of finding two points with relative vector displacement r both in phase i . We again illustrate this procedure using the stripe-like 2D model microstructure shown in Figure 2.4a. Specifically, given the probability map shown in Figure 2.4b, for a given displacement r , all pixel pairs $(x_1 + x_2)$ separated by r (i.e., $x_1 - x_2 = r$) are checked and $S_2^{(i)}(\mathbf{r})$ is computed as

$$S_2^{(i)}(\mathbf{r}) = \frac{1}{N} \sum_{\mathbf{x}_1} P^{(i)}(\mathbf{x}_1) \cdot P^{(i)}(\mathbf{x}_1 + \mathbf{r}) \quad (2.19)$$

where N is the total number of pixels. This process is repeated for all vector displacements, and the resulting $S_2(\mathbf{r})$ for the inclusion phase is shown in Figure 2.5b.

We note that this vector-based function is shown as a 2D grayscale map, with the displacement between a pixel and the center of the map indicating r and the value associated with the pixel being the value of S_2 at r .

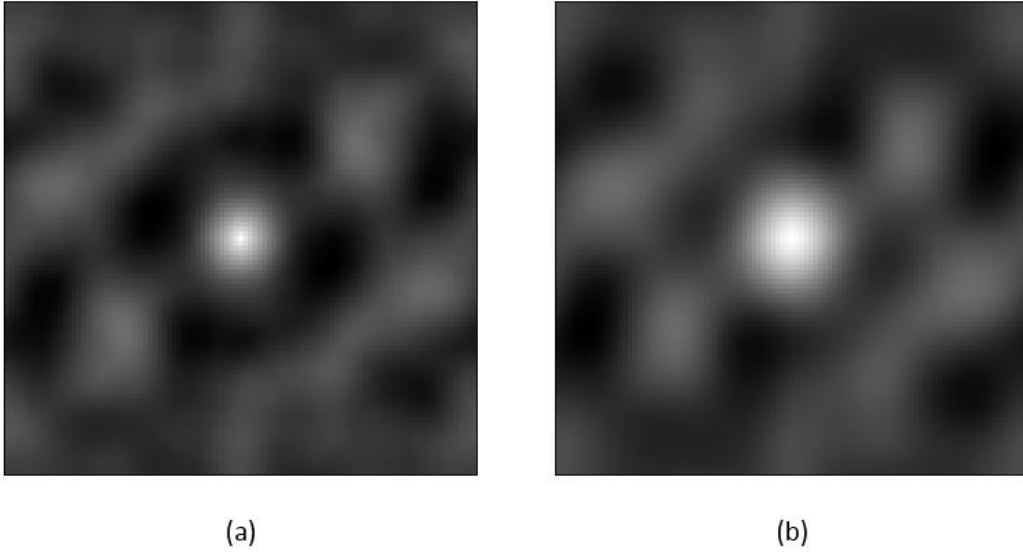


Figure 2.5 Vector based two-point probability functions computed from both the target structure (a), and the probability map (b). The distance and angle between each pixel and the center in the image is the same as the distance and angle for two pixels in the structure. The value in each pixel indicates the probability of the two pixels both being in the phase of interest. The brighter the color, the higher the value.

In order to verify our procedure for computing correlation functions based on the probability map and ascertain the accuracy of the computed function, we directly compute S_2^* of the inclusion phase from the original binary microstructure shown in Figure 2.4a and the resulting S_2^* is shown in Figure 2.5a. We use the mean squared error to quantify the difference between the two correlation functions, i.e.,

$$E = \frac{1}{N} \sum_r |f(\mathbf{r}) - f^*(\mathbf{r})|^2 \quad (2.20)$$

where N is the total number of pixels in the image of the vector based two-point

correlation functions. And P is the value of each pixel. The error energy calculated is 7.24×10^{-4} , which clearly indicates the validity and accuracy of our procedure.

2.3.2 Non-standard Lower Order Correlation Functions

The probability map computed from x-ray tomography data is continuous in nature, i.e., without sharp “interface” between the inclusion and matrix phase. As a result, the correlation functions such as the two-point cluster function C_2 and the surface correlation function F_{ss} and F_{sv} , which require a prior knowledge of corresponding structural features (e.g., well defined clusters of inclusions and interfaces), cannot be directly computed from the probability map. In order to extracting the necessary structural information for computing such non-standard lower order correlation functions from the projection data, the grayscale probability map is segmented to yield a binary image, which contains well-defined cluster and sharp interfaces between the phases. The binarized probability possesses pixel values of either 1 (100% probability in the inclusion phase) or 0 (100% probability in the matrix phase).

Now, the two-point cluster function C_2 and surface correlation functions F_{ss} and F_{sv} can be all computed from the segmented probability map, as shown in Figure 2.6, using the procedure developed for a general binary pattern reported in literature [1]. It can be seen that the vector-based C_2 (Figure 2.6b) only has significant values in the vicinity around the center and decays rapidly along the radial direction. This is consistent with the fact that the system only contains finite-sized inclusions and no percolating clusters. Thus, the cluster function is short-range and rapidly decays to zero when $|r|$ is great than the largest linear extent of the inclusions. The vector-based surface-surface correlation function F_{ss} is shown in Figure 2.6d. It can be seen that it possesses much

lower values than S_2 since only the interface pixels are considered which constitute a small portion of the total number of pixels.

To verify the accuracy of this procedure, the corresponding correlation functions are directly computed from the original binary microstructure and the mean squared errors E are also calculated for different correlation functions using Eq. (2.20). As the inclusion particles are better resolved after the segmentation, more morphological information can be captured, which leads to reduced error values. Indeed, we find the mean squared errors associated with C_2 and F_{ss} are respectively 1.86×10^{-5} and 2.89×10^{-6} . These results clearly indicate the validity of our procedure.

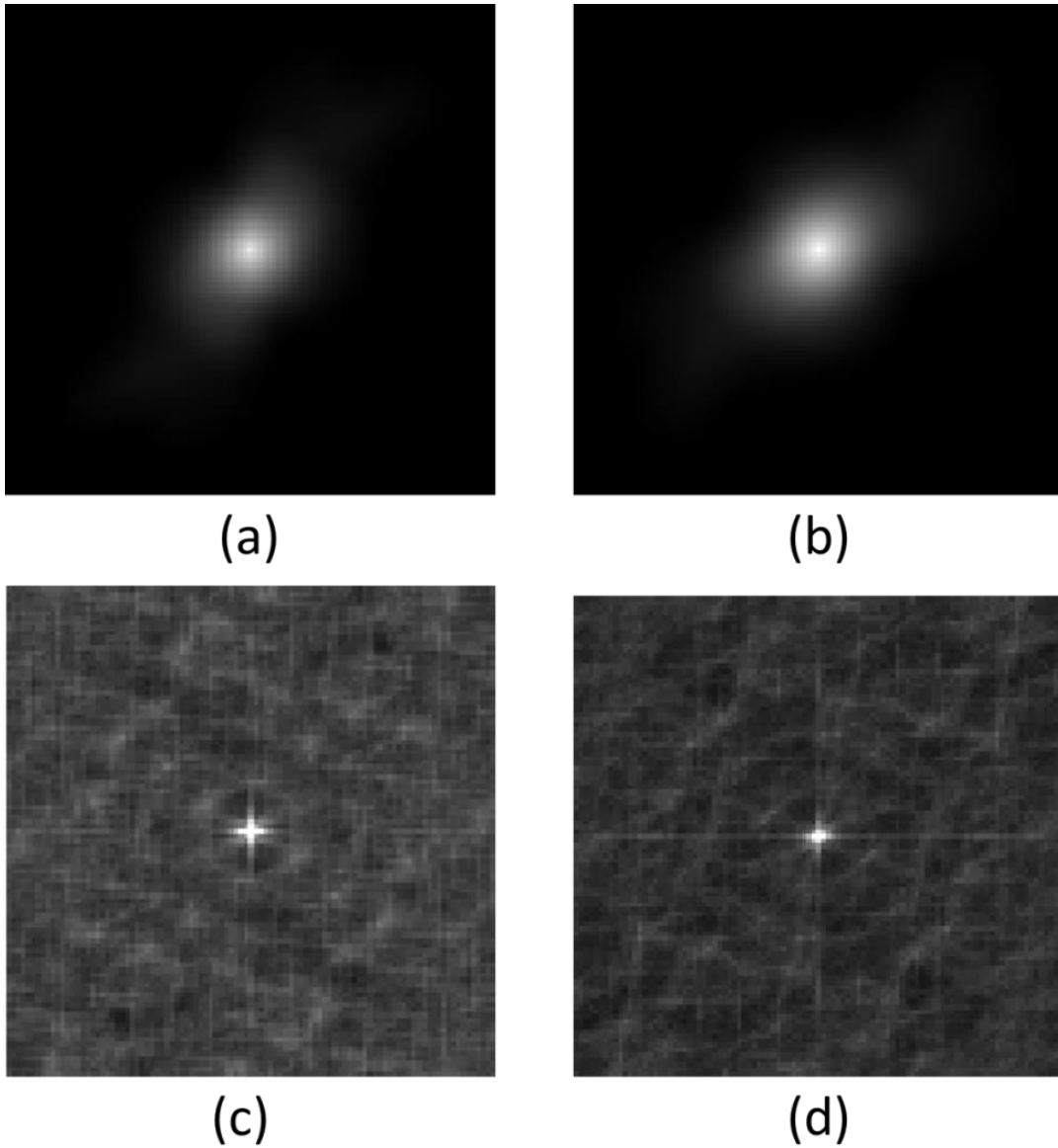


Figure 2.6 Vector based two-point correlation functions for target structure (a) (c) and segmented probability map (b) (d). (a) and (b) are two-point cluster function $C2$. (c) and (d) are surface correlation function F_{ss} . The distance and angle between each pixel and the center in the image is the same as the distance and angle for two pixels in the structure. For $C2$, the value in each pixel indicates the probability of the two pixels both being in the phase of interest and in the same cluster. For F_{ss} , the value in each pixel

indicates the probability of the two pixels both being the boundary pixel in the phase of interest. The brighter the color, the higher the value.

2.4 Quantification of Tin-Clay Composite Microstructure from Synchrotron and Lab-scale X-ray Tomographic Data

In this part, we apply the algorithm to generate probability map for a Sn-sphere-clay-matrix composite from limited angle tomographic data. The solder spheres are randomly distributed in the clay matrix. 30 parallel-beam synchrotron projections evenly distributed from 0 to 180 degrees that are obtained at Advanced Photon Source, Argonne Nation Lab and 30 cone-beam projections obtained via the lab-scale cone-beam tomography microscopy at ASU are used as input for generating the probability map. Follow the same procedure, probability maps were generated from each set of projections and two-point correlation functions were computed (Figure 2.7). Corresponding correlation functions were computed for comparison and error E were calculated. For cone-beam geometry, the error E for S_2 , C_2 , and F_{ss} between probability map and target structure are 1.80×10^{-4} , 8.80×10^{-10} , and 3.09×10^{-11} . For parallel geometry, the error E for S_2 , C_2 , and F_{ss} between probability map and target structure are 1.06×10^{-5} , 4.27×10^{-8} , and 1.09×10^{-9} .

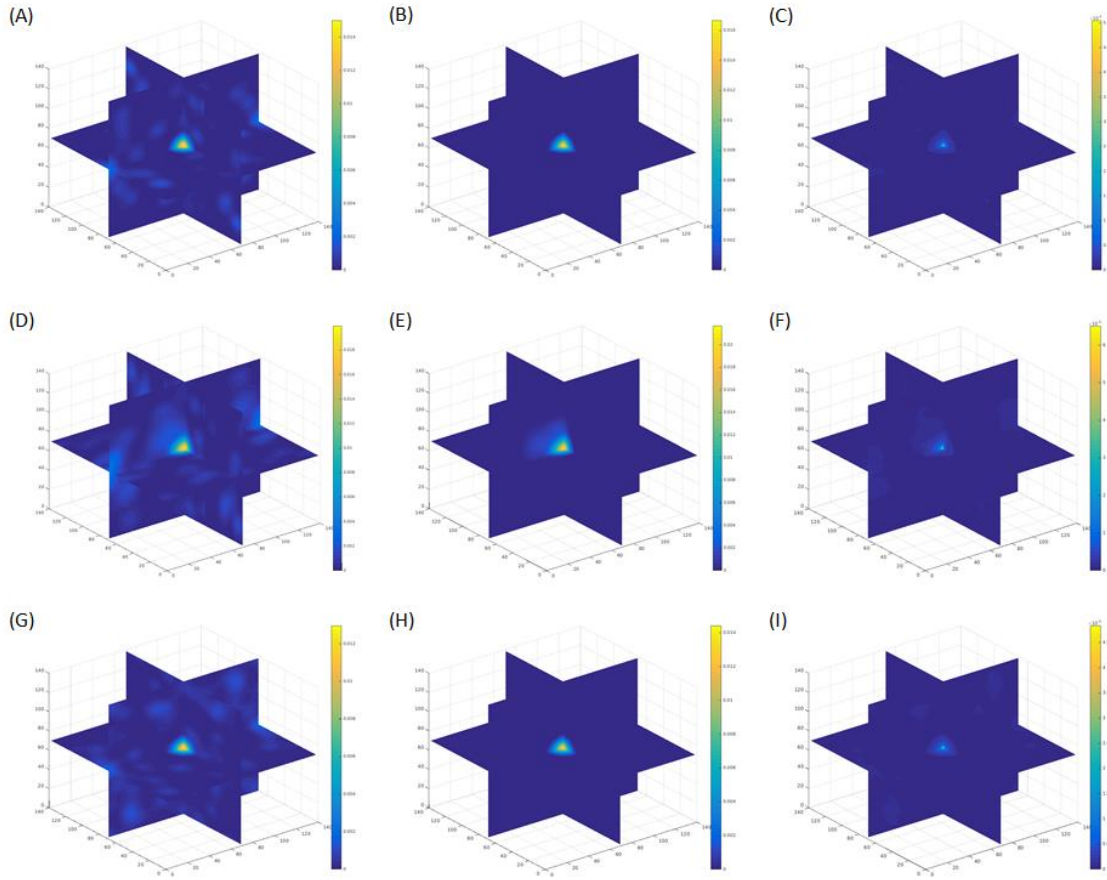


Figure 2.7 Vector based two-point correlation functions for Tin-clay composite microstructure. (A)(B)(C) are the two-point probability function, two-point cluster function, and surface correlation function computed from target structure. (D)(E)(F) are corresponding correlation functions computed from probability map generated using synchrotron data (parallel-beam geometry). (G)(H)(I) are corresponding correlation functions computed from probability map generated using lab-scale data (cone-beam geometry).

2.5 Summary

An alternative way of capturing structural information and represent the structure without any reconstruction process is presented in this chapter. The probability map is generated directly from limited tomographic projection with the value in each pixel indicating the probability of that pixel being in the phase of interest. The algorithm is tested on a simulated stripe-like two phase material. In order to fully extract the structural information from probability map, certain segmentation technique is processed to get a segmented probability map. Several vector based two-point correlation functions, such as two-point probability function S_2 , two-point cluster function C_2 , and surface correlation function F_{ss} , are computed for the target structure and both the probability map and segmented probability map. To quantitatively testify the robustness of our algorithm, an error energy is computed which is the difference between the value of pixels in the vector based two-point correlation functions computed from the target structure and the probability map. With all the error energies in or smaller than the magnitude of 10^{-4} , this indicates that the probability map algorithm can accurately capture almost all the morphological information contained in the projection data. And after certain segmentation procedure on the probability map, the resulting binary image can fully represent the target structure. And further analysis can be made such as predicting physical properties of the material using effective medium theory, which is based on the two-point correlation function computed from probability map.

CHAPTER 3

PROPERTY PREDICTION USING THE MORPHOLOGICAL INFORMATION

EXTRACTED FROM LIMITED X-RAY TOMOGRAPHY DATA

3.1 Strong-contrast Expansion Formalism

Directly extracting n-point correlation functions from limited x-ray tomography data allows us to immediately estimate the physical properties of the material of interest from such limited data, once the corresponding properties of individual phases are known. This is done by employing the strong-contrast expansion (SCE) formalism that analytically expresses the elastic moduli of a heterogeneous material as a series of integrals involving S_n and individual phase properties [1, 54, 55]. Here, we apply the SCE formalism to estimate the elastic moduli of polymer matrix (polypropylene) composites reinforced with glass sphere (borosilicate). For such as a composite microstructure in which the particle phase volume fraction is below the percolation threshold, it has been shown that truncating the expansion series at the 3rd order, which only incorporates two-point and three-point correlation functions (S_2 and S_3) into the solution, can already provide a highly accurate estimate of the bulk modulus K and shear modulus G of the system, i.e.,

$$\Phi_2 \frac{\kappa_{21}}{\kappa_{e1}} = 1 - \frac{(d+2)(d-1)G_1\kappa_{21}\mu_{21}}{d(K_1+2G_1)} \Phi_1 \zeta_2 \quad (3.1)$$

$$\begin{aligned} \Phi_2 \frac{\mu_{21}}{\mu_{e1}} = & 1 - \frac{2G_1\kappa_{21}\mu_{21}}{d(K_1+2G_1)} \Phi_1 \zeta_2 - \frac{(d^2-4)G_1(2K_1+3G_1)\mu_{21}^2}{2d(K_1+2G_1)^2} \Phi_1 \zeta_2 \\ & - \frac{1}{2d} \left[\frac{dK_1+(d-2)G_1}{K_1+2G_1} \right]^2 \mu_{21}^2 \Phi_1 \eta_2 \end{aligned} \quad (3.2)$$

where Φ_1 and Φ_2 are the volume fractions of phase 1 and phase 2, d is the dimension of the system, here $d = 3$, the scalar parameters κ_{21} and μ_{21} are bulk modulus polarizability

and shear modulus polarizability, i.e.,

$$\kappa_{21} = \frac{K_2 - K_1}{K_1 + \frac{2(d-1)}{d}G_1} \quad (3.3)$$

$$\mu_{21} = \frac{G_2 - G_1}{G_1 + \frac{G_1[\frac{dK_1}{2} + (d+1)(d-2)G_1/d]}{K_1 + 2G_1}} \quad (3.4)$$

κ_{e1} and μ_{e1} will be considered as scalar effective polarizabilities. $K_1, G_1, K_2,$ and G_2 are bulk and shear modulus of phase 1 and phase 2. ζ_2 and η_2 are the 3-pt parameters, i.e.,

$$\zeta_2 = \frac{9}{2\phi_1\phi_2} \int_0^\infty \frac{dr}{r} \int_0^\infty \frac{ds}{s} \int_{-1}^1 d(\cos\theta) P_2(\cos\theta) \left[S_3^{(2)}(r, s, t) - \frac{S_2^{(2)}(r)S_2^{(2)}(s)}{\phi_2} \right] \quad (3.5)$$

$$\eta_2 = \frac{5\zeta_2}{21} + \frac{150}{7\phi_1\phi_2} \int_0^\infty \frac{dr}{r} \int_0^\infty \frac{ds}{s} \int_{-1}^1 d(\cos\theta) P_4(\cos\theta) \left[S_3^{(2)}(r, s, t) - \frac{S_2^{(2)}(r)S_2^{(2)}(s)}{\phi_2} \right] \quad (3.6)$$

where $t = (r^2 + s^2 - 2rscos\theta)^{1/2}$, and P_2 and P_4 are respectively the Legendre polynomials of order two and four, i.e.,

$$P_2(x) = \frac{1}{2}(3x^2 - 1) \quad (3.7)$$

$$P_4(x) = \frac{1}{8}(35x^4 - 30x^2 + 3) \quad (3.8)$$

Eq. (3.1) and (3.2) require the evaluation of the three-point parameters ζ_2 and η_2 , which involves the three-point correlation function S_3 .

3.2 Statistical Sampling Method

In Chapter 2, we present the general procedure for extracting the n-point correlation function S_n from limited x-ray tomography data. In order to further improve the accuracy of computed ζ_2 and η_2 , we have used a non-uniform radial sampling template introduced in Ref. [56], in which the spatial density of the sampling points

monotonically increases (e.g., $\sim 1/r$) as one moves towards the original along the radial direction. This will provide sufficient number of sampling points for small r for an accurate numerical integration. In addition, the mechanical properties (i.e., bulk and shear moduli) of the individual phases required in Eq. (3.1) and (3.2) were obtained via nano-indentation technique and the overall Young's modulus of the composites was obtained via tensile test. The details for the aforementioned procedure will be presented below [56].

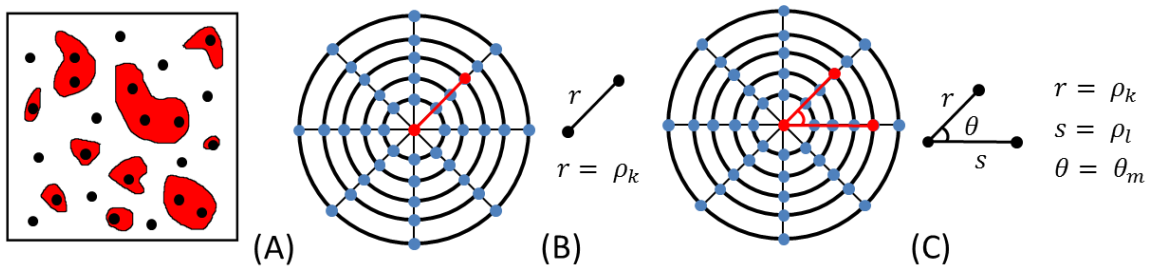


Figure 3.1 Schematics of statistical sampling method in 2D. (A) shows the primary points randomly and uniformly distributed in the sample domain. (B) shows the discrete line segment of length ρ_k with the end point being the primary point and one secondary point (originating from the primary point) in a sampling template. (C) shows the triangle defined by two-line segment of length ρ_k , ρ_l , and the angle between them, θ_m , in a sampling template.

The statistical sampling method was first proposed by Smith and Torquato [57], which is based on a Monte Carlo statistical sampling. The approach will first be described in two dimensions, and it will be shown that this method can be easily applied to three dimensions. For a two phase material, let phase 1 be the phase of interest to illustrate the approach. Initially, a large number N_p of primary points was randomly and

uniformly distributed throughout the material. In the current study, N_p is around 10^4 to 10^6 based on the different system sizes. For each primary point, a sampling template will be generated and the primary point will be considered as the center of the template. Each sampling template involves N_ρ number of concentric circles centering at the primary point with radii ρ_k ($k = 0, \dots, N_\rho - 1$), and N_ϕ radial rays equally spaced originating from the primary point. The intersection of the circles with the radial rays will be treated as secondary points, with total number $N_\rho N_\phi$ in each template. For each template, the primary point and each secondary point will form a set $\{A\}$ of $N_\rho N_\phi$ line segments with a range of discrete length ρ_k (originating from primary points). Then the value of $S_2(\rho_k)$ will be computed as the probability that the end points of a line segment with specific length ρ_k (one primary points and one secondary points) to be located in the phase of interest, averaging over $\{A\}$ and template ensemble. Similarly, this approach can be utilized to evaluate three points probability functions S_3 . In this case, a set of triangles were constructed formed by all possible combinations of two line segment from $\{A\}$ for each template. Every triangle can be defined as two discrete line segments with length ρ_k and ρ_l ($k, l = 0, \dots, N_\rho - 1$), and an angle θ_m between the two edges of the triangle ($m = 0, \dots, N_\phi - 1$). Then $S_3(\rho_k, \rho_l, \theta_m)$ can be evaluated as the probability of finding the vertices of a triangle defined by ρ_k, ρ_l, θ_m to be located in the phase of interest, averaging over $\{A\}$ and the template ensemble (Figure 3.1). This statistical sampling approach can be easily applied to three dimensions by generating the template with randomly choosing Euler angles (Figure 3.2).

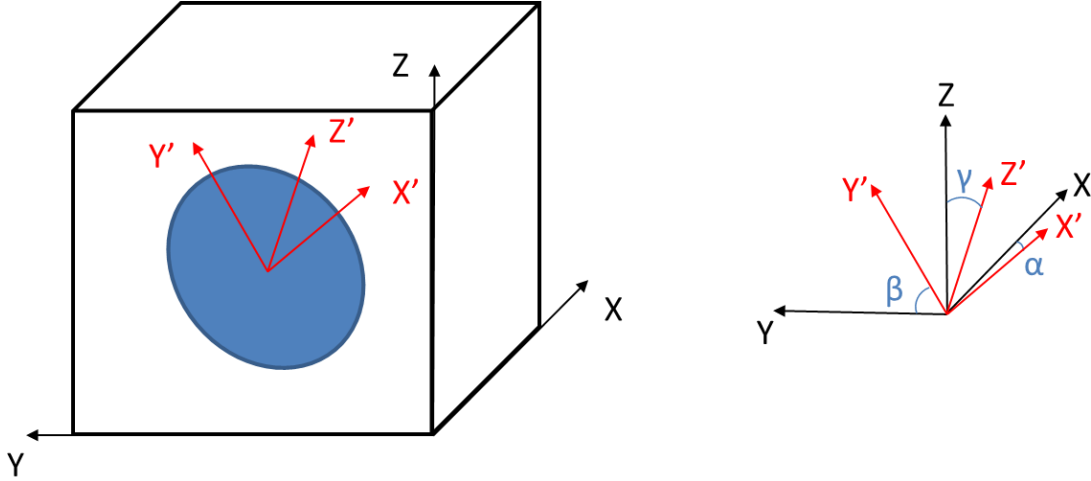


Figure 3.2 Schematics of sampling template in 3D by randomly choosing the Euler angle.

The calculation of ζ_2 and η_2 by Eq. (3.5) and (3.6) was carried out by numerical integration using discrete values of S_2 and S_3 evaluated using the statistical sampling method. Two dimensional trapezoidal rule was used for all three integrations. Because the Eq. (3.5) and (3.6) is proportional to r^{-1} and s^{-1} , the region of integration near $r = 0$ and $s = 0$ will make a huge contribution to the integral. This will require a fine spatial grid in order to get an accurate result. However, using fine spatial grid will result in huge computing time and requires large amount of discrete values of S_2 and S_3 since the range of the integral of r and s is from zero to infinity. In order to solve these conflicting requirements at the same time, one possible solution proposed by Hlushkou [56] is by using a non-uniform spatial grid to construct the concentric circle for the template, following a power law, as

$$\rho_k = a_0 A^k \quad (3.9)$$

where ρ_k is the radius of the k th concentric circle in the sampling template ($k = 0, \dots, N_\rho - 1$), a_0 is a constant indicating the radius of the smallest circle, and A is a constant which

is chosen to be slightly bigger than 1. In the current study, we follow Hlushkou's procedure that all the templates are constructed with $N\rho = 64, N\varphi = 64, a_0 = 10^{-4}, A = 1.21$, with the radius of the smallest circle $\rho_0 = 0.0001$, and the radius of the largest circle $\rho_{63} \approx 16.42$. With the sample domain to be normalized to 10 by 10 in 2D and 10 by 10 by 10 in 3D, and the average radius of phase 1 to be 0.25, around 64% of the concentric circles in a template will be within a particle of phase 1, providing a fine spatial grid when r and s near 0. At the same time, with ρ_{63} much larger than the system size, with the use of periodic boundary conditions, one can easily get the integral at long range, providing accurate result approximating the integral of r and s up to infinity.

The statistical sampling method was first test on a simulated 3D hard sphere packing structure with the volume fraction of the spheres to be around 11%. With the parameters chosen in the previous section, $S_2(r)$ and $S_3(r, s, t)$ are evaluated and the results shows in Figure 3.3 and 3.4. For S_2 in the short range, with the fine spatial grid, $S_2(r)$ is equal to the volume fraction of the spheres as

$$\lim_{r \rightarrow 0} S_2(r) = \Phi \quad (3.10)$$

With increasing r , we first see monotonic decrease with r approaching 1. And with several small oscillations around each integer, the value of S_2 eventually deduces to its asymptotic value, which is equal to Φ^2 , which indicating that the two points are independent between each other, with no long range correlation. The sampling method with non-uniform spatial grid also accurately capture this long rang behavior of S_2 as

$$\lim_{r \rightarrow \infty} S_2(r) = \Phi^2 \quad (3.11)$$

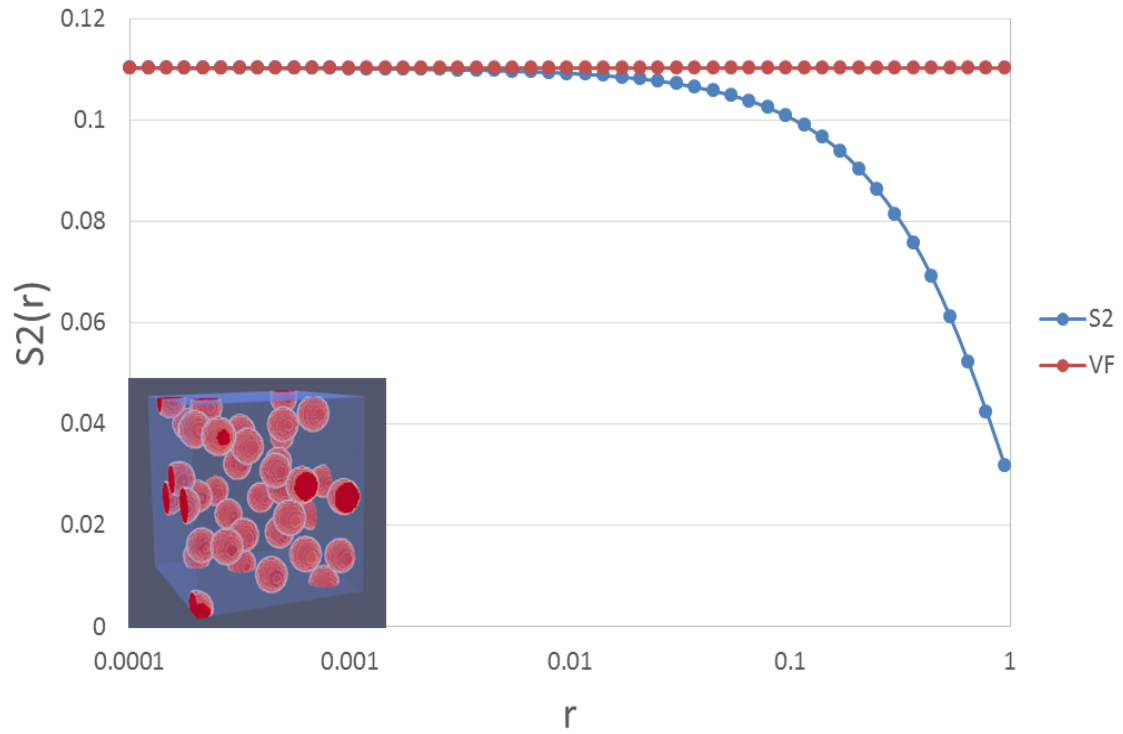


Figure 3.3 S_2 with r smaller than 1 compared to the volume fraction of a 3D hard sphere packing structure.

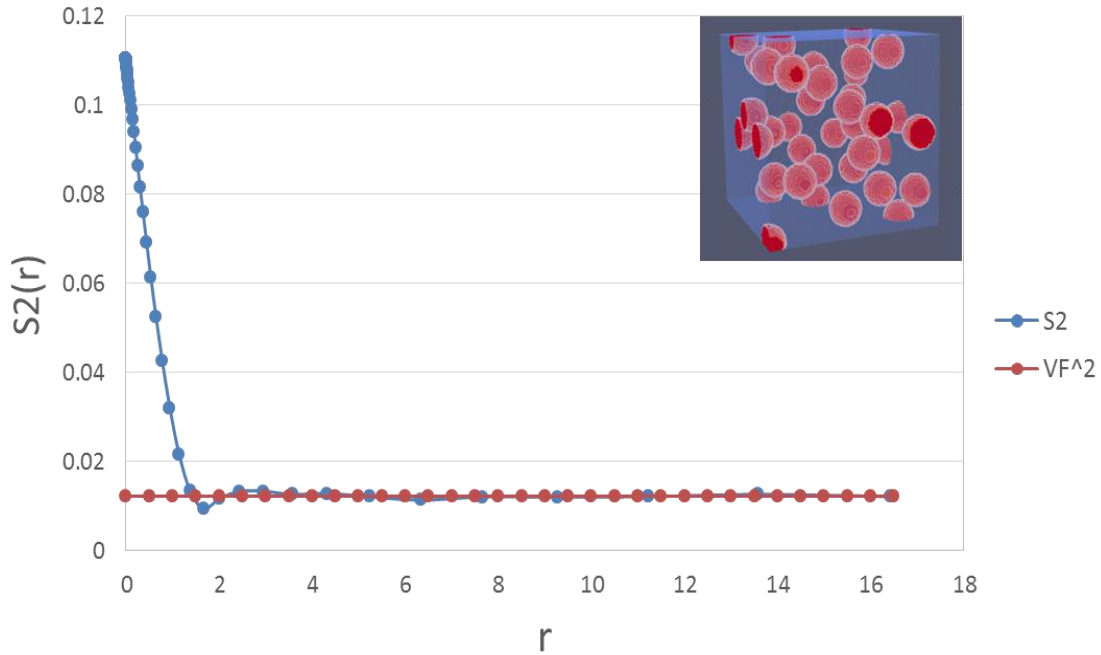


Figure 3.4 Long range behavior of S_2 with r goes to the maximum value compared to the theoretically asymptotic value of a 3D hard sphere packing structure.

For S_3 , since the values will be 3D curve with three parameters, we will only show some special values to prove the accuracy of the sampling approach (Figure 3.5). With fixed r and s , the complexity of S_3 will be reduced to be a function of angle θ . As it is shown in Figure 3.5, when r and s equals to zero, three vertices of the triangle are almost overlap with each other with the length equal to 0.0001. As a result, S_3 will be equal to the volume fraction as

$$\lim_{\substack{r \rightarrow 0 \\ s \rightarrow 0}} S_3(r, s, \theta) = \Phi \quad (3.12)$$

With r and s goes to infinity, all three vertices will be independent with each other representing no long range correlations, and S_3 will be equal to Φ^3 as

$$\lim_{\substack{r \rightarrow \infty \\ s \rightarrow \infty \\ t \rightarrow \infty}} S_3(r, s, t) = \Phi^3 \text{ with } t = (r^2 + s^2 - 2rscos\theta)^{1/2} \quad (3.13)$$

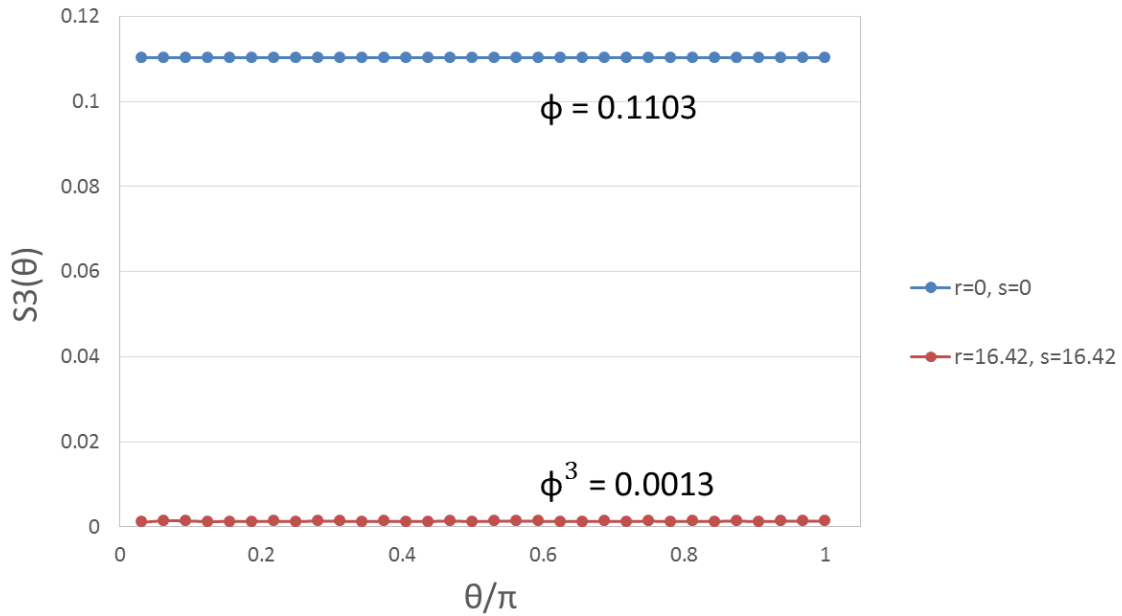


Figure 3.5 S_3 with fixed r and s for both short range and long range values.

3.3 Predicting Mechanical Properties of Polymer Matric Composites

Now we will present the theoretical prediction of Young's modulus of a polymer matrix composite with different volume fraction of reinforced borosilicate spheres [58, 59]. The volume fractions of the glass spheres are 5%, 10%, 20%, and 30%. The Young's modulus and Poisson's ratio of each component in the composite are tested through experiments. Based on the assumption that the structures are statistically homogeneous, isotropic, and linear elastic, the bulk modulus and shear modulus of each component can be calculated. All these values are listed in Table 3.1.

Table 3.1 Mechanical properties of each component of polymer matrix composites

	Young's Modulus (GPa)	Poisson's Ratio	Bulk Modulus (GPa)	Shear Modulus (GPa)
Borosilicate glass	46.1	0.2	25.61	19.21
Polypropylene	1.097	0.42	2.29	0.39

We first compute correlations directly from single 2D slices as shown in Figure 3.6. With the statistical sampling method described earlier, accurate two-point and three-point probability functions can be computed. Using numerical integration and the non-uniform template construction method, Eq. (3.5) and (3.6) can be solved to get the three point parameters ζ_2 and η_2 , and the values are listed in Table 3.2.

Table 3.2 3pt parameters of polymer matrix composites structures with different volume fractions of glass spheres (Single 2D slice)

	5%	10%	20%	30%
ζ_2	0.056	0.043	0.066	0.113
η_2	0.073	0.088	0.164	0.227

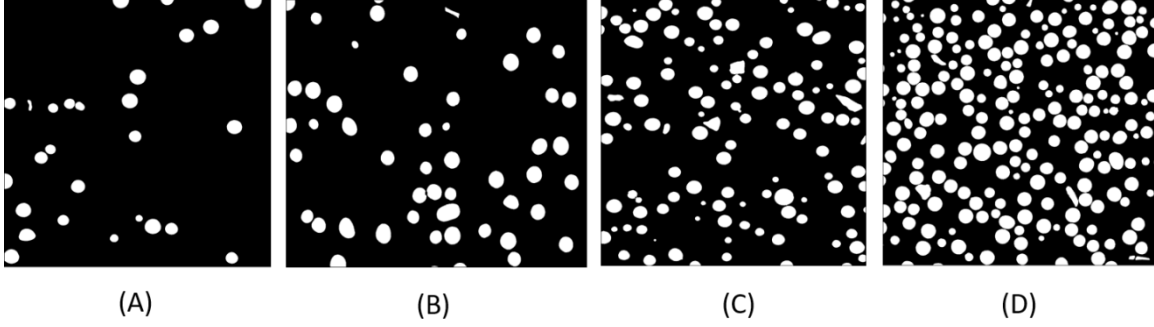


Figure 3.6 2D slice of polymer matrix composite materials with (A) 5%, (B) 10%, (C) 20%, and (D) 30% volume fractions of glass spheres.

The Young's of each individual phase can be obtained from nano-indentation and tensile test. Assuming the system is statistically homogeneous and isotropic (approximation with high accuracy), the bulk and shear modulus of both polymer and glass phase can be acquired following the relationship between bulk and shear modulus with Young's modulus and Poisson's ratio. Now solving Eq. (3.1) and (3.2) will be simple and straight forward and the effective bulk and shear modulus of the composite can be obtained. Hashin-Shtrikman bounds [60] are also computed here to verify the result. The d-dimensional Hashin-Shtrikman bounds on the effective bulk modulus K_e for two-phase composites in which $G_2 \geq G_1$ are

$$K_L^{(2)} \leq K_e \leq K_U^{(2)} \quad (3.14)$$

where

$$K_L^{(2)} = \langle K \rangle - \frac{\varphi_1 \varphi_2 (K_2 - K_1)^2}{\langle \bar{K} \rangle + \frac{2(d-1)}{d} G_1} \quad (3.15)$$

$$K_U^{(2)} = \langle K \rangle - \frac{\varphi_1 \varphi_2 (K_2 - K_1)^2}{\langle \bar{K} \rangle + \frac{2(d-1)}{d} G_2} \quad (3.16)$$

The d-dimensional Hashin-Shtrikman bounds on the effective shear modulus G_e

for two-phase isotropic composites in which $K_2 \geq K_1$ and $G_2 \geq G_1$ are

$$G_L^{(2)} \leq G_e \leq G_U^{(2)} \quad (3.17)$$

where

$$G_L^{(2)} = \langle G \rangle - \frac{\varphi_1 \varphi_2 (G_2 - G_1)^2}{\langle \tilde{G} \rangle + H_1} \quad (3.18)$$

$$G_U^{(2)} = \langle G \rangle - \frac{\varphi_1 \varphi_2 (G_2 - G_1)^2}{\langle \tilde{G} \rangle + H_2} \quad (3.19)$$

and

$$H_i = G_i \left[\frac{dK_i/2 + (d+1)(d-2)G_i/d}{K_i + G_i} \right] \quad (3.20)$$

where φ_1, φ_2 are the volume fractions of polymer matrix and glass spheres, d is the dimension of the system, $\langle K \rangle$ and $\langle G \rangle$ are the ensemble average of bulk and shear modulus, i.e., $\langle K \rangle = \varphi_1 K_1 + \varphi_2 K_2$ and $\langle G \rangle = \varphi_1 G_1 + \varphi_2 G_2$, and $\langle \tilde{K} \rangle$ and $\langle \tilde{G} \rangle$ are the inverse ensemble average, i.e., $\langle \tilde{K} \rangle = \varphi_1 K_2 + \varphi_2 K_1$ and $\langle \tilde{G} \rangle = \varphi_1 G_2 + \varphi_2 G_1$.

Figure 3.7 shows a typical segmented virtual slice of the polymer matrix composite obtained via filtered-back-projection reconstruction (left panel), as well as the probability map (middle panel) associated with the virtual slice computed from 30 simulated synchrotron x-ray tomography projections evenly distributed between 0 and 180 degrees. It can be seen that the probability map clearly captures the geometry and spatial distribution of the particle panel. The right panel of Figure 3.7 shows the two-point correlation function S_2 computed from the probability map.

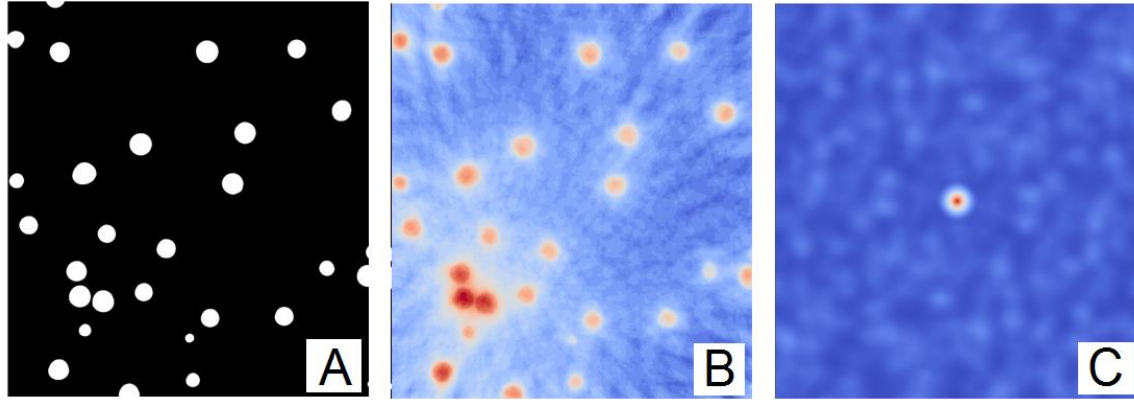


Figure 3.7 Left panel: A segmented virtual slice of the polymer matrix composite with 5% borosilicate spheres obtained via filtered-back-projection reconstruction. Middle panel: The probability map associated with the virtual slice computed from 30 simulated synchrotron x-ray tomography projections evenly distributed between 0 and 180 degrees. Right panel: The two-point correlation function S_2 computed from the probability map.

Figure 3.8 shows the comparison between the effective bulk and shear modulus computed following strong-contrast expansion formulism with the three-dimensional Hashin-Shtrikman bounds. The result shows that the estimated bulk modulus and shear modulus are within the range of higher and lower Hashin-Shtrikman bounds, which validate the estimation. To be specific, the effective modulus is located close to the lower bounds. This is because the spherical shape of the reinforcement phase, borosilicate, has the aspect ratio of 1, which is the same compare to the sphere coating model Hashin and Shtrikman used to derive the bounds.

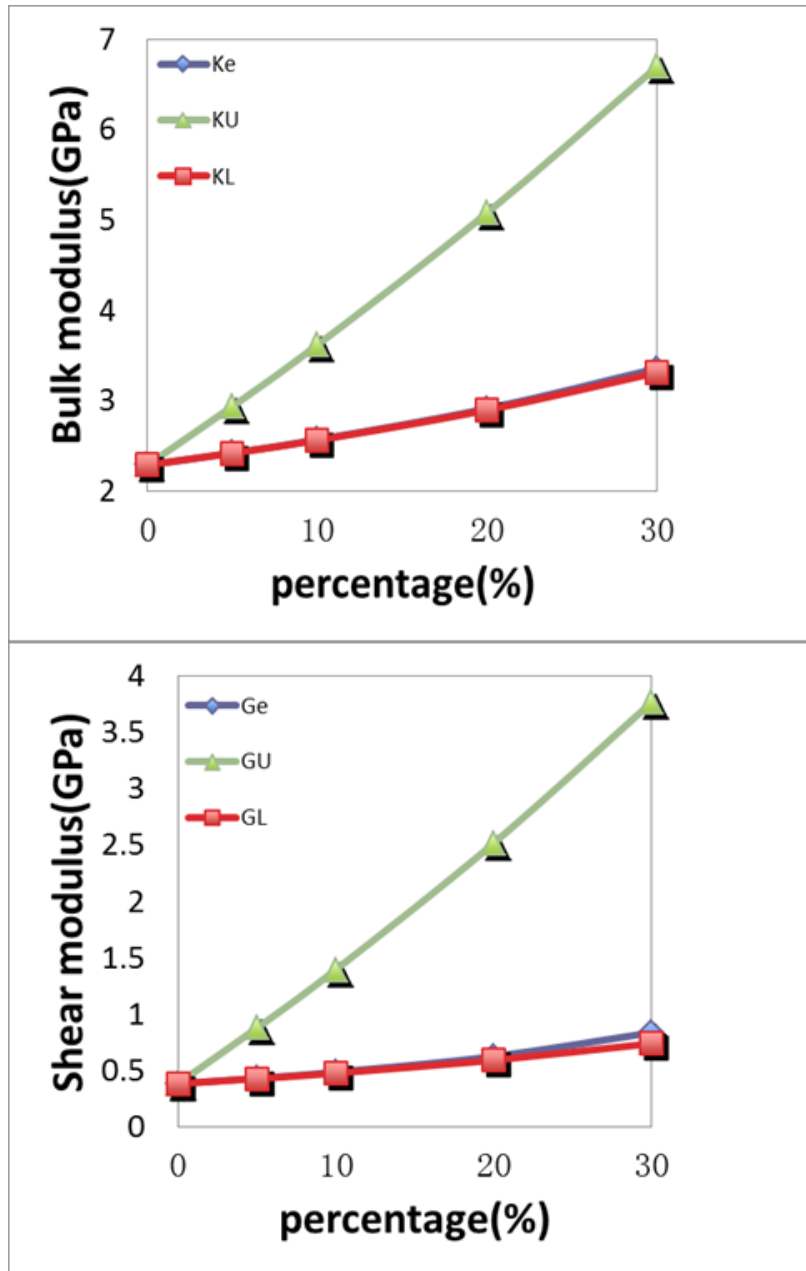


Figure 3.8 Left panel shows the effective bulk modulus with different percentage of borosilicate spheres compared to the Hashin-Shtrikman bounds. Right panel shows the effective shear modulus with different percentage of borosilicate spheres compared to the Hashin-Shtrikman bounds.

Following the assumption that the composite material is statistically homogeneous and isotropic, one can compute effective Young's Modulus E_e based on the relation between E , K and G . Figure 3.9 shows the comparison of estimated Young's modulus from the limited X-ray tomography data using Eq. (3.1) and (3.2) and that obtained from the tensile test for composites with different particle volume fractions. We note that it has been shown for such a composite microstructure, which is statistically homogeneous and isotropic, the lower-order correlation functions S_2 and S_3 of the 3D system can accurately computed from 2D slices, and thus, the elastic moduli can be estimated from 2D slices. Indeed, we can see in Figure 3.8 that the estimated Young's modulus from the probability map associated with single 2D virtual slices for each volume fraction agrees very well with the tensile testing result. Based on the observation, the accuracy of the estimation is increasing with increasing the volume fraction of the glass phase. This is because with small volume fraction, like 5%, local degree of clustering could play an important role in affecting the short range value of S_2 and S_3 , eventually affect the value of three point parameters. This indicates that three point parameters are sensitive to the local degree of clustering. With increasing the volume fraction of the glass phase, high volume fraction can reduce the effect of local degree of clustering, and eventually the accuracy of the estimation can be increased. The value of experimental result, theoretical calculation, and normalized differences are listed in Table 3.3.

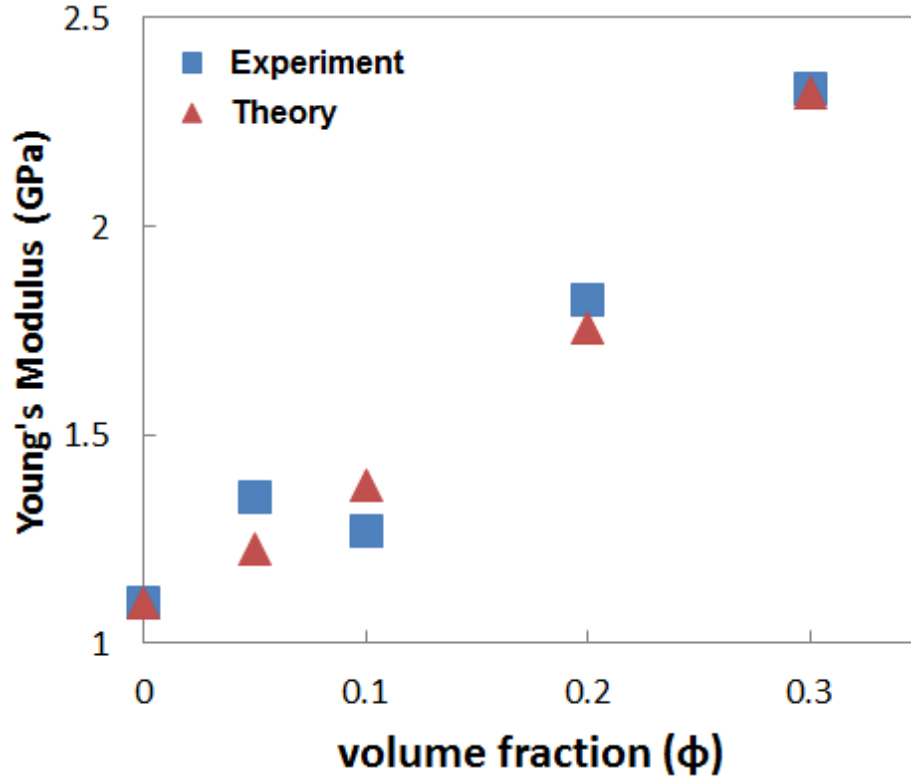


Figure 3.9 Comparison of the Young's modulus estimated from limited x-ray tomography data and that obtained from tensile test for composites with different particle volume fractions.

Table 3.3 Effective Young's Modulus of polymer matrix composites from experimental test, theoretical calculation from single 2D slice, and normalized difference for different volume fractions of glass spheres

	Experiment (GPa)	Theoretical (GPa)	Difference (%)
5%	1.35	1.23	8.96
10%	1.27	1.38	8.5
20%	1.82	1.76	3.35
30%	2.33	2.32	0.43

Same procedure is performed for each sample with multiple 2D slices in order to reduce the bias and increase the accuracy of the theoretical calculation. Here 6 independent 2D slices for each sample is taken, as Figure 3.9 shows the cross-section images for the composite sample with 5% volume fraction of glass spheres. The statistical sampling and following calculation of 3pt parameters are done on each slice, and then compute a numerical average. The results are listed in Table 3.4. Figure 3.10 shows the estimation of effective Young's modulus and the numerical values are listed in Table 3.5. Although the theoretical calculation shows the same value compared to the single 2D slice situation, the normalized difference is smaller due to the difference in higher significant digits.

The excellent approximation even with single 2D slice of a structure as the input strongly implies the structural information in limited data is enough for an accurate property prediction. We note that this procedure can be easily generalized to estimate other linear properties of a heterogeneous material, including electric/thermal conductivity and diffusion coefficient.

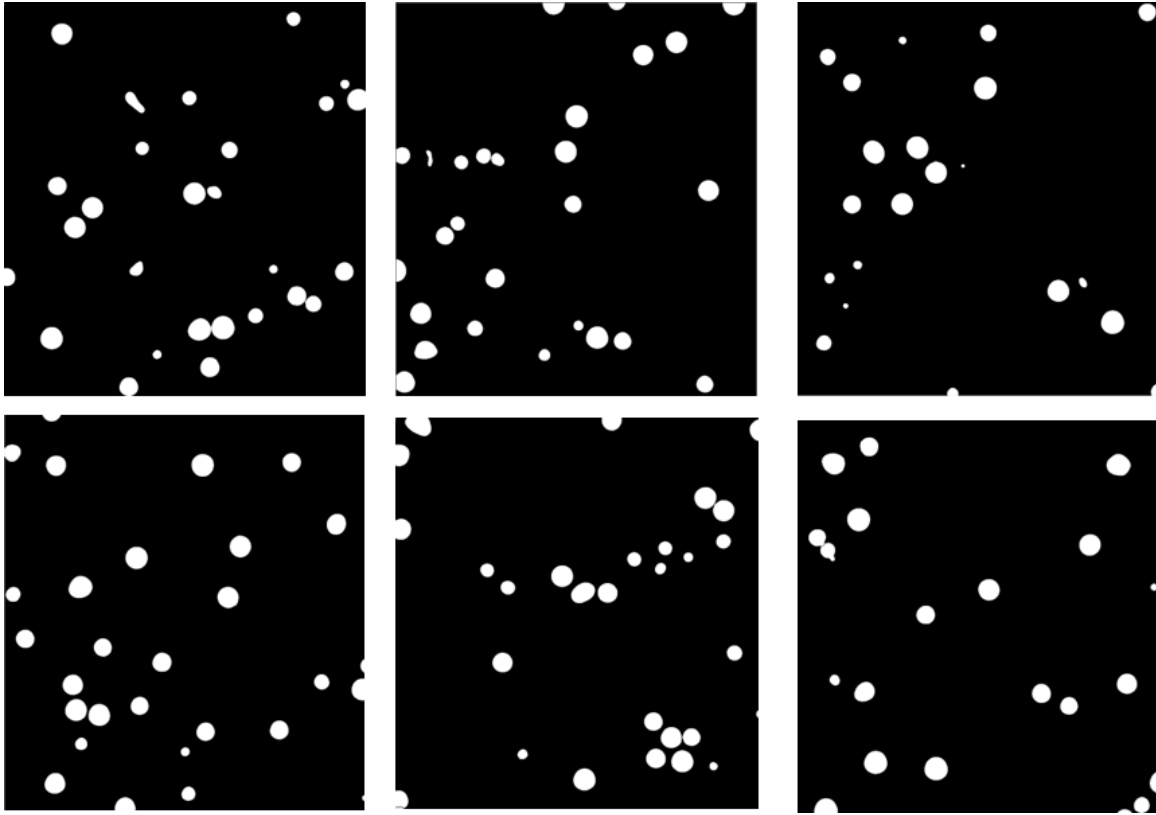


Figure 3.10 6 independent 2D slice of the 5% polymer matrix composites.

Table 3.4 3pt parameters of polymer matrix composites structures with different volume fractions of glass spheres (6 slices)

	5%	10%	20%	30%
ζ_2	0.047 ± 0.021	0.057 ± 0.007	0.07 ± 0.012	0.12 ± 0.01
η_2	0.061 ± 0.022	0.091 ± 0.01	0.136 ± 0.017	0.22 ± 0.019

Table 3.5 Effective Young's Modulus of polymer matrix composites from experimental test, theoretical calculation from 6 independent 2D slices, and normalized difference for different volume fractions of glass spheres

	Experiment (GPa)	Theoretical (GPa)	Difference (%)
5%	1.35	1.23 ± 0.02	8.89
10%	1.27	1.38 ± 0.03	7.97
20%	1.82	1.76 ± 0.06	3.3
30%	2.33	2.32 ± 0.05	0.39

3.4 Predicting Mechanical Properties of SiC/Al Composites

Particle reinforced metal matrix composites (MMCs), consisting of a light alloy matrix such as aluminum, reinforced with ceramic particulates, i.e., silicon carbide, exhibit enhanced performance over conventional monolithic metal alloys. Adding reinforced particles into the metal matrix will improve the strength and stiffness, and fatigue resistance [61-64]. The composites will have a better performance at elevated temperature than unreinforced alloys. Moreover, the addition of reinforcement particles will not significantly increase the weight, while maintaining cost at an acceptable level.

Silicon carbide reinforced aluminum matrix composites have been well studied in the last couple of decades, and most of their fatigue behavior have been understood. As shown in Table 3.6, the addition of high stiffness ceramic reinforced particles can increase the overall strength and stiffness compare to the unreinforced alloys. There are several key factors that affect the overall fatigue performance, including the volume fraction of the reinforcement particles, the particle sizes, the microstructure of the matrix, and the working temperature, etc. Here a sample of SiC/Al composite will be tested using

the aforementioned statistical sampling method and the estimated Young's modulus will be compared with reference. The SiC/Al composite sample is tested in the lab and the information of each component and as a composite is provided by Dr. Nikhilesh Chawla's group in Arizona State University as a comparison to the theoretical calculation. The properties of each component, 3pt parameters computed using statistical sampling method, and the estimated Young's Modulus using strong contrast expansion method are listed in Table 3.7. One can confirm an excellent estimation is made by comparing the theoretical calculation result with the reference value listed in Table 3.6.

Table 3.6 Tensile Properties of Reinforced and Unreinforced 2080 Al [60]

	Yield Strength (MPa)	Ultimate Strength (MPa)	Elastic Modulus (GPa)	Strain to Failure (Pct)
30%, F-1000	575	639	119	2.27
20%, F-1000	539	593	107	3.14
10%, F-1000	528	574	89	6.34
20%, F-600	522	563	106	2.88
20%, F-280	457	478	95	1.02
Unreinforced	490	525	75	9.0

Table 3.7 Mechanical properties of each component, 3pt parameters and estimated Young's modulus of SiC reinforced Aluminum composite material

	Young's Modulus (GPa)	Poisson's ratio	3pt parameters		Effective Young's Modulus (GPa)
SiC	450	0.17	ζ_2	0.179	93.88
Al	75	0.31	η_2	0.214	

3.5 Summary

We accurately estimated the effective elastic properties for a set of polymer matrix composites with different volume fractions of borosilicate spheres and SiC/Al composites following the procedure of strong-contrast expansion formulism. Utilizing the statistical sampling approach to evaluate the two-point and three-point probability functions from a couple of slices of the polymer matrix composites and SiC reinforced Aluminum composites structure and numerical integration results in accurate calculation of three point parameters. Following strong contrast expansion formulism one can estimate the effective bulk modulus and shear modulus, and the comparison with Hashin-Shtrikman bound validates the correctness of result. And the comparison of the estimated effective Young's modulus with the experimental result and reference shows the accuracy of our estimation. Since all the work are done based on a couple of slices instead of the whole material, the requirement of the experimental data can be significantly reduced, which can save a huge amount of human effort and data collecting and saving time and space. And we can apply this work to estimate other properties like conductivity and permeability, etc.

CHAPTER 4

STOCHASTIC RECONSTRUCTION USING LIMITED X-RAY TOMOGRAPHY DATA

4.1 Stochastic Reconstruction Procedure via Simulated Annealing

In this section, we first introduce the general simulated annealing procedure that formulates the reconstruction problem as an inverse optimization problem and allows one to generate virtual microstructures compatible with prescribed structural information and statistics. Then, we describe in detail the specific algorithms for stochastic reconstruction based on both cone-beam and parallel beam projection geometries.

4.1.1 Simulated Annealing Reconstruction Procedure

In general, consider a 3D material microstructure digitized and represented by a 3D array M , whose entry value M_{ijk} indicates the local state of that voxel (e.g., the phase that the voxel belongs to). An experiment performed to probe the microstructure of the material generates a set of structural data, which we noted by D . A mathematical transformation F is introduced which transform the microstructure to the structural data. The relation between the 3D array M and the structural data set D can be presented as,

$$D = F\{M\} \quad (4.1)$$

In the x-ray tomography microscopy, the structural data D are 2D projections of the 3D microstructure from different projections angles. The 3D microstructure can be fully determined if the attenuation coefficient of each voxel (i.e., the phase of the voxel) is known. Thus, the value of each voxel of the 3D array is the attenuation coefficient associated with the phase of that voxel belongs to. The 2D projections record the attenuated intensities (due to absorption in our case) of the x-rays passing through the

materials sample. In particular, consider the schematic projection geometry shown in Figure 4.1, the intensity of the projection associated with the projection angle θ at position r is given by,

$$D(r, \theta) = I_0 \exp[-\int M(x, y, z) ds] \quad (4.2)$$

where I_0 is the initial intensity of the incident x-ray, and s is the path along which the x-ray travels. With a sufficiently large number of 2D projections, typically hundreds or even thousands of projections at successive projection angles evenly distributed in the interval $[0, \pi]$, traditional computed tomographic reconstruction techniques, such as the filtered-back-projection (FBP) method [39, 40] and algebraic reconstruction techniques (ART) [41, 42], can be utilized to generate accurate 3D representation of the material microstructure. However, if only a limited number of projections are available, the accuracy of the reconstructions using FBP and ART could be dramatically reduced. In addition, such methods typically produce a 3D grayscale map of the attenuation coefficients for the material of interest. Tedious segmentation is usually required to resolve the actual material microstructure.

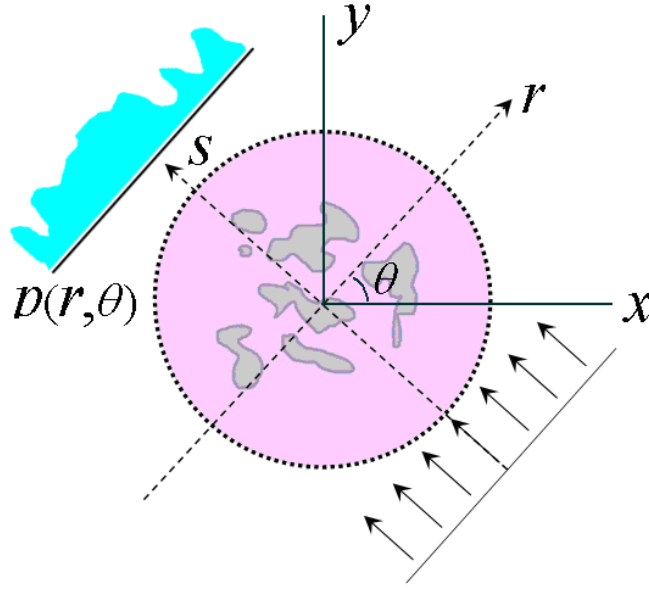


Figure 4.1 A schematic illustration of parallel-beam projection geometry in 2D.

In order to reconstruct 3D microstructure M from *limited* projection data set D and the associated mathematical transformation F , we apply a reconstruction technique that inspired from Yeong-Torquato’s stochastic optimization scheme to generate virtual microstructures from prescribed statistical morphological descriptors of the microstructure, i.e., various correlation functions associated with the material’s phases [65]. In particular, we formulate the reconstruction problem as an “energy” minimization problem, where the energy functional E is defined as the square difference between the target data set D and the corresponding data set D^* from a trial microstructure M^* ,

$$E = |D - D^*|^2 \quad (4.3)$$

The trial microstructure is randomly generated (i.e., by assigning a phase to each entry of the 3D microstructural array with certain probability); and the associated projection data set D^* is then calculated from Eq. (4.1).

The energy minimization problem is solved using the simulated annealing method [66]. We note that other techniques have also been employed to solve such optimization problems [67, 68]. Specifically, the system is given an initial trial microstructure M_o^* , which contains a fixed number of voxel for each phase. Then the positions of two randomly selected voxels with different phases are switched, which results in a new trial microstructure M_n^* . The transform function F is applied to both M_o^* and M_n^* to compute the simulated projection data sets D_o^* and D_n^* , which are used to compare with target data set D to calculate energy E_{old} , and E_{new} according to Eq. (4.3). The probability that the new trial microstructure will be accepted and that the old trial microstructure be replaced is given by,

$$P_{acc}(old \rightarrow new) = \min \left\{ 1, \exp\left(\frac{E_{old}}{T}\right) / \exp\left(\frac{E_{new}}{T}\right) \right\} \quad (4.4)$$

where the parameter T is an effective temperature used to control the acceptance rate for energy-increasing trial microstructures. In the beginning of the simulated annealing process, the parameter T is chosen to be relatively high in order to achieve an acceptance probability of approximately 0.5. Then T is gradually reduced according to a prescribed cooling schedule as the simulation proceeds in order to allow the energy to converge to a very small value if not zero (See Figure 4.2). In the current work we choose an exponential cooling schedule, i.e., $T(t)/T_0 = \gamma^t$, where $0.95 < \gamma < 0.99$. As T gradually decreases, the acceptance probability for energy-increasing trail microstructure will also decrease. Eventually the energy converges to a (local) energy minimum, which is associated with microstructure that is very close to the actual material structure. In practice, the global energy minimum is extremely difficult to reach, and we claim the reconstruction is successfully accomplished if energy E drops below a prescribed

tolerance value, which is chosen to be 10^{-4} here.

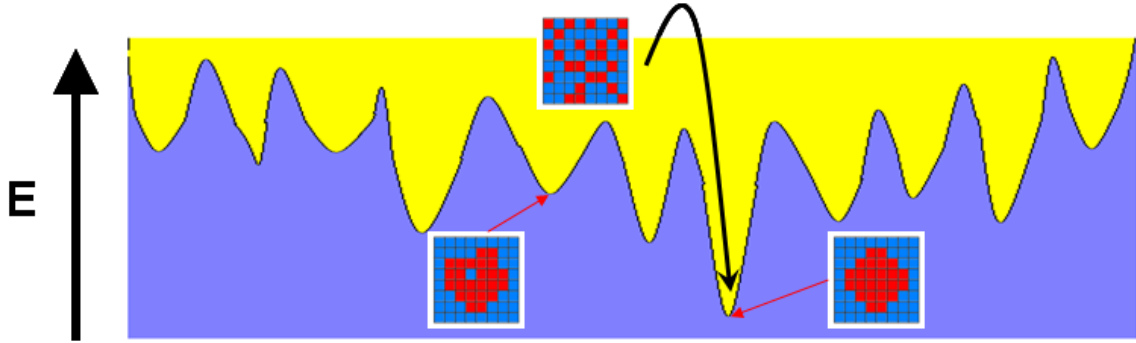


Figure 4.2 Schematic illustration of the stochastic reconstruction procedure using the simulated annealing method: Energy-increasing trial microstructures can be accepted initially in order to increase the probability for the system to converge to the global or very deep local energy minima.

4.1.2 Algorithmic Details for Parallel-Beam Geometry

For the parallel-beam projection geometry, a set of parallel rays are sent through the material sample from different projection angles and the attenuated intensities of the x-rays passing through the sample are recorded via a detector behind the sample. As shown in Figure 4.3, we denote the vector pointing from the center of the detector to the position where an attenuated x-ray hits the detector by r , and denote the projection angle by θ , then the total attenuation of the ray $D(r, \theta)$ due to the absorption is given by [28],

$$D(r, \theta) = \ln\left(\frac{J_0}{J}\right) = -\int \mu(x, y, z) ds \quad (4.5)$$

where J_0 is the initial intensity of the x-ray, J is the attenuated intensity recorded by the detector, and $\mu(x, y, z)$ is the position dependent attenuation coefficient of the heterogeneous materials. For a two-phase (binary) material,

$$\mu(x, y, z) = \mu_1 I^{(1)}(x, y, z) + \mu_2 I^{(2)}(x, y, z) \quad (4.6)$$

where μ_i is the attenuation coefficient of phase i , and $I^{(i)}$ is the indicator function of phase i , which equals to 1 if the voxel is in phase i , and 0 otherwise, i.e.,

$$I^{(i)}(x, y, z) = \begin{cases} 1, & (x, y, z) \in V^{(i)} \\ 0, & \text{otherwise} \end{cases} \quad (4.7)$$

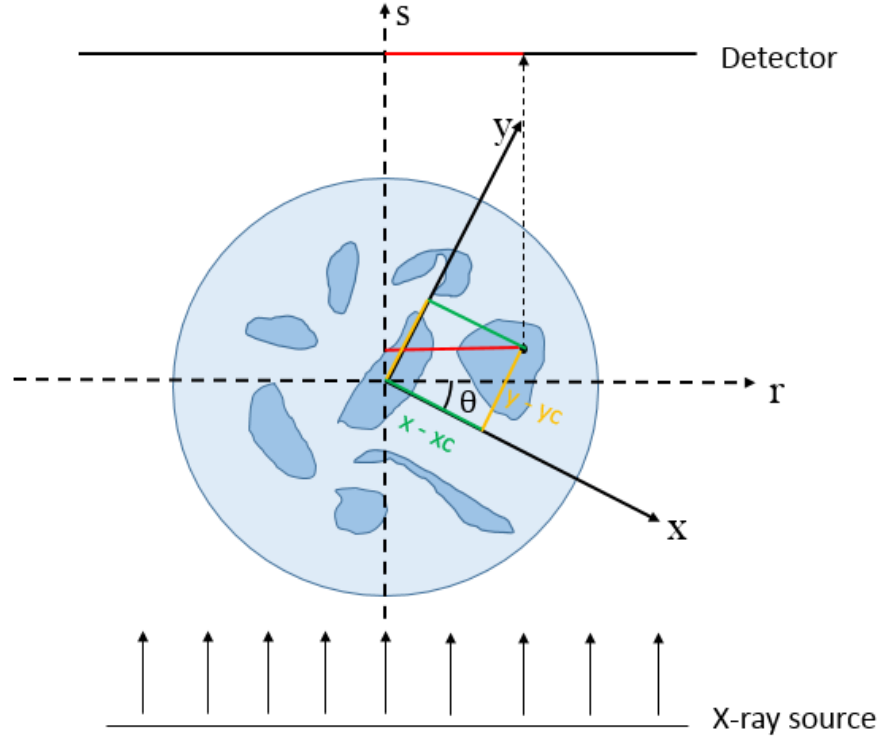


Figure 4.3 Schematic illustration of geometrical relation that maps a voxel position to the corresponding detector bin in the parallel-beam projection geometry.

In a tomographic reconstruction, the original continuous 3D material sample is discretized and represented as a 3D array, whose entry values indicate which phase the voxel belongs to (e.g., the phase-specific attenuation coefficients). In this formulation, the attenuation intensities recorded by the detector at different projection angles are

transformed to the total intensity drop ΔJ as the x-ray pass through the material sample along a particular path, which can be expressed as the summation of the attenuation coefficient μ_i of each voxel along the path multiplied by the length of that voxel l , i.e., $\Delta J = \sum \mu_i l$. Therefore, for the parallel-beam geometry, the contribution to the total intensity drop at a particular detector bin due to each voxel can be computed separately. For each voxel in the material, the position of its projection on the detector (i.e., the position of the detector bin whose intensity drop is affected by that voxel) relative to the center of the detector is a function of the position of the voxel in the material sample as well as the geometric center of the sample. As shown in Fig. 3, when rotating the material sample clockwise by an angle θ , the position of the projection of a voxel on the detector (X, Z) can be calculated as,

$$X = (x - x_c) * \cos\theta + (y - y_c) * \sin\theta \quad (4.8)$$

$$Z = z - z_c \quad (4.9)$$

where x, y, z are the coordinates of each voxel in the material sample and x_c, y_c, z_c are the coordinates of the center of the sample. We note that due to the parallel nature of the incident rays, a voxel and the vertical coordinate of the projection of a voxel on the detector is independent of the projection angles and is a function of the vertical coordinate of the voxel in the material sample alone.

The aforementioned formulation allows us to devise a highly efficient method to compute the energy E_{new} for a new trial microstructure, based on E_{old} of the old trial microstructure. Specifically, when the positions of two voxels associated with different phases are switched to generate a new trial microstructure, only the total attenuation values in two detector bins containing the two exchanged voxels are affected and the total

attenuation values in all the other bins remain the same. Therefore, there is no need to re-compute the total attenuations for all bins for the new trial microstructure and it is sufficient to update the two affected bins for each projection angle, i.e.,

$$\Delta J_i(\theta) \leftarrow \Delta J_i(\theta) + (\mu_j - \mu_i) \cdot l \quad (4.10)$$

where $\Delta J_i(\theta)$ is the total attenuation value at the detector bin associated with voxel i at projection angle θ , μ_i and μ_j are respectively the attenuation coefficients for voxel i before and after the phase switch, and l is the linear size of the voxel. We note that the complexity of this energy update method scales linearly with the number of projections and is independent of the size of the reconstruction domain nor the size of the 3D array representing the material microstructure. Therefore, it is highly efficient when the number of projections used in the reconstruction is small.

4.1.3 Algorithmic Details for Cone-Beam Geometry

Different from the parallel-beam projection geometry, the cone-beam geometry has a point x-ray source, and the x-rays are radially emitted from the source to form a cone pattern. A consequence of such projection geometry is that the spatial density of incident rays is higher at the front side of the material sample which is close to the source and is lower at rear side of the sample. Therefore, each voxel may affect the total attenuation values in multiple detector bins and thus, a detector-bin-based projection method is used to compute the contribution of each voxel to the total attenuation data.

As shown in Fig. 4.4, a set of prescribed paths connecting the center of each detector bin and the point x-ray source are constructed. We use these paths to simulate the x-rays passing through the sample and hitting particular detector bins which result in a recorded total attenuation. The total attenuation in each detector bin is computed as the

summation of the intensity drop due to each voxel along the path that connects that bin and the x-ray source. We note that at a specific projection angle, a voxel can affect multiple detector bins. Specifically, if the distance from the center of a voxel to an x-ray path is smaller than half of the voxel linear size $l/2$, we consider this voxel contributes $\mu_i l_v$ to the total attenuation in the bin that the x-ray path hits, where μ_i is the attenuation coefficient of the phase in the voxel, and l_v is the line segment of the x-ray path in the voxel, i.e.,

$$l_v = \sqrt{R^2 - d^2} \quad (4.11)$$

where R is the radius of the inscribed circle of a voxel, which is equal to $l/2$, and d is the distance from the center of the voxel to the x-ray path.

At different projection angles, the detector bins affected by a voxel are generally different. Such geometric maps are independent of the phases the voxels belong to and thus, are acquired only once in the beginning of the simulation. In other words, at each projection angle, the voxels affect each detector bin are identified and saved for subsequent calculation and update of the energy for trial microstructures.

Similar to the parallel-beam case, the energy of a new trial microstructure can be efficiently obtained based on that of the old trial microstructure, without re-computing the entire set of total attenuations. In particular, once two voxels belonging to different phases are switched, the total attenuations in the bins affected by the two voxels are updated according to Eq. (4.10). However, in the cone-beam case, at a specific projection angle, there are generally more than one bin that are affected by a single voxel. The associated changes of the total attenuation values in the affected bins should all be computed and updated accordingly.

Finally, we note that in both parallel-beam and cone-beam cases, the resolution of the reconstruction domain (i.e., the number of voxel per unit length) should be carefully chosen. Too low resolution leads to low-accuracy reconstructions in which the detailed geometrical features of the phases are not resolved and the simulated annealing procedure usually does not converge for such systems. Very high resolution result in high-quality reconstructions but would be too computationally expansive.

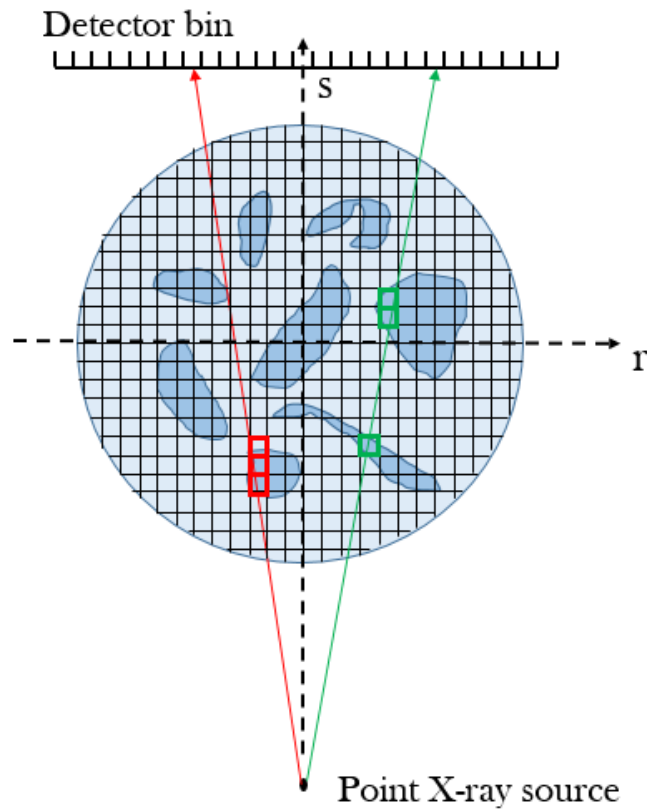


Figure 4.4 Schematic illustration of detector-bin-based projection method for cone-beam geometry. For each detector bin, a path connecting the point X-ray source to the bin is created. The number of voxels in the discrete sample domain in the target phase along that path is then counted. The total intensity drop (i.e., attenuation) along that path is computed and record for that bin.

4.2 Stochastic Reconstruction Using Simulated X-ray Tomographic Projections

In this section, we validate the aforementioned stochastic procedure by applying it to reconstruct a number of two-phase heterogeneous materials from simulated x-ray projections in both parallel-beam and cone-beam geometry. Specifically, a Fontainebleau sandstone microstructure [10] consisting of percolating rock and void phase and a dense packing of hard ellipsoids [69] are used as target systems, for which the associated 3D microstructure arrays are already known. Simulated projections are generated by computing the total attenuation along specific paths of incident x-rays using Eq. (4.5) for different projection geometries. We note that we first consider simulated x-ray projections because such data are noise free and thus, enable us to systematically investigate the information content of the x-ray tomography data. Without loss of generality, we use $\mu_1 = 1$ for the solid phase (rock phase for sandstone and particle phase for the packing) and $\mu_2 = 0$ for the void phase for generating the simulated projections and the reconstruction.

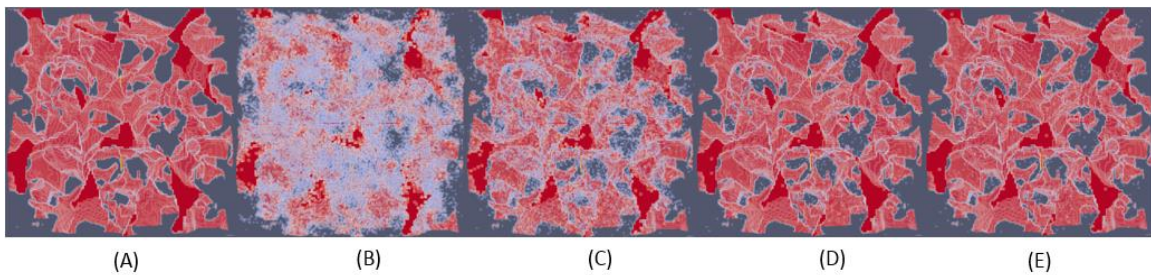


Figure 4.5 Reconstructions of the sandstone microstructure (A) from 5 (B), 10 (C), 20 (D) and 30 (E) simulated projections generated in parallel-beam geometry.

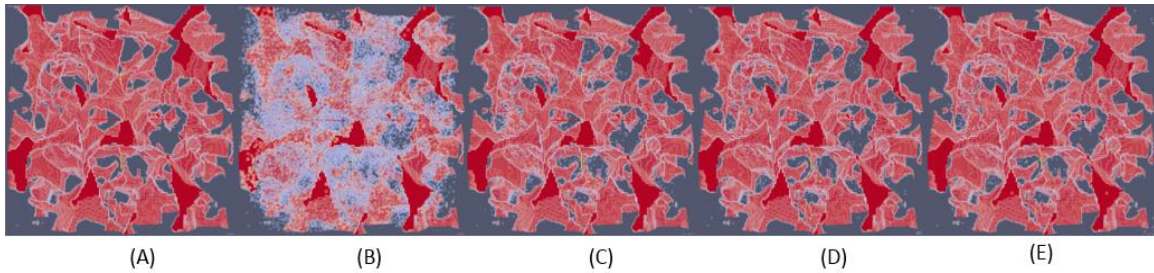


Figure 4.6 Reconstructions of the sandstone microstructure (A) from 5 (B), 10 (C), 20 (D) and 30 (E) simulated projections generated in cone-beam geometry.

The reconstructions of the sandstone microstructure from simulated projections in parallel-beam and cone-beam geometries are respectively shown in Figure 4.5 and Figure 4.6. The reconstructions of the hard-ellipsoid packing from simulated projections in parallel-beam and cone-beam geometries are respectively shown in Figure 4.7 and Figure 4.8. The linear size of the simulation domain is 200 voxel length, which is roughly 400 μm . A total of 500 annealing stages and a cooling schedule of 0.98 are used for these reconstructions. In each figure, panel (A) shows the target microstructure and panels (B) to (E) respectively show the reconstructions using 5, 10, 20 and 30 simulated projections. The angles associated with these projections are evenly distributed within the interval between 0 and 180 degrees.

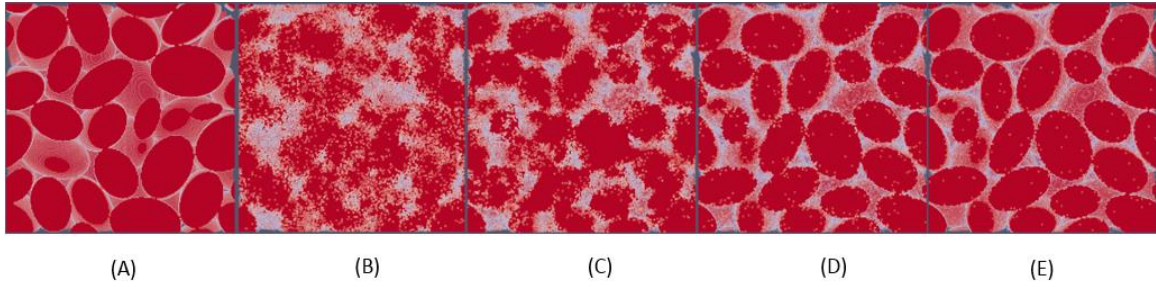


Figure 4.7 Reconstructions of a dense packing of hard ellipsoids (A) from 5 (B), 10 (C), 20 (D) and 30 (E) simulated projections generated in parallel-beam geometry.

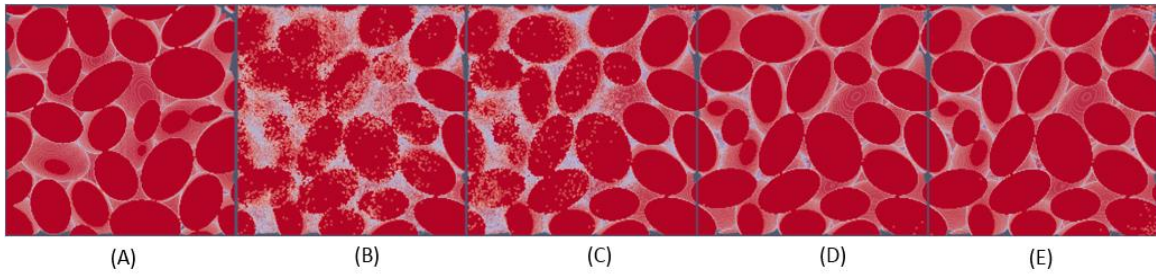


Figure 4.8 Reconstructions of a dense packing of hard ellipsoids (A) from 5 (B), 10 (C), 20 (D) and 30 (E) simulated projections generated in cone-beam geometry.

It can be clearly seen that an initial increase of the number of projections N_θ (e.g., from 5 to 10 and from 10 to 20) can lead to significantly improved reconstructed microstructures. However, further increasing N_θ (e.g., from 20 to 30) does not result in much improvement of the accuracy of the reconstructions. Simulated projections are used here for us to investigate the information content of the projection data. Our reconstruction results clearly show that a relative small number of noise-free synchrotron x-ray tomography projections (e.g., 20 to 30) already contain sufficient structural information for a highly accurate rendition of the material microstructure. Moreover, the

successful reconstructions strongly suggest that our stochastic procedure can utilize the available structural information contained in limited-angle projection data in a highly efficient manner.

In order to quantify the accuracy of the reconstructions, we employ an accuracy metric that measures the deviation of the reconstructed and target microstructure [70],

$$M_a = \sum_{x,y,z} |I(x, y, z) - I^*(x, y, z)| / N^3 \quad (4.12)$$

where $I(x, y, z)$ is the indicator function of the phase of interest in the reconstructed microstructure, and $I^*(x, y, z)$ is the indicator function of the corresponding phase in the target microstructure, N is the linear size of the system and a cubic domain is assumed here. It is easy to see that this metric is actually the fraction of the misplaced voxels over the total number of voxels in the reconstructed microstructure. Figure 4.9 shows M_a as a function of N_θ for the sandstone and hard-ellipsoid packing structures that we studied, which quantitatively indicates that the accuracy of the reconstructions initially increase rapidly as the number of projections increases [cf. Figures 4.5 to 4.8]. When $N_\theta > 20$, the reconstructed microstructure virtually perfectly matches the target structure (with $M_a \sim 0$) and thus, further increasing number of projections does not lead to improved reconstructions.

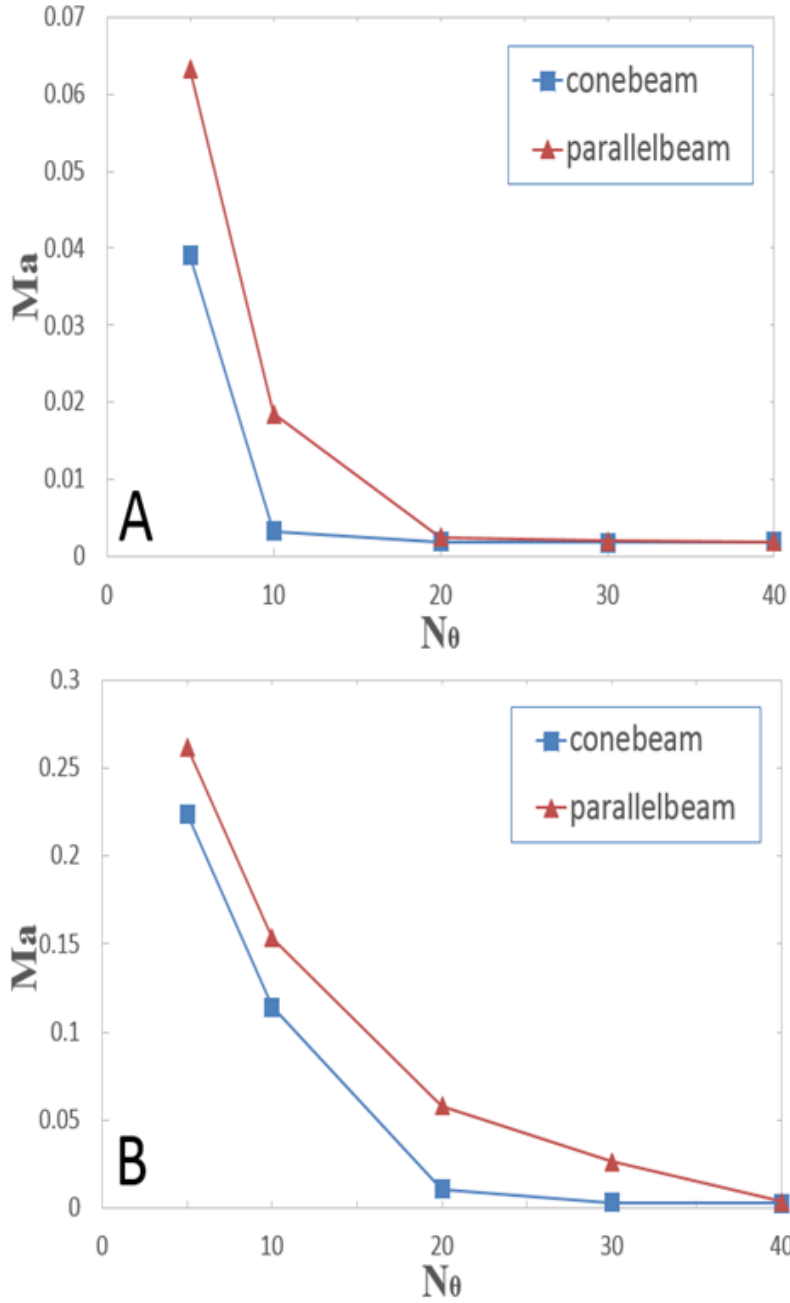


Figure 4.9 The accuracy metric M_a as a function of N_θ for the reconstructions of the sandstone microstructure (A) and the hard-ellipsoid packing (B). In both systems, M_a initially decays rapidly as N_θ increases and virtually decays to 0 beyond $N_\theta = 20$.

In addition, as shown in Figure 4.9 (A) and (B), for a given number of projections, the cone-beam geometry results in more accurate reconstructions compared to the parallel-beam geometry. This is because the stochastic reconstruction from limited structural information strongly depends on spatial correlations among the voxels of different phases encoded in the partial structural information. Due to the nature of the cone-beam geometry, each voxel affects multiple bins at the detector for each projection angle and thus, the cone-beam data (i.e., the total attenuation values in each detector bin) possess stronger correlations than the parallel-beam data. Therefore, during the reconstruction process, switching two voxels leads to a larger change of energy in cone-beam geometry. This facilitates the convergence of the reconstruction process. We emphasize that the above analysis assumes perfectly monochromatic x-rays. In practice, due to polychromatic nature of the incident rays and other artifacts, the cone-beam data might lead to less accurate reconstruction compared to the parallel beam data.

4.3 Reconstructions from Limited-Angle X-ray Tomographic Data

In this section, we apply the stochastic procedure to reconstruct Sn-sphere-clay-matrix systems from limited-angle tomography data [71]. Two microstructures (i.e., spatial distributions of Sn-sphere in clay matrix) are studied. One system consists of Sn-spheres embedded close to the surface of a cylinder-like clay matrix with a helical arrangement, which was originally made to test and fine-tune the alignment of a lab-scale cone-beam x-ray tomography microscopy at Arizona State University (ASU) [72]. The other system is a random distribution of Sn-spheres in clay matrix. For each system, 30 parallel-beam synchrotron projections evenly distributed from 0 to 180 degrees that are obtained at Advanced Photon Source, Argonne Nation Lab and 30 cone-beam projections

obtained via the lab-scale cone-beam tomography microscopy at ASU are used as input for our stochastic reconstruction procedure. The procedures for acquiring the projection data are described elsewhere [72]. The attenuation coefficients for the tin and clay used in our reconstructions are normalized values with respect to the attenuation coefficient of air and geometrical parameters, i.e., the linear voxel length in the reconstruction domain.

The reconstructions of the helical arrangement of Sn-sphere in clay from cone-beam and parallel-beam data are respectively shown in Figure 4.10 and 4.11. For the cone-beam data, a reconstruction domain of 136 by 136 by 152 voxels is used and 500 annealing stages with a cooling schedule 0.98 is employed in the stochastic optimization. The normalized attenuation coefficients of clay and Sn are respectively 0.0022 and 0.0784. The linear size of domain is roughly 2200 μm . For the parallel-beam data, a reconstruction domain of 303 by 303 by 201 voxels is used and 1000 annealing stages with a cooling schedule 0.98 is employed in the stochastic optimization. The normalized attenuation coefficients of clay and Sn are respectively 0.0026 and 0.0751. The linear size of domain is roughly 1250 μm . Also shown in the figures are the raw projections, i.e., intensity maps showing the total attenuation due to absorption as the x-rays passing through the material sample. In both cases, both the helical distribution and the shape of Sn-spheres are very well resolved in the reconstructions. However, a closer inspection reveals that the sphere phase is better reconstructed using the parallel-beam data. This is because during the reconstruction process, a single attenuation coefficient value is used for each distinct phase, which assumes that the x-rays are monochromatic. Such an assumption is valid for the parallel-beam synchrotron data, but is not true for the cone-beam data. We note that the polychromatic nature of x-rays used in acquiring the cone-

beam data as well as the beam hardening effect [72] also causes significant artifacts in the reconstruction using the filtered-back-projection reconstruction method.

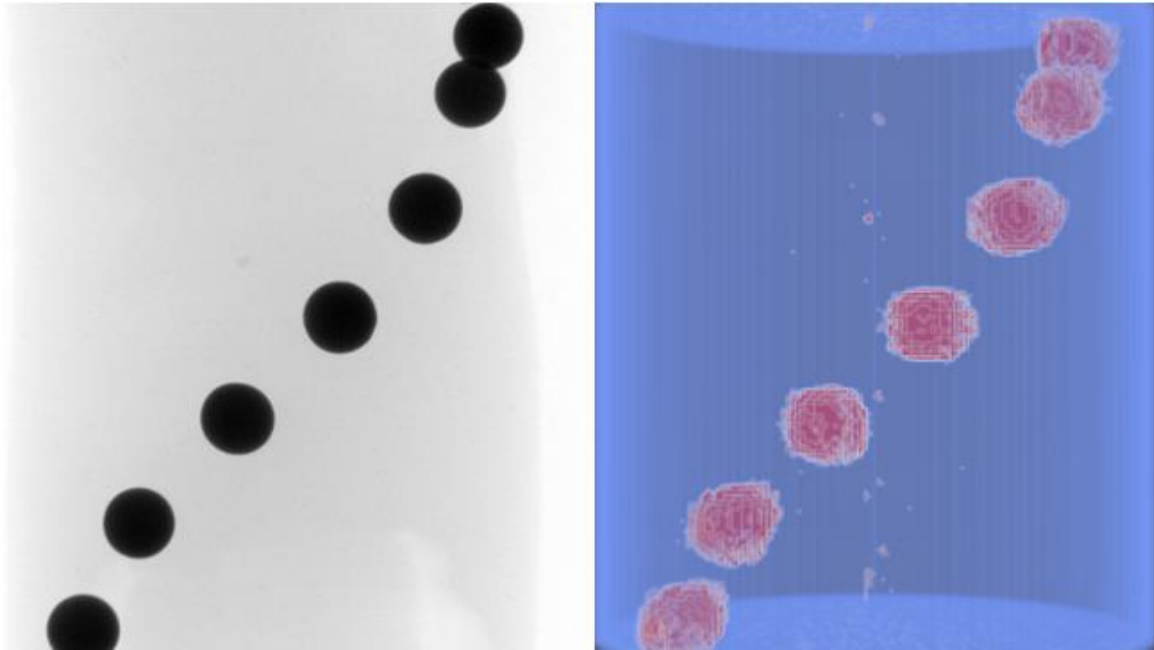


Figure 4.10 Reconstruction of the helical arrangement of Sn-spheres in clay from cone-beam data. (A) A projection (i.e., the total attenuation intensity) associated with the projection angle of 0° . (B) Reconstructed microstructure from 30 projections evenly distributed in the interval between 0 and 180 degrees.

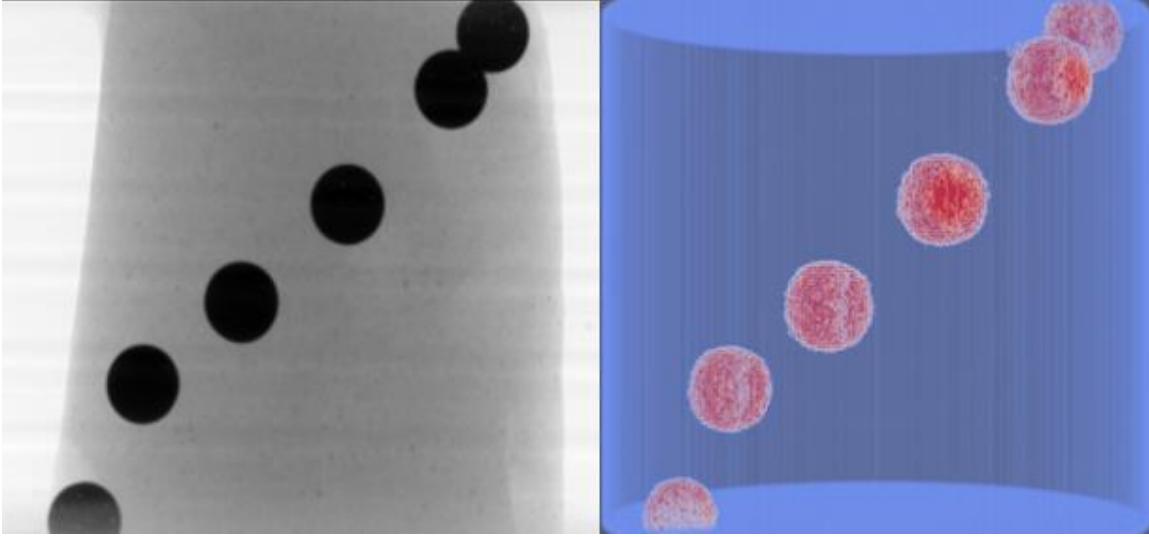


Figure 4.11 Reconstruction of the helical arrangement of Sn-spheres in clay from parallel-beam data. (A) A projection (i.e., the total attenuation intensity) associated with the projection angle of 0° . (B) Reconstructed microstructure from 30 projections evenly distributed in the interval between 0 and 180 degrees.

We also apply the stochastic procedure to reconstruct a random distribution of Sn-spheres in clay, whose microstructure resembles that of a particle-reinforced composite material. The reconstruction of such a system from parallel-beam data is shown in Figure 4.12. Specifically, a reconstruction domain of 303 by 303 by 203 voxels is used and 1000 annealing stages with a cooling schedule 0.98 is employed in the stochastic optimization. The normalized attenuation coefficients of clay and Sn are respectively 0.0026 and 0.0697. The linear size of domain is roughly 1300 μm . Also shown in the figures are the raw projections. Again, it can be clearly seen that the system has been successfully reconstructed with well resolved sphere shape and spatial distributions. We emphasize that in the reconstructions via FBP method using only 30 projections, which are not

shown here, neither the spatial distribution nor the sphere shape can be resolved. In addition, the FBP reconstruction yields a grayscale map of the attenuation coefficients and further segmentation is required to recover the binary microstructure. In this aspect, our stochastic procedure is clearly superior to the FBP method. These examples clearly illustrate the utility and efficiency of the stochastic reconstruction procedure.

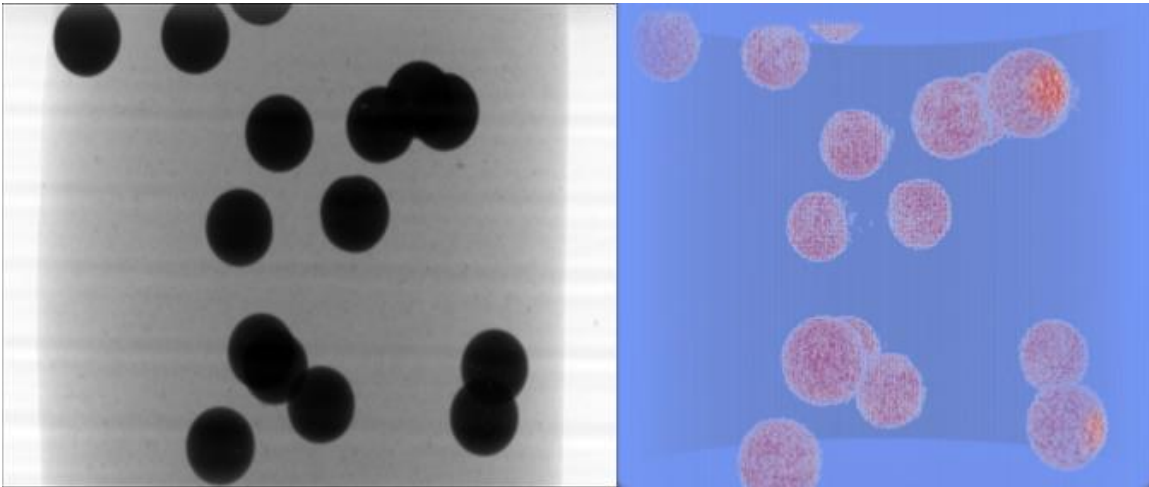


Figure 4.12 Reconstruction of a random distribution of Sn-spheres in clay from parallel-beam data. (A) A projection (i.e., the total attenuation intensity) associated with the projection angle 0° . (B) Reconstructed microstructure from 30 projections evenly distributed in the interval between 0 and 180 degrees.

4.4 Stochastic Reconstruction with Multi-modal Data Fusion

The structural information contained in most raw imaging data such as X-ray tomographic radiographs (projections) and diffraction data have not been used directly. And material reconstruction and post-processing procedures are typically employed to first generate a 3D microstructure for subsequent analysis. In Chapter 2, a novel

procedure which named “probability map” has been described in detail that can “leapfrogs” the tedious 3D reconstruction processes and directly extracts and quantifies the key structural information contained in X-ray projection data. It has been demonstrated that limited number of projections contains enough structural information of the microstructure. And an accurate stochastic procedure of reconstructing heterogeneous microstructures utilizing limited X-ray tomographic projections has been presented and tested on different types of materials in the previous of this chapter. This allows us to save huge amount of space that was used to store thousands of projection data in order to reconstructing the microstructure.

Here we focus on two types of imaging data: (i) X-ray tomographic radiographs (projections) and (ii) 2D micrographs including SEM/BES/SEM/optical images as well as EBSD color maps. As described in detail below, we devise a unified framework to compute correlation functions directly from such raw imaging data, which allows us to “transform” the structural information contained in such data from a non-usable form to a directly usable and understandable form.

Given a 2D micrograph (e.g., EBS/SEM/ optical images or EBSD), a variety of correlation functions (including the n -point correlation function S_n , surface correlation function F_s , lineal-path function L , pore-size function F and cluster function C_2 etc) can be immediately obtained by grouping the pixels belonging to different bulk phases/surfaces/ clusters and computing the pair distances between the pixels in selected groups. Figure 4.13 shows two examples of computing correlation functions from 2D micrographs. In the left panel, S_2 , F_s and C_2 computed from an optical image of a concrete microstructure are shown, which respectively reflect the correlation between

bulk phase, the correlation between the interface, as well as degree of clustering in the microstructure. However, we note that the cluster function C_2 should be used with caution, since certain percolating 3D microstructure may appear disconnected in 2D. In the right panel, the set of S_2 of a polycrystalline microstructure are computed from an EBSD color map, in which each grain (associated with different color) is treated as a distinct “phase”. Both the autocorrelation functions (for individual grains) and the cross-correlation functions (for correlation between different grains) are shown. The correlation functions directly computed from limited 2D micrographs will be employed for stochastic data fusion described in subsequent sections. Again, the accuracy of correlation functions directly computed from the 2D micrographs, which reflects the level of structural information contained in such data, will be ascertained by comparing quantitatively them with the corresponding functions computed from the actual reconstructed 3D microstructure.

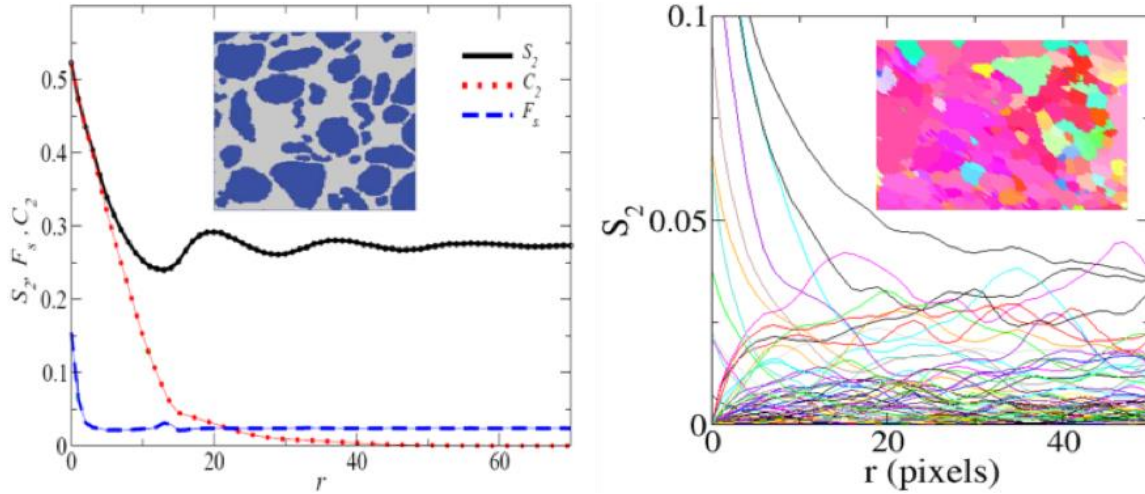


Figure 4.13 Left panel: The correlation functions S_2 , C_2 and F_s of a concrete microstructure (see inset) as computed from a 2D optical image. Right panel: S_2 associated with the grains in a polycrystalline Sn-rich solder joint as computed from a 2D EBSD color map (see inset).

Here we propose to generalize the stochastic reconstruction procedure for integrating limited complementary X-ray tomography and optical imaging data for modeling different types of materials. The reconstruction procedure, which stochastically evolves a trial microstructure to best match the given structural information, provides a convenient means to utilize different types of structural data. Specifically, the objective function is now defined as the linear combination of two “energy” terms, one for tomography data and one for optical images. We note that more terms can be introduced if additional imaging data needs to be incorporated. For the X-ray tomography data, the associated “energy” is defined as the sum of the squared difference between the simulated attenuated intensity value in each projection bin for the trial microstructure and the corresponding experimental value. For the optical imaging data, the associated “energy”

is defined as the sum of squared difference between corresponding correlation functions computed from the optical images and the trial microstructure.

The stochastic reconstruction algorithm with multi-modal data source is first tested on 4 Fontainebleau structures. They all have the same system size with 128 by 128 by 128 total voxels, with different volume fractions of target phase ranging from 5 to 20 percent. Target projections are generated modeling the X-ray tomography experiment with parallel beam geometry. All the projections are evenly distributed from 0 to 180 degrees. The target correlation function (S_2) is directly computed from the target configuration following the procedure described in Chapter 2. The reconstruction process with simulated annealing algorithm is exactly the same as described in detail in the previous of this chapter, except that now the energy that needed to be reduced is the combination of the energy computed from both X-ray tomography projections and two-point correlation functions. Eventually the energy will converge to a local minimum, which is practically more likely to happen in the most of the case, and the reconstruction will be considered succeeded if the total energy is below a certain tolerance.

Sample 1 to 3 are reconstructed with S_2 and 4 projections due to relative small volume fractions and simple structures. And Sample 4 is reconstructed using 6 projections for relatively high volume fraction. The volume fractions of different structures can be found in Table.1. Figure 4.14 shows an example of the reconstruction result for sample one as an example, using multi-modal data, compared with the reconstruction results using single source. Here the two-point correlation function S_2 used for reconstruction is computed directly from the target structure. Although Figure 2(A) and (B) share the same correlation function, the reconstruction result is far away from the

target structure. This is due to the nature of degeneracy of lower order correlation functions [51, 52]. Figure 2(C) is the reconstruction result from 4 projections. As we can see the main frame of the structure has been constructed. However, the details are not perfectly captured as a lot of random points exist in the reconstruction result. This is due to the reason that not enough structural information is provided in 4 projections for such a system. As we compare the result in Figure 2(D) with the target structure, one can tell that the key structure features have been perfectly captured and illustrated. Our understanding of this excellent reconstruction result is that during the beginning of the reconstruction, two-point correlation function can make the initially totally random distributed target voxels quickly converge to large structure features. And as the reconstruction procedure continues, projections can provide extra structural constrains and refine the shape, especially edges of those particles and clusters. We then quantify the accuracy of the reconstruction with a metric, which represents the normalized difference between the target structure and all three reconstruction results, i.e., total number of target voxels that are misdisplaced from the correct position divided by the system size. All the values are listed in Table 4.1. These values, together with the 3D illustration, qualitatively and quantitatively demonstrate that the combined information input can significantly improve the reconstruction accuracy compared with single source input.

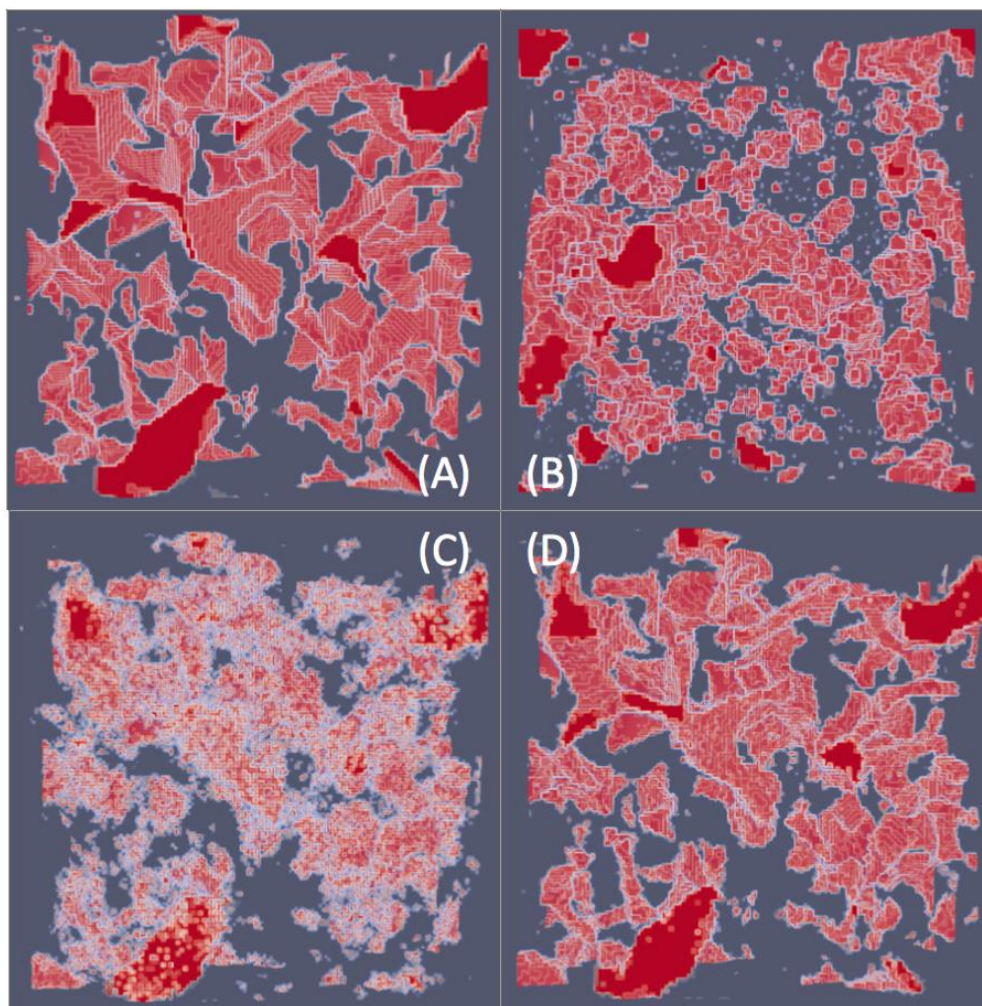


Figure 4.14 Target structure of a Fountainbleau sample (A) and the reconstruction result using only S_2 (B), only 4 projections (C), and both S_2 and 4 projections (D).

Table 4.1 Volume fraction of the target phase and normalized error between target structure and reconstruction results with different data input.

	Volume fraction	S2 only	projections only	S2 + projections
Sample_1	0.0584	0.1132	0.0358	0.0103
Sample_2	0.0964	0.1728	0.0583	0.0207
Sample_3	0.1600	0.2681	0.1071	0.0408
Sample_4	0.2141	0.3383	0.1073	0.0274
SiC/Al composite	0.1390	0.2274	0.0678	0.0184

Figure 4.15 shows the reconstruction of a coarsening Pb-Sn system isothermally aged at 175°C at different time points. Each 3D microstructure is reconstructed from only 5 synchrotron projections evenly distributed over 0° and 180° and the two-point correlation function S_2 computed from a single optical image of the polished surface of the material. The stochastic reconstructions are found to be in excellent agreement with the corresponding reconstructions via FBP using the full tomography data set (including 1048 projections), with the fraction of misdisplaced voxels less than 5% for all cases.

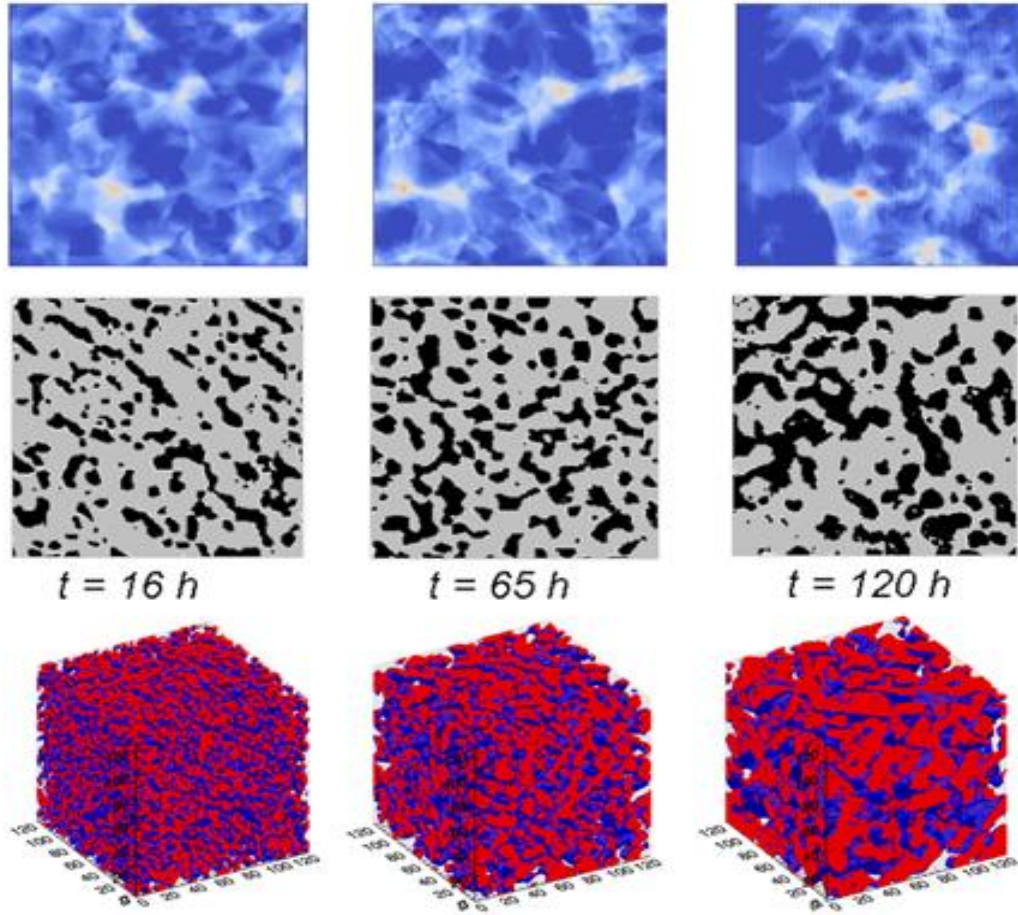


Figure 4.15 Upper panels: Parallel-beam X-ray tomography projection intensity maps for the Pb-Sn system at different aging stages. Middle panels: Optical images of the coarsening system at different stages corresponding to the tomography data. Lower panels: 3D reconstruction of the coarsening system via stochastic optimization using both tomography data and optical images. Linear size of the system shown in the panels is 180 μm .

We then further investigate the minimal set of complementary imaging data (e.g., X-ray tomography projections and correlation functions computed from optical images) for modeling more complex material systems. The model is a SiC/Al composite with

irregular shaped SiC particles and Al alloy with anisotropic secondary phase inclusions [7, 8, 62-64, 73]. The X-ray tomography projections are provided by Dr. Nikhilesh Chawla's group from Arizona State University. The discretized system size of SiC/Al composite material is 360 by 360 by 2028 voxels, which is approximately 2 mm in height and 400 by 400 μm^2 in cross sectional area. For better illustration, here will only show a small portion of the structure. As the results showing in Figure 4.16, multi-modal reconstruction with 4 projections and S_2 can provide us very accurate 3D rendition of the structure as all the SiC particles are perfectly reconstructed. The accuracy can further improved by increasing projection number to 5. In comparison, reconstructions with only 5 projections and only S_2 are also provided. The quantified accuracy of with different reconstruction inputs are also listed in Table 4.1. These results suggest that a minimal set of complementary imaging data can contain sufficient structural information for material characterization and such information can be efficiently utilized via our stochastic reconstruction procedure.

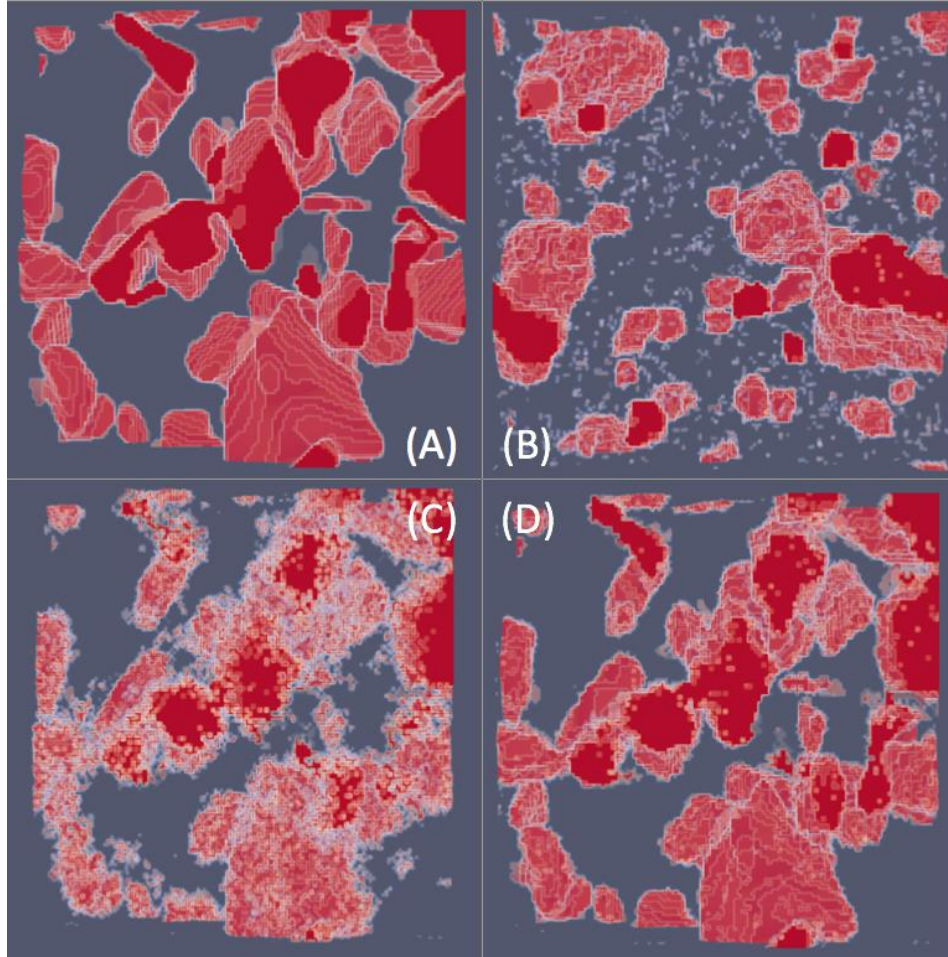


Figure 4.16 Target structure of SiC/Al composite (A) and the reconstruction result using only S_2 (B), only 5 projections (C), and both S_2 and 5 projections (D).

4.5 Summary

In this chapter, we have presented in detail a stochastic procedure to accurately reconstruct two-phase heterogeneous materials from limited-angle tomographic projection data. We have demonstrated the utility of this procedure by applying it to successfully reconstruct a number of topologically complex 3D microstructures from both simulated noise-free projection data as well as experimentally obtained

polychromatic cone-beam data and parallel-beam synchrotron data. The information content of the projection data is also investigated. Our reconstruction results imply that the large tomographic data set (typically having several hundred projections) used by tradition reconstruction methods would contain significantly redundant structural information for capturing the salient features of the microstructure. Thus, the stochastic procedure could provide a means to use the information in tomographic data in a highly efficient manner. We note that our reconstruction procedure based on limited x-ray tomography data is different from widely used material microstructure reconstruction techniques based on statistical descriptors [74-87], image synthesis [88,89] or machine learning [90-92].

The stochastic reconstruction with multi-modal data fusion takes the advantage of both the structural information from statistical descriptors (i.e., two-point correlation function), and morphological information (i.e., X-ray tomographic projections), which combined provides us a novel optimization procedure that requires much less data input, a fast reconstruction running time, and an accurate result. The two-point correlation functions can be directly computed from 2D micrographs like EBS/SEM/ optical images or EBSD. The projection number required here is further reduced compared to the stochastic reconstruction procedure that utilize projections alone, not to mention the significant reduction compared to the traditional reconstruction algorithm, like FBP, which requires thousands of projections.

In the current work, the angles associated with the projections were evenly distributed. It is not obvious that such a distribution of angles can lead to a set of projections that contain the maximum level of structural information. It is highly desirable to investigate what is the optimal distribution of the angles for a given material system that can lead to a set of projections that contain the highest level of structural information for a given number of projections.

CHAPTER 5

MICROSTRUCTURAL DEGENERACY AND ENERGY LANDSCAPE ASSOCIATED WITH X-RAY TOMOGRAPHIC PROJECTION

In the previous chapter we have found out that accurate reconstruction can be achieved with limited X-ray projection data. In this chapter, we will focus on degeneracy of microstructure and energy landscape respect to different number of projections, to analytically explain the accuracy of our reconstruction algorithm, following Gommes's previous work [51, 52], where he addressed the same issue using two-point correlation functions. The degeneracy of two-phase microstructures with different number of projections can be analyzed by mapping them to ground state degeneracy. And the associated density of states can be determined through Monte Carlo simulation. Hamming distance will be used here to determine the roughness of energy landscape for different systems associated with different number of projections. And this will explain the relative easiness of reconstruction for different microstructures. At last, cooperating with Gommes [93], analytical expressions of different energy states will be expressed. A metric will also be defined to characterize the roughness of the energy landscape.

5.1 Microstructural Degeneracy and Density of States

The degeneracy of a microstructure is defined as the number of configurations that have energy $E = 0$. And the energy here is respected to projections and the definition can be found in previous chapter. In the case of two-point correlation functions, structures that can be obtained through space transformations that preserve distances, i.e., translation, rigid rotations, and inversion, will share the same two-point statistics and therefore can all be considered as the ground state degeneracy [51, 52]. The number of

ground state degeneracy is subjected to system size and the complexity of the structure. The situation in the case of projections is different in several ways. By the definition of energy and the nature of projections, trivial transformations will not work here, and the ground-state degeneracy is subjected to the number of projections. Now the ground-state degeneracy includes the structures that share the same set of projections. And increasing the number of projections will reduce the ground-state degeneracy because by involving more constrains, the number of configurations that meet those constrains will decrease. And eventually, after reaching a critical number of projections, the ground-state degeneracy will be reduced to 1, and a target structure will be uniquely defined by those projections.

An ergodic exploration of all the possible configurations of a microstructure with certain volume fractions of different phases is barely doable even for a small system. In order to estimate the degeneracy of microstructure, a Monte Carlo simulation will be utilized. The method of using MC simulation to numerically estimate density of states was first developed by Wang and Landau [94, 95]. In their work, the density of states (DOS) $\Omega(E)$ is defined as the number of configurations with a certain energy E . And the ground-state energy is then taken by $\Omega(E)$ with $E = 0$.

Wang and Landau's method is different with canonical Monte Carlo simulations. In their method, the transition probability is in the form of

$$p(E_1 \rightarrow E_2) = \min \left[1, \frac{g(E_1)}{g(E_2)} \right] \quad (5.1)$$

where $g(E)$ is the density of states of energy E . As they claimed that using this formulation, all the energies can be visited equally. However, the density of states $\Omega(E)$ is

unknown so the method will go through an iterative way.

Starts from here all the tests will be done on binary systems for better illustration purpose. And it should be aware that these methods can be easily applied to multiphase systems. For a 2D binary system, we can generate a set of projections by modeling the X-ray tomography experiment, as details described in the previous chapter. For any other configurations with the same volume fraction of each phase, we can acquire their projections following the same way. And then we can define the energy as the squared difference between each detector bin in every projections of the target structure and that of the temporary structure,

$$E = \sum_i^\alpha \sum_j^N (\hat{p}(i, j) - p(i, j))^2 \quad (5.2)$$

where \hat{p} represents the target projections, p the projections of the temporary structure, α is the total number of projections, and N is the total detector bin in each projection. The goal here is to figure out the total number of configurations that has the energy E , i.e., $\Omega(E)$. Starting with $\Omega(E) = 1$ for all possible energies, the system will evolve following a Monte Carlo simulation. In each trial move, two pixels (voxels in 3D) in different phases will be randomly selected and their position will be switched. This will result in a new configuration and a new energy. Whether this new configuration is accepted or not is determined by the acceptance probability defined in Eq. (5.1). If it is accepted, the density of states of the corresponding energy will be updated as $\Omega(E) \rightarrow \Omega(E) \times f$, where f is a modification factor larger than 1. Wang and Landau stated that by selecting f equals to $e = 2.71828\dots$, it will allow us to reach all possible energy levels very quickly [95]. The evolution is terminated after certain number of runs. And then the modification factor is updated as $f \rightarrow \sqrt{f}$. And the evolution starts again. Eventually, f will reduce to a

value very close to 1. And the procedure will stop when f reaches below a prescribed value. In our study the critical value of f is 1.00001. It is clear that the modification factor acts as a control parameter in the MC simulation, like the cooling temperature T in the stochastic reconstruction algorithm.

After the MC simulation, the cumulative DOS is computed as

$$N_{\Omega}(E) = \sum_{e \leq E} \Omega(e) \quad (5.3)$$

And it is then normalized by setting $N_{\Omega}(E)$ to be equal to the total number of configurations Ω_{tot} . For a binary structure with total number of pixels equal to N , and the number of black pixels N_l , the total number of configurations is equal to the number of different ways selecting N_l positions for the black pixels in total N locations, i.e.,

$$\Omega_{tot} = \binom{N}{N_l} \quad (5.4)$$

The running moves for every modification factor f is chosen so that after normalization, the density of state for $E = 1$ for one projection is equal to the theoretical value $\Omega(1)$.

What differs the situation for projections from correlation functions is that in order to determine the DOS for all possible energies, the number of projections play an important role. Increasing projection number will result in increasing possible energy states, since the energy is calculated through all the projections provided. So in the current study, the normalized DOS is computed and plotted with respect to different projection numbers. We first test the algorithm on three structures with same system size of 8 by 8, and the number of black pixels, which is 13. The three structures are namely a single disk, hard disks, and a Poisson point process. The ground state configuration and the plots of normalized cumulative DOS versus energy are shown in Figure 5.1. The

ground-state degeneracy of each configuration associated with one projection and theoretically the number of all possible configurations associated with the system size and numbers of target pixels are listed in table 5.1.

Table 5.1 System size, number of target pixels, ground-state degeneracy associated with one projection, and theoretically the number of all possible configurations

	System size	Target pixel	Ground-state Degeneracy	All possible configurations
Single disk	8 x 8	13	1.1239×10^7	1.31369×10^{13}
Hard disks	8 x 8	13	5.5073×10^8	1.31369×10^{13}
Poisson distribution	8 x 8	13	8.8117×10^9	1.31369×10^{13}
Large spheres	32 x 32	196	3.5021×10^{177}	4.33082×10^{215}

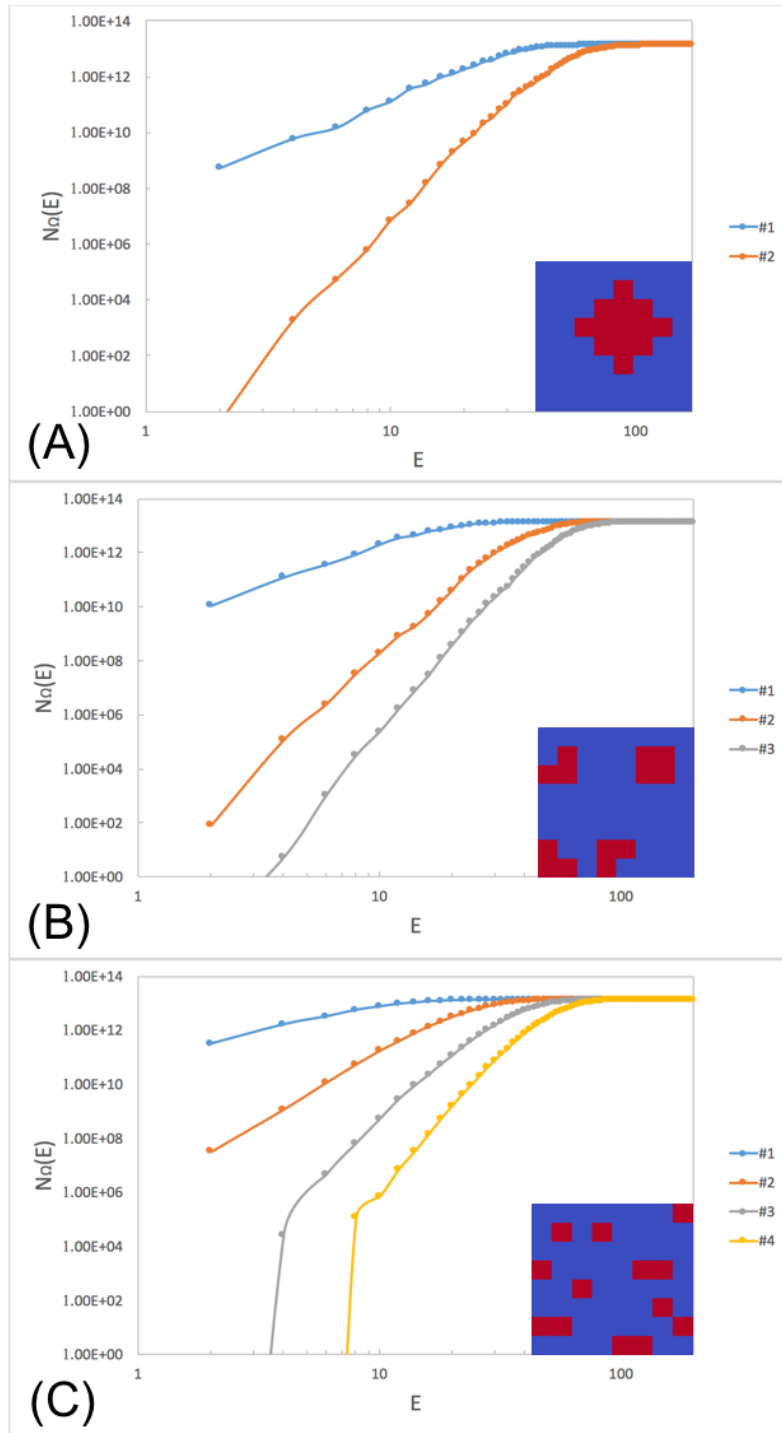


Figure 5.1 Cumulative DOS associated with energy for (A) single disk, (B) small hard disks, and (C) Poisson point process. The system size is 8 by 8, and the number of red pixels is 13 for all three configurations.

As the plot shows, the trend for different number of projections is the same as the cumulated DOS is increasing from a certain value when E is small, to the theoretical value of possible configurations by increasing E . When increasing the projection number, the DOS for certain energy is decreasing. This is because increase projection number will increase structural constrains to the system. At the same time the possible energy state is increasing by increasing number of projections. As a result, the possible configurations to match certain energy will decrease. As one notices that for large number of projections, the cumulative DOS will drop below the horizontal axis when the energy is reducing to a value. This is because the number of configurations with energy smaller than that certain value are really small and hard to reach in a random evolution algorithm like Monte Carlo simulation. So the normalized DOS can be considered as under sampling for those energies. For small systems like the configurations shown in Figure 5.1, the minimum number of projections that required to reconstruct a configuration exactly the same as the target structure is achievable. This is verified by plotting out the configurations of $E = 0$ under different number of projections and examine with the target configuration. For single disk, the minimum number of projections required to reconstruct the target structure is 2. The number for hard disks is 3, and 4 for Poisson point process.

We then apply the algorithm to larger systems. The target structure now has system size of 32 by 32, consist of 16 hard disks with total 196 total black pixels. The results of cumulative DOS versus energy for different number of projections are shown in Figure 5.2. The result shows the same trend that for certain energy, the cumulative DOS is decreasing by increasing number of projections. The huge drop of DOS when energy reach a certain value can be considered as reaching to those steep energy wells on the

energy landscape. These results validate the situation that in practice reconstructing a perfect match of target structure is impossible to reach even for a very small system. Instead, what we can do is to set an energy threshold, and claim that the reconstruction is succeeded when the energy is dropped below that threshold. As one can see the accuracy of the reconstruction is increasing by using more projections. By reducing the possible configurations that can be reached, we are increasing the probability of getting the target structure, or structures close enough to the target that the error of overall performance can be ignored.

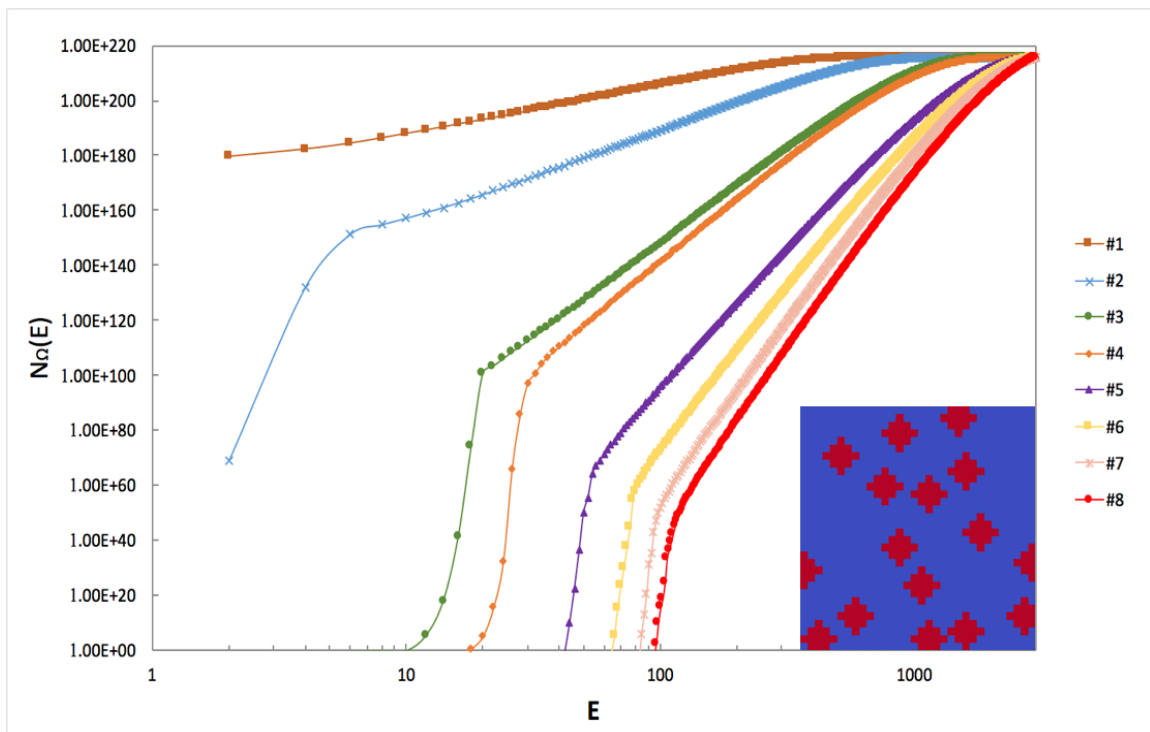


Figure 5.2 Cumulative DOS associated with energy for configuration with multiple spheres. The system size is 32 by 32 and the number of red pixels is 196.

5.2 Energy Landscape and Roughness Metric

To characterize the energy landscape, a complete configuration space of a two-

phase microstructure should be defined first. For a microstructure with N pixels, all the possible configurations will be the vertices of an N -dimensional hypercube [51]. The vertices of the hypercube are consist of sets of indicator vectors $I(i)$, where the value could only be either 1 or zero, indicating black and white. Moving from one vertex to another along a prescribed direction means replacing the value of one pixel to another. For reconstruction problems, not all the vertices are needed to be explored since the numbers of black and white pixels are kept constant at all times. All the realizable configurations will be lying on the intersection of the hypercube with a lower-dimensional hyperplane. And each vertex has an energy assigned by Eq. (5.2). Now an energy landscape can be defined as a set of energies associated with each vertex on the hyperplane. And what a reconstruction algorithm does is to thoroughly explore the energy landscape in order to find the vertices with $E = 0$. Because systems with large ground-state degeneracies intend to have a rough energy landscape [96, 97], so the hypothesis here is that by reducing the ground-state degeneracy with increasing number of projections, we should be able to achieve a smoother energy landscape, which as a result, a more accurate reconstruction. We can also determine the relative reconstruction complexity of different microstructures by comparing the roughness their energy landscape.

In order to explore the vertices on the hyperplane, here we will involve a concept from information theory. By definition, a hamming distance is the number of positions of two strings with the same length where the symbols are different [98]. In reconstruction, we can consider the hamming distance as the number of misdisplacements of black pixels of a configuration compared to the target one. By reducing the hamming distance, we are

moving black pixels to the correct spot, and eventually, when all the black pixels are on the right places, the reconstruction is finished.

Now the energy landscape can be explored with a random walk on the configuration space by changing the hamming distance. The procedure is as follows. Starting from the target configuration, the system will be moving to any configurations with hamming distance equal to 1, by randomly switching one black pixel with a white pixel. Compute the energy E for this new configuration. And then move to a configuration with hamming distance equal to 2, and compute the energy. By increasing the number of random moves, configurations with large hamming distance from the ground state will be explored. This process is repeated with different number of projections, and the results are plotted in Figure 5.3, 5.4 for different structures. The energy E for each hamming distance d is an average value of 10000 random walk cases in order to explore all possible configurations. As the result shows, for certain hamming distance, increasing number of projections will increase the energy. This means that more projections provide more constrains to the structure, and moving black pixels around in the configuration will have larger impact on the overall energy. On the other hand, in order to achieve certain energy, the hamming distance with more projections will be smaller than that of fewer projections. This explains the higher accuracy of reconstruction with more projections because the reconstruction result is more close to the ground state, whereas for reconstructions with smaller number of projections, the configuration could still be random but achieve the threshold energy at the same time.

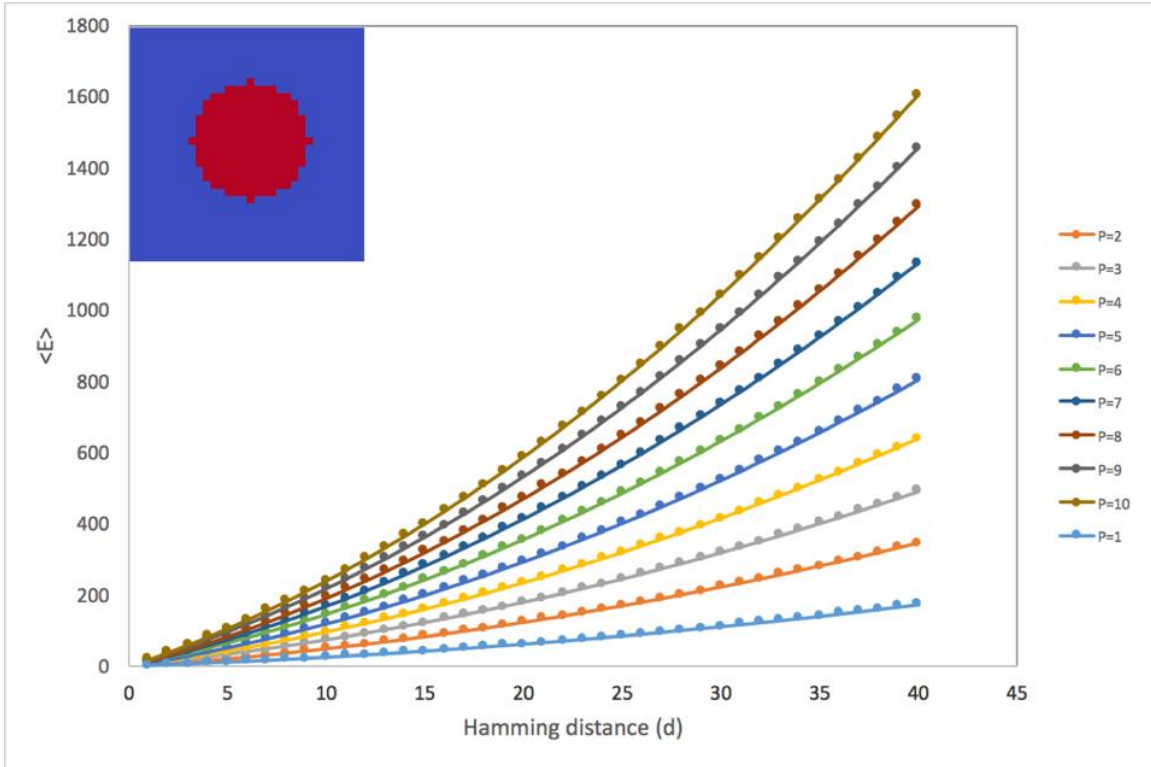


Figure 5.3 Average energy associated with hamming distance for single sphere structure under the condition of different number of projections. The system size is 32 by 32 and the number of red pixel is 196.

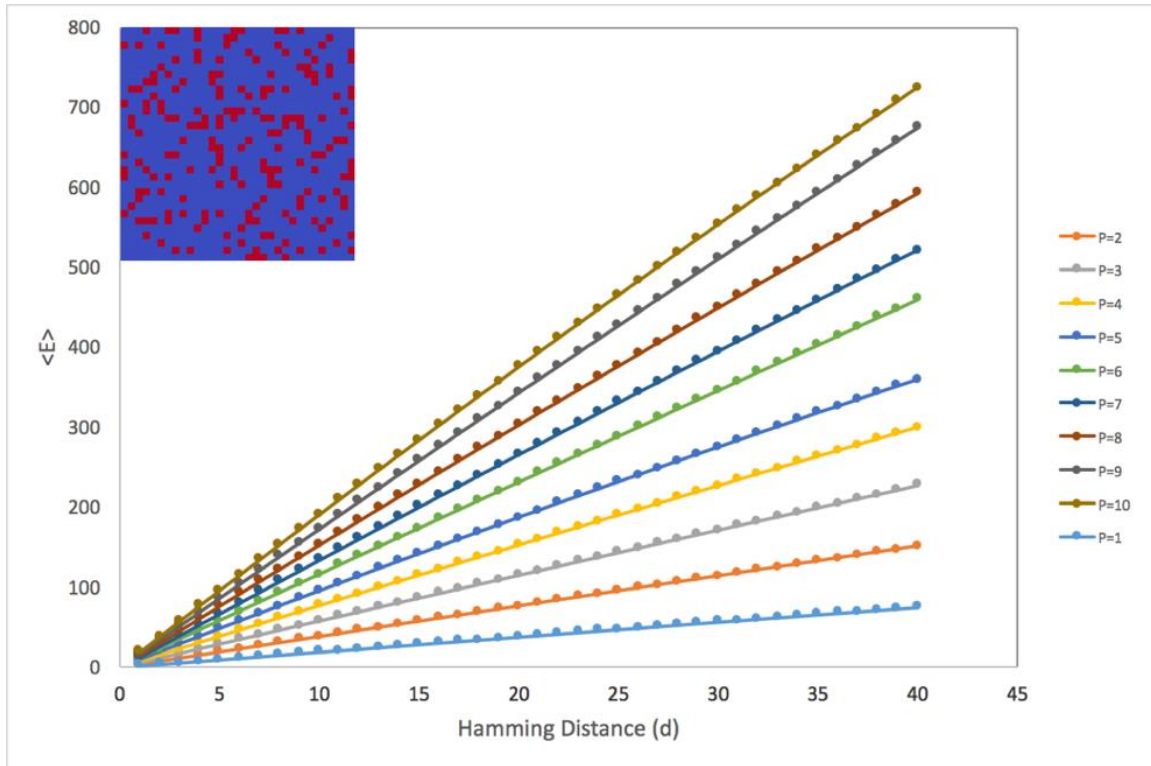


Figure 5.4 Average energy associated with hamming distance for a structure of Poisson point process under the condition of different number of projections. The system size is 32 by 32 and the number of red pixel is 196.

Comparing the energy of the same hamming distance for different structures can give us an insight of the relative reconstruction complexity of the structure. Shown in Figure 5.5 are three structures with the same system size 32 by 32 and same number of black pixels 196 with 5 projections. The three structures are single sphere, multiple spheres with smaller radius, and Poisson point process. The energy of single sphere by increasing hamming distance shows a higher increasing rate than that of smaller multiple spheres and Poisson point process. This means that moving one black pixel can have a larger impact on the overall energy for reconstructing a relative simple structure. On the

contrary, the energy change by reducing the hamming distance for Poisson point process is small. This is reasonable since the random distribution of black pixels increases the complexity of reconstruction. So if we set the threshold energy of reconstruction to be the same for all three cases, one could expect a better reconstruction result from the single sphere case. Another observation from Figure 5.5 is that the average curve has a quadratic relationship with hamming distance d , whereas for Poisson point distribution, the relationship is linear. This has been explained qualitatively by Gommès as the difference in interpretation of holes and extra pixels with hamming distance d [52]. For single sphere, the quadratic behavior shows a collective contribution of target pixels to the overall energy. On the contrary, the target pixels in Poisson distribution are relatively independent to each other, and this results in a linear contribution to the total energy. And the relation of average energy with hamming distance for multiple small spheres is somewhere in between quadratic and linear.

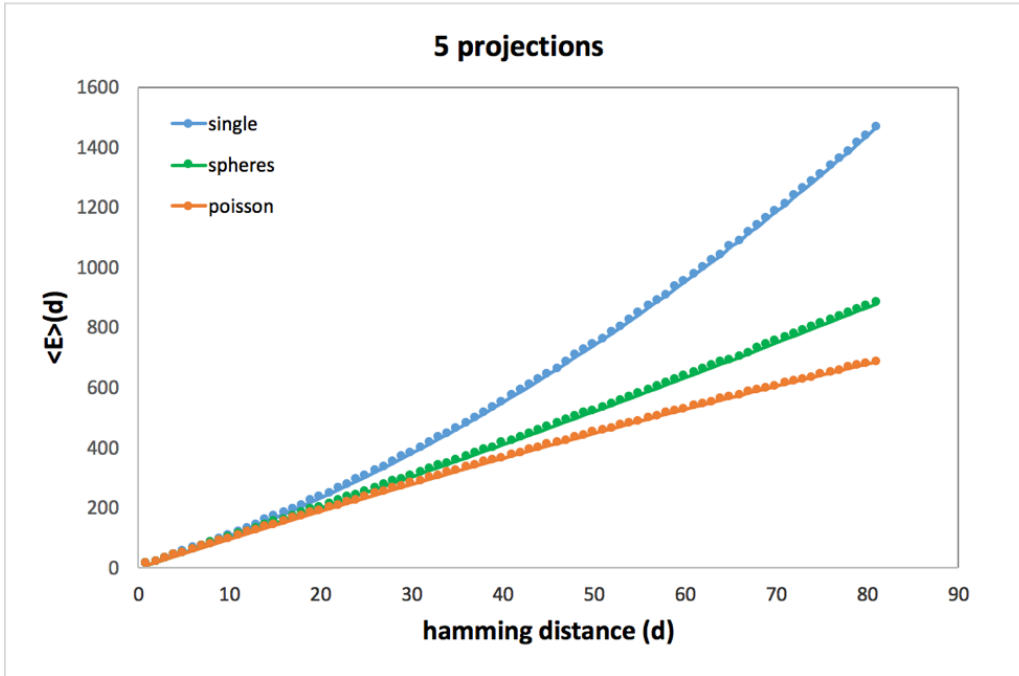
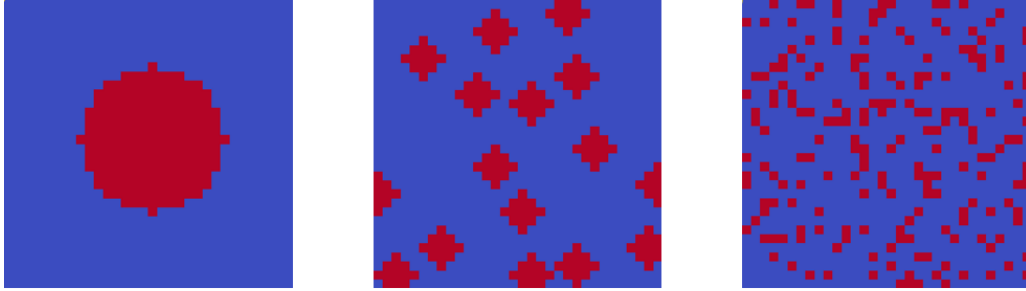


Figure 5.5 Comparison of average energy $\langle E \rangle$ associated hamming distance for three different structures with same system size, and number of red pixels under the condition of 5 projections.

In the rest of this chapter we will analytically explore the average energy for n random moves $\langle E \rangle(n)$ closely follow the work from Gommès [51, 52, 93]. We will start with the notations and definition of the energy. The projection along direction α can be written as follows

$$f_{\alpha}(n) = \sum_i P_{\alpha}(n, i) I(i) \quad (5.5)$$

where I is the indicator function of the structure and $P_\alpha(n, i)$ is an operator matrix of the projections. If we define the set of target projections as $\hat{f}_\alpha(n)$, then for any configuration with projections $f_\alpha(n)$, the energy can be defined as

$$\begin{aligned} E &= \sum_\alpha \sum_n \left(\hat{f}_\alpha(n) - f_\alpha(n) \right)^2 \\ &= \sum_\alpha \sum_n \left(\hat{f}_\alpha(n) - P_\alpha(n, i) I(i) \right)^2 \end{aligned} \quad (5.6)$$

The problem is simpler here than for correlation functions because the energy is quadratic in I instead of fourth power in the case of correlation function [52]. The energy can be written as

$$\begin{aligned} E &= \sum_\alpha \sum_n \left(\hat{f}_\alpha(n) \right)^2 \\ &\quad - 2 \sum_i \left[\sum_\alpha \sum_n \hat{f}_\alpha(n) P_\alpha(n, i) \right] I(i) \\ &\quad + \sum_i \sum_j \left[\sum_\alpha \sum_n P_\alpha(n, i) P_\alpha(n, j) \right] I(i) I(j) \end{aligned} \quad (5.7)$$

where the following quantities appear. A vector of size N

$$\hat{I}_b(i) = \sum_\alpha \sum_n \hat{f}_\alpha(n) P_\alpha(n, i) \quad (5.8)$$

which can be considered as a back-projection operation of $\hat{f}_\alpha(n)$. And a symmetric $N \times N$ matrix

$$J_{ij} = \sum_\alpha \sum_n P_\alpha(n, i) P_\alpha(n, j) \quad (5.9)$$

Using a strict definition of projection, $P_\alpha(n, i)$ is equal to zero everywhere except the value of n that corresponds to the receiving detector bin of the X-ray with direction α that pass through point i . For that value of n , $P_\alpha(n, i) = 1$. With that, the production $P_\alpha(n, i) P_\alpha(n, j)$ in Eq. (5.9) will be equal to 1 if the X-ray that being received by detector bin n passes both point i and j . And it will be equal to zero anywhere else.

The Eq. (5.7) is equivalent to an Ising Hamiltonian with interaction matrix J_{ij} and space-dependent external field $\hat{I}_b(i)$,

$$E = \sum_{\alpha} \sum_n \hat{f}_{\alpha}(n)^2 - 2 \sum_i \hat{I}_b(i)I(i) + \sum_i \sum_j J_{ij}I(i)I(j) \quad (5.10)$$

It is interesting to notice from the equation that the energy can be minimized by a scalar product if $I = \hat{I}_b$. However, in this way the inverse projection operation will tend to create configurations with many pixels aligned with the projection directions. Based on the definition of J_{ij} , this operation, however, will result in maximizing the value of $\sum_i \sum_j J_{ij}I(i)I(j)$. With the conflicting constraints existing at the same time, the best solution should be considered as a compromise.

Now we will see how random moves starting from target configuration can affect the energy. We will consider the effect separately on each of the three contributors to the energy in Eq. (5.10), namely,

$$\hat{E}_0 = \sum_{\alpha} \sum_n \hat{f}_{\alpha}(n)^2 \quad (5.11)$$

$$\hat{E}_1 = \sum_i \hat{I}_b(i)I(i) \quad (5.12)$$

and

$$E_2 = \sum_i \sum_j J_{ij}I(i)I(j) \quad (5.13)$$

The symbol $\hat{}$ in these notations highlights the quantity that depends on the target projection data, i.e., $\hat{f}_{\alpha}(n)$.

Linear contributions \hat{E}_1

When randomly moving a pixel (voxel in 3D) from position p to position q , the modification of the indicator function can be written as

$$I'(i) = I(i) + \delta(i, q) - \delta(i, p) \quad (5.14)$$

So the first-order contribution to the energy becomes

$$\hat{E}'_1 = \hat{E}_1 + \hat{I}_b(q) - \hat{I}_b(p) \quad (5.15)$$

When pixels p and q are chosen randomly in the black and white phases, respectively, the average value of \hat{E}'_1 is computed as,

$$\langle \hat{E}'_1 \rangle = \frac{1}{N_0 N_1} \sum_p \sum_q I(p)(1 - I(q)) [\hat{E}_1 + \hat{I}_b(q) - \hat{I}_b(p)] \quad (5.16)$$

where $N_1 = \sum_i I(i)$ and $N_0 = N - N_1$. This leads to

$$\langle \hat{E}'_1 \rangle = \hat{\beta}_0 + \beta_1 \hat{E}_1 \quad (5.17)$$

with

$$\hat{\beta}_0 = \frac{1}{N_0} \sum_q \hat{I}_b(q) \quad (5.18)$$

and

$$\beta_1 = 1 - \frac{N}{N_0 N_1} \quad (5.19)$$

Eq. (5.17) can be used recursively to estimate the average value of \hat{E}'_1 after n random moves, and we can find

$$\langle \hat{E}'_1 \rangle(n) = \frac{\hat{\beta}_0}{1 - \beta_1} + \beta_1^n (\hat{E}_1(0) - \frac{\hat{\beta}_0}{1 - \beta_1}) \quad (5.20)$$

where $\hat{E}_1(0)$ is the starting value of \hat{E}_1 , which is the value in the ground-state. For special case like $n = 1$,

$$\langle \hat{E}'_1 \rangle(1) = \frac{1}{N_0} \sum_i \hat{I}_b(i) + (1 - \frac{N}{N_0 N_1}) \hat{E}_1(0) \quad (5.21)$$

And in the limit of $n \rightarrow \infty$, this will be

$$\lim_{n \rightarrow \infty} \langle \hat{E}'_1 \rangle(n) = \frac{\hat{\beta}_0}{1 - \beta_1} = \frac{N_1}{N} \sum_i \hat{I}_b(i) \quad (5.22)$$

Since $\frac{N_1}{N}$ is the probability for $I(i)$ takes the value 1 when the system is totally scrambled.

Quadratic contribution E_2

Here we apply the procedure as in the case of \hat{E}_1 , changing E_2 to E'_2 by moving pixel p to position q , as

$$E'_2 = E_2 + J_{pp} + J_{qq} - 2J_{pq} + 2 \sum_j J_{qj} I(j) - 2 \sum_j J_{pj} I(j) \quad (5.23)$$

For the situation when p is randomly chosen from black phase, and q is from white phase, the average value of E'_2 will be

$$\langle E'_2 \rangle = \beta_2 + \beta_3 E_2 + \beta_4 \sum_i J_{ii} I(i) + \beta_5 \sum_{ki} J_{ki} I(i) \quad (5.24)$$

With

$$\beta_2 = \frac{1}{N_0} \sum_k J_{kk} \quad (5.25)$$

$$\beta_3 = 1 + \frac{2}{N_0 N_1} - \frac{2}{N_0} - \frac{2}{N_1} \quad (5.26)$$

$$\beta_4 = \frac{1}{N_1} - \frac{1}{N_0} \quad (5.27)$$

$$\beta_5 = \frac{2}{N_0} - \frac{2}{N_0 N_1} \quad (5.28)$$

The structures of the last two terms in Eq. (5.24) are scalar product of vector I with a constant vector, which are mathematically identical to Eq. (5.12). The average value of the two terms after n random moves can then be computed through Eq. (5.20) with appropriate β_0 . And the result is

$$\langle \sum_i J_{ii} I(i) \rangle(n) = \frac{\beta'_0}{1-\beta_1} + \beta_1^n (\langle \sum_i J_{ii} I(i) \rangle(0) - \frac{\beta'_0}{1-\beta_1}) \quad (5.29)$$

with

$$\beta'_0 = \frac{1}{N_0} \sum_i J_{ii} = \beta_2 \quad (5.30)$$

and

$$\langle \sum_{ki} J_{ki} I(i) \rangle(n) = \frac{\beta_0''}{1-\beta_1} + \beta_1^n (\langle \sum_{ki} J_{ki} I(i) \rangle(0) - \frac{\beta_0''}{1-\beta_1}) \quad (5.31)$$

with

$$\beta_0'' = \frac{1}{N_0} \sum_i \sum_k J_{ki} \quad (5.32)$$

Therefore, the final result of $\langle E_2 \rangle(n)$ is

$$\begin{aligned} \langle E_2 \rangle(n) &= \beta_2 \frac{1-\beta_3^n}{1-\beta_3} + \beta_3^n \langle E_2 \rangle(0) \\ &+ \beta_4 \left[\frac{\beta_0'}{1-\beta_1} \frac{1-\beta_3^n}{1-\beta_3} + \left(\langle \sum_i J_{ii} I(i) \rangle(0) - \frac{\beta_0'}{1-\beta_1} \right) \frac{\beta_3^n - \beta_1^n}{\beta_3 - \beta_1} \right] \\ &+ \beta_5 \left[\frac{\beta_0''}{1-\beta_1} \frac{1-\beta_3^n}{1-\beta_3} + \left(\langle \sum_{ki} J_{ki} I(i) \rangle(0) - \frac{\beta_0''}{1-\beta_1} \right) \frac{\beta_3^n - \beta_1^n}{\beta_3 - \beta_1} \right] \end{aligned} \quad (5.33)$$

In the limit of $n \rightarrow \infty$, this will converge to

$$\lim_{n \rightarrow \infty} \langle E_2 \rangle(n) = \frac{N_0 N_1}{N(N-1)} \sum_i J_{ii} + \frac{N_1(N_1-1)}{N(N-1)} \sum_{ik} J_{ik} \quad (5.34)$$

For large systems with $n \rightarrow \infty$, one can expect the pixels are independent from one another, and this leads to

$$\langle I(i) I(j) \rangle \cong \left(\frac{N_1}{N} \right)^2 + \delta_{ij} \left(\frac{N_1}{N} - \left(\frac{N_1}{N} \right)^2 \right) \quad (5.35)$$

With that, the expression of E_2 can then be written as

$$\langle E_2 \rangle = \left(\frac{N_1}{N} \right)^2 \sum_{ij} J_{ij} + \frac{N_0 N_1}{N^2} \sum_i J_{ii} \quad (5.36)$$

Roughness Metric

As defined in Gommel's previous work [52], a roughness metric can be written as

$$\rho = \langle E \rangle(1) / \langle E \rangle(\infty) \quad (5.37)$$

where $\langle E \rangle(1)$ is the average energy of all the configurations with hamming distance equal to 1, and $\langle E \rangle(\infty)$ is the average energy for all possible configurations with the given

system size and number of black pixels.

The quantity of $\langle E \rangle(1)$ can be considered as the energy curvature as it represents the difference between the average energy of a near neighborhood to the energy of the central point. With the previous knowledge, we can put that

$$\begin{aligned}
\langle E \rangle(1) &= \sum_{\alpha} \sum_n f_{\alpha}(n)^2 - 2 \sum_i I_b(i)I(i) + \sum_{ij} J_{ij}I(i)I(j) \\
&\quad - 2 \left[\frac{1}{N_0} \sum_i I_b(i) - \frac{N}{N_0 N_1} \sum_i I_b(i)I(i) \right] \\
&\quad + \frac{1}{N_0} \sum_i J_{ii} + \left(\frac{1}{N_1} - \frac{1}{N_0} \right) \sum_i J_{ii}I(i) + \frac{2}{N_0} \left(1 - \frac{1}{N_1} \right) \sum_{ij} J_{ij}I(i) \\
&\quad - 2 \frac{N}{N_0 N_1} \left(1 - \frac{1}{N} \right) \sum_{ij} J_{ij}I(i)I(j) \tag{5.38}
\end{aligned}$$

The first three terms are the energy of the start point, which is the ground state. In other words, those three terms will vanish. It is also turns out that the energy $\langle E \rangle(1)$ is identical for all ground states. All terms involving $I(i)$ can be expressed in terms of projections $f_{\alpha}(n)$. With the definition of back-projection in Eq. (5.8), we can write

$$\sum_i I_b(i) = \sum_{\alpha} \sum_n V_{\alpha}(n) f_{\alpha}(n) \tag{5.39}$$

where $V_{\alpha}(n)$ is defined as

$$V_{\alpha}(n) = \sum_i P_{\alpha}(n, i) \tag{5.40}$$

Similarly,

$$\sum_i I_b(i)I(i) = \sum_{\alpha} \sum_n f_{\alpha}(n)^2 \tag{5.41}$$

And

$$\sum_{ij} J_{ij}I(j) = \sum_{\alpha} \sum_n P_{\alpha}(n, i) \sum_j P_{\alpha}(n, i)I(j) = \sum_{\alpha} \sum_n V_{\alpha}(n) f_{\alpha}(n) \tag{5.42}$$

We also have

$$\sum_i J_{ii}I(i) = N_1 N_{\alpha} \tag{5.43}$$

where N_{α} is the total number of projections. In the meantime,

$$\sum_{ij} J_{ij} I(i) I(j) = \sum_{\alpha} \sum_n f_{\alpha}(n)^2 \quad (5.44)$$

Eventually, we will achieve an easier expression of $\langle E \rangle(1)$, as

$$\begin{aligned} \langle E \rangle(1) &= 2N_{\alpha} - \frac{2}{N_0 N_1} \sum_{\alpha} \sum_n f_{\alpha}(n) (V_{\alpha}(n) - f_{\alpha}(n)) \\ &= 2 \sum_{\alpha} \left[1 - \frac{1}{N_0 N_1} \sum_n f_{\alpha}(n) (V_{\alpha}(n) - f_{\alpha}(n)) \right] \end{aligned} \quad (5.45)$$

Average energy $\langle E \rangle(\infty)$

The average energy of all possible configurations can be written as

$$\begin{aligned} \langle E \rangle(\infty) &= \sum_{\alpha} \sum_n \left[f_{\alpha}(n) - \frac{N_1}{N} V_{\alpha}(n) \right]^2 \\ &\quad + \frac{N_0 N_1}{N-1} N_{\alpha} \left(1 - \frac{1}{N_{\alpha}} \sum_n \left(\frac{V_{\alpha}(n)}{N} \right)^2 \right) \end{aligned} \quad (5.46)$$

It is worth mentioning that the first term has a clear meaning, it quantifies the deviation of the projections from situations where all the positions have a probability of N_1/N to be occupied by a black pixel. The second term characterizes the shape of the reconstruction domain.

Here we compute the roughness metric for the three configurations in Figure 5.5. as one could expect, the Poisson point distribution has the largest roughness metric value, single sphere the smallest, and multiple spheres in the middle, as listed in Table 5.2. These results are consistent with the observation that large ground-state degeneracies are generally associated with rough energy landscapes [96, 97].

Table 5.2 Roughness metric for different configurations with same system size and number of target pixels

	Single sphere	Multiple spheres	Poisson distribution
ρ	0.001487	0.003594	0.006465

5.3 Summary

Any stochastic reconstruction algorithm can be considered as an optimization procedure that explore the whole configuration space and try to find one or several configurations that morphologically or functionally match the target configuration. Those configurations that process the same features can be considered as the degeneracy of the target structure. And the number of those configurations strongly affects the performance of the reconstruction algorithm. In the situation with X-ray projections, by exploring the ground-state degeneracy and density of states associated with different number of projections, we have found that increasing the number of projections provides more structural constrains that will reduce the ground-state degeneracy. Eventually, when the number of projections reaches a critical value, the ground-state degeneracy will reduce to one and the target configuration is now uniquely defined by those projections. Using the stochastic reconstruction algorithm with such amount of projections, theoretically, one could get a reconstruction result that perfectly matches the target configuration morphologically.

However, an ergodic exploration of the configuration space and finding out that unique configuration is practically undoable, even for a relative small system. What we really could do is to set up a threshold, which stands as the maximum bias or error that we can live with, and find out one configuration that below the threshold. An energy landscape will then become very important as it provide us an understanding of the degree of similarity of different configurations, in terms of hamming distance, that correspond to each energy level.

In this chapter we have explored the density of states associated with different number of projections for different configurations. It is shown that increasing number of projections can reduce the cumulative density of states for certain energy. And we can end up having a configuration that more similar to the target one after a stochastic reconstruction by using more projections. For different configurations with the same system size and target pixel numbers, the complex configuration will process a higher degree of roughness in the energy landscape. This could explain the low accuracy of reconstructing such structures. More tests should be done in order to fully understand the impact of energy landscape associated with different number of projections. And apply the concept of “information content” from Gommel’s previous work [52] to the current study.

We have demonstrated a promising stochastic reconstruction algorithm with multi-modal data fusion. With that, one possible future work is to follow the procedure in the chapter and systematically study the microstructural degeneracy and energy landscape of the combined information of two-point correlation functions and projection data. And make comparisons with the current results and those with correlation functions [51, 52].

CHAPTER 6

FUTURE WORK

A major advantage of the stochastic procedure is that binary microstructure is readily generated from a handful of projections, with no additional segmentations. With some straightforward generalizations, our method can be easily re-casted to reconstruct microstructural evolution over time from *in situ* tomographic data. For example, we also apply the stochastic procedure to reconstruct the growth process of a fatigue crack. As shown in Figure 6.1A, the target process consists of 6 images showing successive growth stages of the crack. For the image of the initial crack, 20 projections are obtained and used for its reconstruction. For the images of the subsequent cracks, only the contrast between the total attenuations associated with the images of current stage and previous stage are used, so that only the differences between the two microstructures are reconstructed, which requires less computational cost. The reconstructed growth process is shown in Figure 6.1B, which is virtually indistinguishable from the actual process [71].

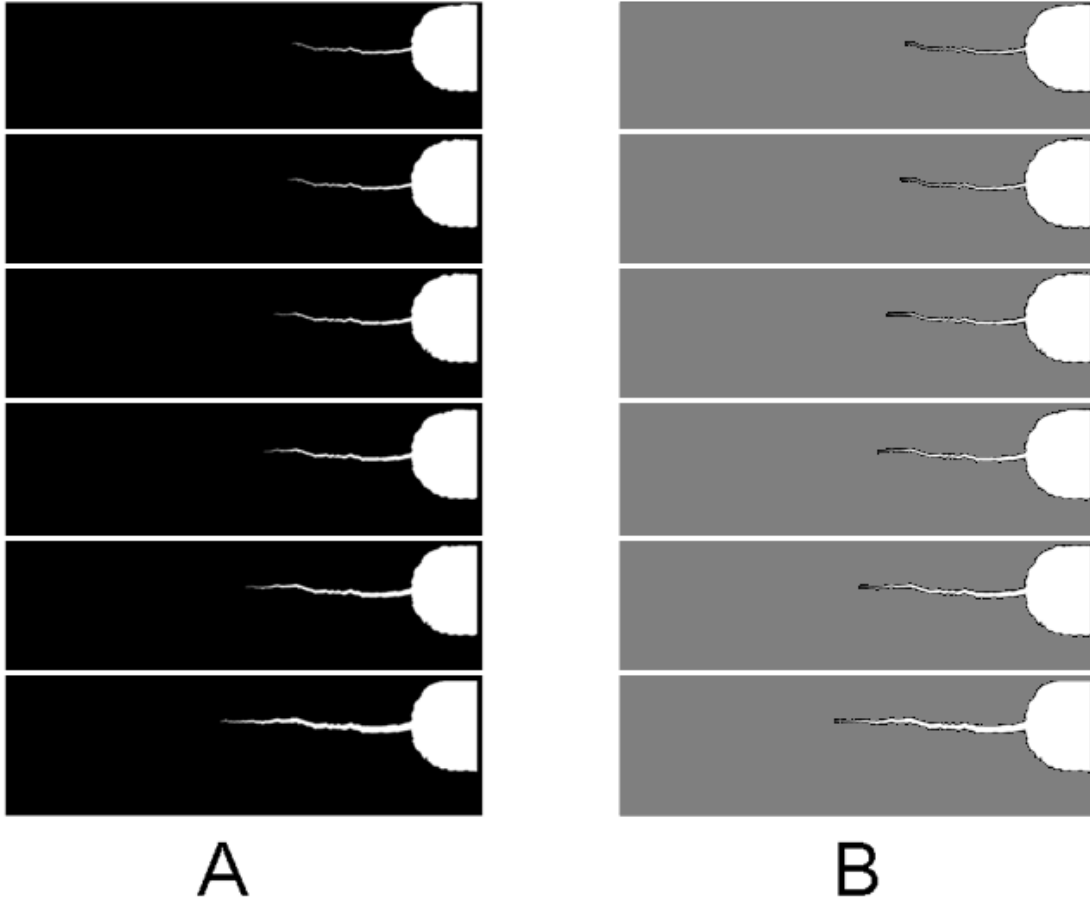


Figure 6.1 Reconstruction of the growth of a fatigue crack. The growth process consists of 6 images showing successive growth stages of the crack. (A) Target process. (B) Reconstructed process.

REFERENCES

- [1] S. Torquato, "Random heterogeneous materials: Microstructure and macroscopic properties," New York: Springer; (2002).
- [2] M. Sahimi, "Heterogeneous materials I: Linear transport and optical properties," New York: Springer; (2003).
- [3] K. Thornton, H.F. Poulsen, "Three-dimensional materials science: An intersection of three-dimensional reconstructions and simulations," *MRS Bull*, (2008) 33, 587-595.
- [4] L. Babout, E. Maire, J.Y. Buffière and R. Fougères, "Characterization by X-ray computed tomography of decohesion, porosity growth and coalescence in model metal matrix composites," *Acta Materialia*, (2001) 49, 2055-2063.
- [5] A. Weck, D.S. Wilkinson, E. Maire and H. Toda, "Visualization by X-ray tomography of void growth and coalescence leading to fracture in model materials," *Acta Materialia*, (2008) 56, 2919-2928.
- [6] H. Toda, S. Yamamoto, M. Kobayashi, K. Uesugi and H. Zhang, "Direct measurement procedure for three-dimensional local crack driving force using synchrotron X-ray microtomography," *Acta Materialia*, (2008) 56, 6027-6039.
- [7] J.J. Williams, Z. Flom, A.A. Amell, N. Chawla, X. Xiao, F. De Carlo, "Damage evolution in SiC particle reinforced Al alloy matrix composites by X-ray synchrotron tomography," *Acta Materialia*, (2010) 58, 6194-6205.
- [8] J.J. Williams, K.E. Yazzie, N.C. Phillips, N. Chawla, X. Xiao, F. De Carlo, N. Iyyer and M. Kittur, "On the correlation between fatigue striation spacing and crack growth rate: a three-dimensional (3-D) X-ray synchrotron tomography study," *Metallurgical and Materials Transactions A*, (2011) 42, 3845-3848.
- [9] Y. Jiao, F.H. Stillinger and S. Torquato, "Modeling heterogeneous materials via two-point correlation functions: Basic principles," *Physical Review E*, (2007) 76, 031110.
- [10] Y. Jiao, F.H. Stillinger and S. Torquato, "Modeling heterogeneous materials via two-point correlation functions: II. Algorithmic details and applications," *Physical Review E*, (2008) 77, 031135.
- [11] Y. Jiao, E. Padilla and N. Chawla, "Modeling and predicting microstructure evolution in lead/tin alloy via correlation functions and stochastic material reconstruction," *Acta Materialia*, (2013) 61, 3370-3377.

- [12] Y. Jiao and N. Chawla, "Three dimensional modeling of complex heterogeneous materials via statistical microstructural descriptors," *Integrating Materials and Manufacturing Innovation*, (2014) 3, 1-19.
- [13] Y. Jiao and N. Chawla, "Modeling and characterizing anisotropic inclusion orientation in heterogeneous material via directional cluster functions and stochastic microstructure reconstruction," *Journal of Applied Physics*, (2014) 115, 093511.
- [14] D. Li, G. Saheli, M. Khaleel and H. Garmestani, "Quantitative prediction of effective conductivity in anisotropic heterogeneous media using two-point correlation functions," *Computational Materials Science*, (2006) 38, 45-50.
- [15] A. Mikdam, A. Makradi, S. Ahzi, H. Garmestani, D. Li and Y. Remond, "Effective conductivity in isotropic heterogeneous media using a strong-contrast statistical continuum theory," *Journal of the Mechanics and Physics of Solids*, (2009) 57, 76-86.
- [16] M. Safdari, M. Baniassadi, H. Garmestani and M.S. Al-Haik, "A modified strong-contrast expansion for estimating the effective thermal conductivity of multiphase heterogeneous materials," *Journal of Applied Physics*, (2012) 112, 114318.
- [17] A. Mikdam, R. Belouettar, D. Fiorelli, H. Hu and A. Makradi, "A tool for design of heterogeneous materials with desired physical properties using statistical continuum theory," *Materials Science and Engineering A*, (2013) 564, 493-500.
- [18] J. Goldstein, D.E. Newbury, P. Echlin, D.C. Joy, A.D. Romig Jr, C.E. Lyman, C. Fiori, and E. Lifshin, "Scanning electron microscopy and X-ray microanalysis: a text for biologists, materials scientists, and geologists," Springer Science & Business Media, (2002).
- [19] D. Dingley and D. Field, "Electron backscatter diffraction and orientation imaging microscopy," *Materials Science and Technology*, (1997) 13(1), 69-78.
- [20] F. Humphreys, "Review grain and subgrain characterisation by electron backscatter diffraction," *Journal of materials science*, (2001), 36(16), 3833-3854.
- [21] A.D. Rollett, S.B. Lee, R. Campman, and G. Rohrer, "Three-dimensional characterization of microstructure by electron back-scatter diffraction," *Annual Review of Materials Research*, (2007), 37, 627-658.
- [22] A.J. Schwartz, M. Kumar, B.L. Adams, and D.P. Field, "Electron backscatter diffraction in materials science," New York: Springer, (2009).
- [23] Baruchel, J., J.-Y. Buffiere, and E. Maire, "X-ray tomography in material science," Paris: Hermes science publications, (2000).

- [24] J. Hsieh, "Computed tomography: principles, design, artifacts, and recent advances," Bellingham, WA: SPIE, (2009).
- [25] D. Brandon and W.D. Kaplan, "Microstructural characterization of materials, 2nd Ed," Wiley; (2008).
- [26] J. Baruchel, P. Bleuet, A. Bravin, P. Coan, E. Lima, A. Madsen, W. Ludwig, P. Pernot and J. Susini, "Advances in synchrotron hard X-ray based imaging," *Comptes rendus-Physique*, (2008) 9, 624-641.
- [27] J.H. Kinney and M.C. Nichols, "X-ray tomographic microscopy (XTM) using synchrotron radiation," *Annual Review of Materials Science*, (1992) 22, 121-152.
- [28] A. Kak and M. Slaney, "Principles of computerized tomographic imaging." IEEE Press; (1988).
- [29] L.A. Feldkamp, L.C. Davis and J.W. Kress, "Practical cone-beam algorithm," *Journal of the Optical Society of America A*, (1984) 1, 612-619.
- [30] A. Kupsch, A. Lange and M.P. Hentschel, „Enhanced spatial resolution in 2D CT-reconstruction without filtered back projection," DIRECTT, WCNDT Shanghai, (2008).
- [31] A. Borbély, F.F. Csikor, S. Zabler, P. Cloetens and H. Biermann, "Three-dimensional characterization of the microstructure of a metal-matrix composite by holotomography," *Material Science & Engineering A*, (2004) 367, 40-50.
- [32] P. Kenesei, H. Biermann and A. Borbély, „Structure-property relationship in particle reinforced metal-matrix composites based on holotomography," *Scripta Materialia*, (2005) 53, 787-791.
- [33] G.T. Herman and A. Kuba, "Discrete tomography: Foundations, algorithms, and applications," Boston: Birkhäuser, (1999).
- [34] G.T. Herman and A. Kuba, "Advances in discrete tomography and its applications," Boston: Birkhäuser, (2007).
- [35] R.J. Gardner, P. Gritzmann, "Discrete tomography: determination of finite sets by X-rays," *Transactions of the American Mathematical society*, (1997) 349, 2271-2295.
- [36] L. Hajdu, R. Tijdeman, "Algebraic aspects of discrete tomography," *Journal für die reine und angewandte Mathematik*, (2001) 534, 119-128.
- [37] S. Brunetti, A. Del Lungo, P. Gritzmann, S. de Vries, "On the reconstruction of binary and permutation matrices under (binary) tomographic constraints," *Theoretical Computer Science*, (2008) 406, 63-71.

- [38] P. Gritzmann, B. Langfeld, “On the index of Siegel grids and its application to the tomography of quasicrystals,” *European Journal of Combinatorics*, (2008) 29, 1894-1909.
- [39] H.J. Ryser, “Matrices of zeros and ones,” *Bulletin of the AMS - American Mathematical Society*, (1960) 66, 442-464.
- [40] E. Barcucci, S. Brunetti, A. Del Lungo, M. Nivat, “Reconstruction of lattice sets from their horizontal, vertical and diagonal X-rays,” *Discrete Mathematics*, (2001) 241, 65-78.
- [41] J. Batenburg and J. Sijbers, “DART: A practical reconstruction algorithm for discrete tomography,” *In: IEEE transactions on image processing*, (2011) 20, 2542-2553.
- [42] W. van Aarle, K. J. Batenburg, and J. Sijbers, “Automatic parameter estimation for the discrete algebraic reconstruction technique (DART),” *IEEE Transactions on Image Processing*, (2012).
- [43] K. J. Batenburg and J. Sijbers, “Generic iterative subset algorithms for discrete tomography,” *Discrete Applied Mathematics*, (2009) 157, 438-451.
- [44] A. Alpers, H.F. Poulsen, E. Knudsen, G.T. Herman, “A discrete tomography algorithm for improving the quality of 3D XRD grain maps,” *Journal of Applied Crystallography*, (2006) 39, 582-588.
- [45] L. Rodek, H.F. Poulsen, E. Knudsen, G.T. Herman, “A stochastic algorithm for reconstruction of grain maps of moderately deformed specimens based on X-ray diffraction,” *Journal of Applied Crystallography*, (2007) 40, 313-321.
- [46] X. Huang, Y. Lai, Z.H. Hang, H. Zheng and C.T. Chan, “Dirac cones induced by accidental degeneracy in photonic crystals and zero-refractive-index materials,” *Nature materials*, (2011) 10(8), 582-586.
- [47] Y. Pei, X. Shi, A. LaLonde, H. Wang, L. Chen, and G.J. Snyder, “Convergence of electronic bands for high performance bulk thermoelectrics,” *Nature*, (2011) 473(7345), 66-69.
- [48] K.M. Wu, and M. Enomoto, “Three-dimensional morphology of degenerate ferrite in an Fe–C–Mo alloy,” *Scripta materialia*, (2002) 46(8), 569-574.
- [49] Y. Jiao, F.H. Stillinger, and S. Torquato, “Geometrical ambiguity of pair statistics: Point configurations,” *Physical Review E*, (2010) 81(1), 011105.
- [50] Y. Jiao, F.H. Stillinger, and S. Torquato, 2010. “Geometrical ambiguity of pair statistics. II. Heterogeneous media,” *Physical Review E*, (2010) 82(1), 011106.

- [51] C.J. Gommès, Y. Jiao, and S. Torquato, “Density of states for a specified correlation function and the energy landscape,” *Physical Review Letters*, (2012) 108(8), 080601.
- [52] C.J. Gommès, Y. Jiao, and S. Torquato, “Microstructural degeneracy associated with a two-point correlation function and its information content,” *Physical Review E*, (2012) 85(5), 051140.
- [53] H. Li, S. Singh, N. Chawla, and Y. Jiao, “Direct extraction of spatial correlation functions from limited X-ray tomography data for microstructure quantification,” *in preparation* (2016).
- [54] S. Torquato, “Exact expression for the effective elastic tensor of disordered composites,” *Physical Review Letters*, (1997) 79, 681.
- [55] S. Torquato, “Effective stiffness tensor of composite media—I. Exact series expansions,” *Journal of the Mechanics and Physics of Solids*, (1997) 45, 1421-1448.
- [56] D. Hlushkou, H. Liasneuski, U. Tallarek and S. Torquato, “Effective diffusion coefficients in random packings of polydisperse hard spheres from two-point and three-point correlation functions,” *Journal of Applied Physics* (2015) 118, 124901.
- [57] S. Torquato, “Effective electrical conductivity of two-phase disordered composite media,” *Journal of Applied Physics*, (1985) 58, 3790-3797.
- [58] H. Li, S. Singh, C.S. Kaira, J.C.E. Mertens, J.J. Williams, N. Chawla and Y. Jiao, 2016. “Microstructural quantification and property prediction using limited X-ray tomography data,” *JOM*, (2016) 68(8), 2288-2295.
- [59] S. Singh, H. Li, Y. Jiao and N. Chawla, “Direct prediction of mechanical properties of polymer-matrix composites from limited x-ray tomography data,” *in preparation*, (2016).
- [60] Z. Hashin and S. Shtrikman, “A variational approach to the theory of the elastic behavior of multiphase materials,” *Journal of the Mechanics and Physics of Solids*, (1962) 11, 127-140.
- [61] J.N. Hall, J.W. Jones, and A.K. Sachdev, “Particle size, volume fraction and matrix strength effects on fatigue behavior and particle fracture in 2124 Aluminum-SiC composites,” *Materials Science and Engineering: A*, (1994) 183(1-2), 69-80.
- [62] N. Chawla, J.W. Jones, C. Andres and J.E. Allison, “Effect of SiC volume fraction and particle size on the fatigue resistance of a 2080 Al/SiC composite,” *Metallurgical and Materials Transactions A*, (1998) 29(11), 2843-2854.

- [63] N. Chawla, U. Habel, Y.L. Shen, C. Andres, J.W. Jones and J.E. Allison, “The effect of matrix microstructure on the tensile and fatigue behavior of SiC particle-reinforced 2080 Al matrix composites,” *Metallurgical and Materials Transactions A*, (2000) 31(2), 531-540.
- [64] N. Chawla, C. Andes, L.C. Davis, J.E. Allison and J.W. Jones, 2000. “The interactive role of inclusions and SiC reinforcement on the high-cycle fatigue resistance of particle reinforced metal matrix composites,” *Metallurgical and Materials Transactions A*, (2000) 31(3), 951-957.
- [65] C.L.Y. Yeong and S. Torquato, “Reconstructing random media,” *Physical Review E*, (1998) 57, 495-506.
- [66] S. Kirkpatrick, C.D. Gelatt and M.P. Vecchi, “Optimization by simulated annealing,” *Science*, (1983) 220, 671-680.
- [67] N. Robert, F. Peyrin and M.J. Yaffe, “Binary vascular reconstruction from a limited number of cone beam projections,” *Medical Physics*, (1994) 21, 1839.
- [68] C.V. Alvino and A.J. Yezzi, Jr., “Tomographic reconstruction of piecewise-smooth images,” *Proceedings of the 2004 IEEE Computer Conference*, (CVPR’04).
- [69] A. Donev, I. Cisse, D. Sachs, E.A. Variano, F.H. Stillinger, R. Connelly, S. Torquato and P.M. Chaikin, “Improving the density of jammed disordered packings using ellipsoids,” *Science*, (2004) 303, 990-993.
- [70] H. Li, N. Chawla and Y. Jiao, “Reconstruction of heterogeneous materials via stochastic optimization of limited-angle X-ray tomographic projections,” *Scripta Materialia*, (2014) 86, 48-51.
- [71] H. Li, C.S. Kaira, J.C.E. Mertens, J.J. Williams, N. Chawla and Y. Jiao, “Accurate Stochastic Reconstruction of Heterogeneous Material Microstructure from Limited X-ray Tomographic Projections: Algorithmic Details and Applications,” *Journal of Microscopy*, (2016) 264(3), 339-350.
- [72] J.C.E. Mertens and N. Chawla, “Modeling and characterization of X-ray yield in a polychromatic, lab-scale, X-ray computed tomography system,” *Nuclear Instruments and Methods in Physics Research A*. (2015) 783, 110-116.
- [73] F. de Andrade Silva, J.J. Williams, B.R. Müller, M.P. Hentschel, P.D. Portella, and N. Chawla, 2010. “Three-dimensional microstructure visualization of porosity and Fe-rich inclusions in SiC particle-reinforced Al alloy matrix composites by X-ray synchrotron tomography,” *Metallurgical and Materials Transactions A*, (2010) 41(8), 2121-2128.
- [74] A.P. Roberts, “Statistical reconstruction of three-dimensional porous media from two-dimensional images,” *Physical Review E*, (1997) 56(3), 3203.

- [75] D.T. Fullwood, S.R. Kalidindi, S.R. Niezgoda, A. Fast, and N. Hampson, “Gradient-based microstructure reconstructions from distributions using fast Fourier transforms,” *Materials Science and Engineering: A*, (2008) 494(1), 68-72.
- [76] D.T. Fullwood, S.R. Niezgoda and S.R. Kalidindi, 2008. “Microstructure reconstructions from 2-point statistics using phase-recovery algorithms,” *Acta Materialia*, (2008) 56(5), 942-948.
- [77] A. Hajizadeh, A. Safekordi and F.A. Farhadpour, “A multiple-point statistics algorithm for 3D pore space reconstruction from 2D images,” *Advances in Water Resources*, (2011) 34(10), 1256-1267.
- [78] P. Tahmasebi and M. Sahimi, “Reconstruction of three-dimensional porous media using a single thin section,” *Physical Review E*, (2012) 85(6), 066709.
- [79] P. Tahmasebi and M. Sahimi, “Cross-correlation function for accurate reconstruction of heterogeneous media,” *Physical Review Letters*, (2013) 110(7), 078002.
- [80] P. Tahmasebi and M. Sahimi, “Geostatistical simulation and reconstruction of porous media by a cross-correlation function and integration of hard and soft data,” *Transport in Porous Media*, (2015) 107(3), 871-905.
- [81] D. Chen, Q. Teng, X. He, Z. Xu and Z. Li, “Stable-phase method for hierarchical annealing in the reconstruction of porous media images,” *Physical Review E*, (2014) 89(1), 013305.
- [82] Y. Jiao, “Three-Dimensional Heterogeneous Material Microstructure Reconstruction from Limited Morphological Information via Stochastic Optimization,” *AIMS Materials Science*, (2014) 1, 28-40.
- [83] K.M. Gerke, M.V. Karsanina, R.V. Vasilyev and D. Mallants, “Improving pattern reconstruction using directional correlation functions,” *EPL (Europhysics Letters)*, (2014) 106(6), 66002.
- [84] K.M. Gerke, M.V. Karsanina, “Improving stochastic reconstructions by weighting correlation functions in an objective function,” *EPL (Europhysics Letters)*, (2015) 111(5), 56002.
- [85] M.V. Karsanina, K.M. Gerke, E.B. Skvortsova and D. Mallants, 2015. “Universal spatial correlation functions for describing and reconstructing soil microstructure,” *PloS one*, (2015) 10(5), e0126515.
- [86] S. Chen, A. Kirubanandham, N. Chawla and Y. Jiao, “Stochastic multi-scale reconstruction of 3D microstructure consisting of polycrystalline grains and second-phase particles from 2D micrographs,” *Metallurgical and Materials Transactions A*, (2016) 47(3), 1440-1450.

- [87] D.M. Turner and S.R. Kalidindi, "Statistical construction of 3-D microstructures from 2-D exemplars collected on oblique sections," *Acta Materialia*, (2016) 102, 136-148.
- [88] H. Xu, M.S. Greene, H. Deng, D. Dikin, C. Brinson, W.K. Liu, C. Burkhart, G. Papakonstantopoulos, M. Poldneff and W. Chen, "Stochastic reassembly strategy for managing information complexity in heterogeneous materials analysis and design," *Journal of Mechanical Design*, (2013) 135(10), 101010.
- [89] X. Liu and V. Shapiro, "Random heterogeneous materials via textures synthesis," *Computational Materials Science*, (2015) 99, 177-189.
- [90] V. Sundararaghavan and N. Zabarav, "Classification and reconstruction of three-dimensional microstructures using support vector machines," *Computational Materials Science*, (2005) 32(2), 223-239.
- [91] R. Bostanabad, A.T. Bui, W. Xie, D.W. Apley and W. Chen, "Stochastic microstructure characterization and reconstruction via supervised learning," *Acta Materialia*, (2016) 103, 89-102.
- [92] R. Bostanabad, W. Chen and D.W. Apley, "Characterization and reconstruction of 3D stochastic microstructures via supervised learning," *Journal of Microscopy*, (2016).
- [93] Private conversation with C.J. Gommers, (2016).
- [94] F. Wang, and D.P. Landau, "Efficient, multiple-range random walk algorithm to calculate the density of states," *Physical Review Letters*, (2001) 86(10), 2050.
- [95] F. Wang, and D.P. Landau, "Determining the density of states for classical statistical models: A random walk algorithm to produce a flat histogram," *Physical Review E*, (2001) 64(5), 056101.
- [96] D.J. Wales, M.A. Miller and T.R. Walsh, 1998. "Archetypal energy landscapes," *Nature*, 394(6695), 758-760.
- [97] P.G. Debenedetti and F.H. Stillinger, "Supercooled liquids and the glass transition," *Nature*, (2001) 410(6825), 259-267.
- [98] R.W. Hamming, "Error detecting and error correcting codes," *Bell System technical journal*, (1950) 29(2), 147-160.